



**Politecnico di Torino**

---

DIPARTIMENTO DI INGEGNERIA MECCANICA E AEROSPAZIALE  
Corso di Laurea Magistrale in Ingegneria Aerospaziale

TESI DI LAUREA MAGISTRALE

**Analysis of the turbulent anisotropic flow inside an industrial  
large autoclave and the relevant problem of homogenization  
lack**

Candidato:  
**Luca Cattarossi**  
Matricola 277928

Relatore:  
**Prof.ssa Daniela Tordella**  
Correlatori:  
**Prof. Daniele Marchisio**  
**Dott. Luca Banetta**

Alla mia famiglia ...

### **Abstract**

The following thesis work aims to investigate the behavior of a turbulent flow that develops inside an autoclave. The state of the art design of these industrial machineries is the reason for the production of a highly anisotropic turbulent flow that negatively affects the temperature distribution inside the chamber and threatens the success of the various heat treatment processes for which these machines are predisposed. A viscous and incompressible wall flow with a high Reynolds number has been studied, and then control techniques have been used to homogenize this flow. These consisted of a number of randomly activated velocity perturbations placed on the walls of the vacuum chamber. The impact of these sources was examined through LES simulations conducted on a grid of approximately  $8 \cdot 10^6$  cells of size a few tens of millimeters. The whole was simulated using the open-source code PLUTO V4.4.2.



# Table of Contents

<b>1</b>	<b>Introduction</b>	<b>1</b>
1.1	Polymer matrix composites . . . . .	1
1.2	Curing treatment . . . . .	3
1.3	State of art: Autoclave . . . . .	6
1.3.1	Historical background . . . . .	7
1.3.2	Autoclave cycle . . . . .	7
1.4	Fluid dynamics setup . . . . .	8
1.4.1	Numerical studies of computational fluid dynamics (CFD) . . . . .	10
1.4.2	RANS approach and unresolved issues . . . . .	10
1.5	Thesis outline . . . . .	11
<b>2</b>	<b>Physical-mathematical model</b>	<b>13</b>
2.1	Navier-Stokes Equations . . . . .	13
2.1.1	Reynolds number . . . . .	15
2.2	Concept of Turbulence . . . . .	16
2.2.1	Energy cascade . . . . .	18
2.3	Statistical description of turbulent flow . . . . .	19
2.3.1	Reynolds equations for turbulent flows . . . . .	19
2.3.2	Homogeneous isotropic turbulence . . . . .	20
2.4	Spectral analysis . . . . .	21
2.5	Turbulence models and numerical simulations . . . . .	21
2.5.1	DNS: Direct numerical simulation . . . . .	22
2.5.2	RANS: Reynolds-averaged Navier-Stokes . . . . .	22
2.5.3	LES: Large-eddy simulation . . . . .	26
<b>3</b>	<b>Physical problem</b>	<b>31</b>
3.1	Simulations set-up . . . . .	31
3.1.1	Notes on simulations with Openfoam . . . . .	34
3.1.2	Operating conditions and Viscosity modelling . . . . .	34
3.2	Implementation of additional perturbations ('hatches') . . . . .	37
3.2.1	C script . . . . .	38

<b>4</b>	<b>Numerical methods</b>	<b>43</b>
4.1	Initial description of software: PLUTO code v4.4.2 . . . . .	43
4.2	The Hydrodynamics (HD) Module . . . . .	44
4.3	Finite Volume Method . . . . .	45
4.4	Reconsrtuction: WENOZ Schemes . . . . .	46
4.5	Time stepping: Runge-Kutta (RK3) . . . . .	48
4.5.1	Time Step Determination . . . . .	48
4.6	Numerical Integration of Diffusion Terms . . . . .	49
4.7	Riemann solver: Roe . . . . .	49
<b>5</b>	<b>Numerical simulations and results</b>	<b>51</b>
5.1	Scaling and simulation time . . . . .	52
5.2	Development of the simulation process . . . . .	53
5.2.1	ParaView . . . . .	54
5.2.2	Spectral analysis . . . . .	54
5.2.3	Visualization of results . . . . .	55
<b>6</b>	<b>Conclusions</b>	<b>83</b>
6.1	Future Scenarios . . . . .	83

# List of Tables

2.1	Filter functions for one-dimensional filters [6] . . . . .	28
4.1	Solution to the next time level: where $\Delta t^n = t^{n+1} - t^n$ is the time increment between two consecutive steps and $\mathcal{L}$ denotes the discretized spatial operator on the right hand side of Eq.(4.1) [10]. . . . .	48
4.2	CFL condition [10]. . . . .	49
5.1	Technical specifications of the cluster used for the development of the thesis project. This is one of the three clusters of the HPC of the Politecnico di Torino; the <i>global</i> partition was used [40]. . . . .	51
5.2	This is the result of the scaling performed for the simulations with two million cells. Indeed, the table shows us that the elapsed time trend is roughly linear as the number of processors used increases. . . . .	53



# List of Figures

1.1	Structure of a fibre-reinforced composite material[37] . . . . .	2
1.2	Effect of resin flow[25] . . . . .	5
1.3	Example of an industrial autoclave. There are many types and sizes depending on what types of processing they need to accommodate inside.	6
1.4	Autoclave air flow [30]. The image describes what is usually the path that is taken by the flow before it is fed into the chamber. The latter diffuses, reaches the bottom of the machinery and is collected and recirculated. . .	8
2.1	Streamlines of a turbulent flow inside an autoclave. The image was produced with ParaView [11] from one of many simulations performed. . . .	16
2.2	Energy cascade [6] . . . . .	18
2.3	Sample paths of $\mathbf{U}(t)$ [6] . . . . .	19
2.4	Example of filtered velocity field component, using Gaussian filter [6]. The lines in bold are those corresponding to $\overline{\mathbf{U}}(\mathbf{x})$ and $\overline{\mathbf{u}^2}(\mathbf{x})$ . . . . .	27
3.1	Injection ring. It's an annular inlet for the air flow, as is often the case in real autoclaves. The flow enters the chamber in the positive x-axis direction and develops. . . . .	32
3.2	The figure shows us what is a zoom on the geometric construction of the injection ring of the presented autoclave model. The thickness, as can be clearly seen, is that of a single mesh cell. . . . .	32
3.3	(3.3a and 3.3b) Contour of the x-component of velocity. (3.3c) Cross-sectional plane of the autoclave at $y=0$ . Arrows have been manually added to the images to indicate what is the path that the flow is forced to follow before it can develop freely in the chamber. . . . .	33
3.4	The one presented in this image is the geometry of the autoclave made using the techniques available in Openfoam that allow the undesired shape to be cut out directly from the source domain. . . . .	35
3.5	The figure shows the successful dummy cut operation of the geometry in PLUTO. Despite the difficulties encountered, it can be seen that the result is very similar to that obtained in Openfoam (3.4). . . . .	35
3.6	Difference between geometric box and autoclave. From the initial parallelepiped, the representative step shape of the autoclave was derived. . . .	36

3.7	Hatches - start configuration. In one of the two head configurations, the hatches are placed at the top and bottom, corresponding to the axis of the autoclave. . . . .	38
3.8	Hatches arrangement. Such a solution is the one that will prove most promising and involves totally random placement of the hatches around the side surface of the autoclave. . . . .	41
3.9	The image depicts the structure of the hatches in detail. It can be understood, from this figure, how their geometry is such that they fit perfectly with the course of the autoclave surface. . . . .	42
4.1	Two-dimensional Cartesian grid for finite volumes . . . . .	46
5.1	The figures 5.1a and 5.1b represent the motion field of the x component of the velocity vector after 2.0 physical seconds of simulation. By zooming in, we can see that there is a powerful backflow that continues along the wall to the bottom of the autoclave. This is clearly a numerical error that has no physical meaning whatsoever and will therefore have to be corrected.	56
5.2	These two figures are the representation of the motion field <sup>1</sup> of the x-component of the velocity vector. In figure 5.2a, the numerical method of spatial reconstruction WENO3 was used, in contrast to figure 5.2b where the method applied is WENOZ. It is noticeable how, thanks to WENOZ, the problem of the large recirculation of the near-wall flow is somewhat alleviated without having intervened on the <i>fluid_interface_boundary.c</i> . . . . .	58
5.3	These image pairs were realised using finite difference discretization. Here, too, the backflow phenomenon appears; moreover, it must be considered that the finite difference method is much more time-consuming in terms of simulation time than the finite volume method. Between the figure 5.3a and the figure 5.3b, the WENOZ method gives us a better structured motion field with more scales of motion. . . . .	59
5.4	This is the visualisation of the velocity motion field captured with a grid of 2 million cells. There are a few swirling zones beginning to form here and there within the autoclave, giving the impression of a turbulent motion field. The snapshot shown above is that of a physical simulation time of 8.0 seconds, which is quite representative of an already highly developed field of motion. . . . .	60
5.5	This is the visualisation of the velocity motion field captured with a grid of 8 million cells and after about 8.0 seconds of simulation. These times are sufficient for the airflow to reach the bottom of the autoclave and for the turbulence to fully develop. The system of vortex structures in this case is even more evident. . . . .	61

---

<sup>1</sup>The colour bar has not been reported again, but the range of values also in this space is between -7.1 and 5.0.

5.6 Shown are 3 snapshots of the Tracer diffusion inside the autoclave. The succession of the figures, at three different instants (from figure 5.6a to figure 5.6c we go from 1.0 seconds, 2.5 seconds up to 4.4 seconds of simulation), allows us to observe how it is slowly diffused throughout the volume, as a direct action of the turbulence present. The value of the passive scalar is in a range between 0.0 and 1.0. . . . . 62

5.7 The figure 5.7a represents the velocity component parallel to the longitudinal axis of the autoclave and is the result of a direct approach (DNS) for solving the equations of motion. In the image 5.7b, on the other hand, the LES filter has been applied and thus a new criterion for solving the smallest scales of motion. In both cases, the simulation time is approximately 4.5 seconds. . . . . 64

5.8 The motion snapshot shows how the air flow, after 7.5 seconds, has already reached the end of the autoclave. The simulation was performed with the LES filter present. The 5.8b and 5.8c represent the zoom of two vortical structures captured and resolved by the computational calculation clearly and distinctly. . . . . 65

5.9 Shown here are three images depicting the motion field of kinetic energy on the longitudinal axis of the autoclave. It is a very important parameter in understanding the homogenization of turbulence. The figure 5.9a represents the condition with no hatches; the figure 5.9b depicts the condition where the hatches are placed high and low; finally, the third and last image (5.9c) represents the condition where the apertures are placed randomly. . . . . 67

5.10 Here, the motion field of kinetic energy is depicted in a plane transverse to the autoclave axis at a station  $x = 2.55$  m. The first figure at the top, (5.10a), represents the condition without hatches; in the line below from left to right we find the figure (5.10b) depicting the condition in which the hatches are placed at the top and bottom, and the (5.10c) representing the condition in which the hatches are placed randomly. . . . . 68

5.11 These are 3D contours of the kinetic energy of the  $xz$  plane exactly on the axis of the autoclave ( $y = 0$ ) after 7.5 seconds of simulation. The figure 5.11a represents the base case, while the 5.11b represents the autoclave with hatches. . . . . 69

5.12 The figures represent once again the contours of the kinetic energy on the  $yz$  plane at different positions along the longitudinal axis of the autoclave, at the same time (7.5 seconds). The left column belongs to the case without implemented hatches, while the right column belongs to the case with the hatches in random positions. The three stations considered, from top to bottom, moving towards the bottom of the chamber are:  $x = 5.1$ m (5.12a and 5.12b);  $x = 2.55$ m (5.12c and 5.12d);  $x = 1.275$ m (5.12e and 5.12f). . . . . 70

5.13 In these two figures we can clearly see the concept of improved and accelerated homogenization that is dictated by the presence of the hatches. In the figure 5.13a without the hatches it is noted that the passive scalar introduced in the system has not yet been well distributed throughout the volume, unlike the figure 5.13b where instead the implementations of localized perturbations of better speeds and you accelerate just such distribution process. Both are snapshots taken after 7.5 physical seconds of simulation. . . . . 72

5.14 These figures represent the spectra of Kinetic Energy in the wave number range. The comparison made is between simulations with the autoclave configuration with random hatches (left column) and those with the autoclave without these additional tools (right column). In this case the  $y=0$  plane, parallel to the autoclave axis, is analyzed; then in this which is more generally the  $x-z$  plane 10000 points along the  $x$  direction are sampled at three different stations of the  $z$  coordinate:  $z=0$ ,  $z=0.306$  and  $z=0.612$ . . . . . 73

5.15 These figures represent the spectra of Kinetic Energy in the wave number range. The comparison made is between simulations with the autoclave configuration with random hatches (left column) and those with the autoclave without these additional tools (right column). In this case the  $y=0.306$  plane, parallel to the autoclave axis, is analyzed; then in this which is more generally the  $x-z$  plane 10000 points along the  $x$  direction are sampled at three different stations of the  $z$  coordinate:  $z=0$ ,  $z=0.306$  and  $z=0.612$ . . . . . 74

5.16 These figures represent the spectra of Kinetic Energy in the wave number range. The comparison made is between simulations with the autoclave configuration with random hatches (left column) and those with the autoclave without these additional tools (right column). In this case the  $y=0.612$  plane, parallel to the autoclave axis, is analyzed; then in this which is more generally the  $x-z$  plane 10000 points along the  $x$  direction are sampled at three different stations of the  $z$  coordinate:  $z=0$ ,  $z=0.306$  (in this case the  $z=0.612$  coordinate was characterized by null values and for this reason it was left out). . . . . 75

5.17 These figures represent the spectra of Kinetic Energy in the wave number range. The comparison made is between simulations with the autoclave configuration with random hatches (left column) and those with the autoclave without these additional tools (right column). In this case 10000 points are sampled along the  $y$ -direction, in  $y-z$  planes transverse to the autoclave. The plane corresponding to these graphs is  $x=1.275$  and on it three different stations of the  $z$ -coordinate are selected:  $z=0$ ,  $z=0.306$ ,  $z=0.612$ . . . . . 76

5.18 These figures represent the spectra of Kinetic Energy in the wave number range. The comparison made is between simulations with the autoclave configuration with random hatches (left column) and those with the autoclave without these additional tools (right column). In this case 10000 points are sampled along the y-direction, in y-z planes transverse to the autoclave. The plane corresponding to these graphs is  $x=2.55$  and on it three different stations of the z-coordinate are selected:  $z=0$ ,  $z=0.306$ ,  $z=0.612$ . . . . . 77

5.19 These figures represent the spectra of Kinetic Energy in the wave number range. The comparison made is between simulations with the autoclave configuration with random hatches (left column) and those with the autoclave without these additional tools (right column). In this case 10000 points are sampled along the y-direction, in y-z planes transverse to the autoclave. The plane corresponding to these graphs is  $x=5.1$  and on it three different stations of the z-coordinate are selected:  $z=0$ ,  $z=0.306$ ,  $z=0.612$ . . . . . 78

5.20 What is depicted in these two figures is a 3D contour of the Q-criterion with a value of 100. Then on the display, the isosurfaces are coloured with vorticity values in a range from 0.0 to 150.0. The figure 5.20a depicts the autoclave without hatches, while the figure 5.20b depicts the autoclave characterised by the presence of hatches. . . . . 80

5.21 What is depicted in these two figures is a 3D contour of the Q-criterion with a value of 1000. Then on the display, the isosurfaces are coloured with vorticity values in a range from 0.0 to 150.0. The figure 5.21a depicts the autoclave without hatches, while the figure 5.21b depicts the autoclave characterised by the presence of hatches. . . . . 81



# Chapter 1

## Introduction

Nowadays, the improvement of the quality of the components, especially those that have structural functions, is becoming more and more widespread. This showed a clear surge in growth in the composites industry, compared to all other sectors, despite the general slowdown in the European and world economies. Crucial, more than anything else, is the type of processing to which these types of materials are subjected. However, the one that is making inroads more than others, especially in the aerospace field, but not only, is the autoclave curing process.

### 1.1 Polymer matrix composites

What makes polymer matrix composites special is precisely their composition: they are formed from a combination of materials that can exceed the performance that would be achieved by simply adding up their individual components, one by one [26].

Especially in the transport industry, the specific mechanical properties (i.e. divided by density) of composites make them extremely superior to generic metal alloys, such as aluminium and steel [26], which are still used, for instance, in structural applications anyways. In particular, other mechanical features of interest are strength and stiffness, together with fatigue and corrosion resistance [30]. These materials also require less machining and fastening; this detail, together with all the other aspects, undoubtedly contributes to their increasing popularity day by day. Despite the high cost required for their production, they are increasingly used in the aerospace, shipbuilding, automotive and wind energy sectors, in many civil as well [25]. However, the economic issue remains one of the most delicate aspects, which is why it is essential to try to make production processes more [17], for example by acting on the timing of production cycles. There are different types of composite materials, depending on the fibre reinforcement (glass, carbon, aramid, etc.) and the polymer matrix [26]. Here, we will mainly focus on Carbon Fiber Reinforced Polymers (CFRP). The mechanical properties, mentioned above, are the aspect that distinguishes this type of material and therefore the one that needs to be paid the most attention to during the curing process; they mostly depend on the degree of polymerization and the residual stresses developed during the process

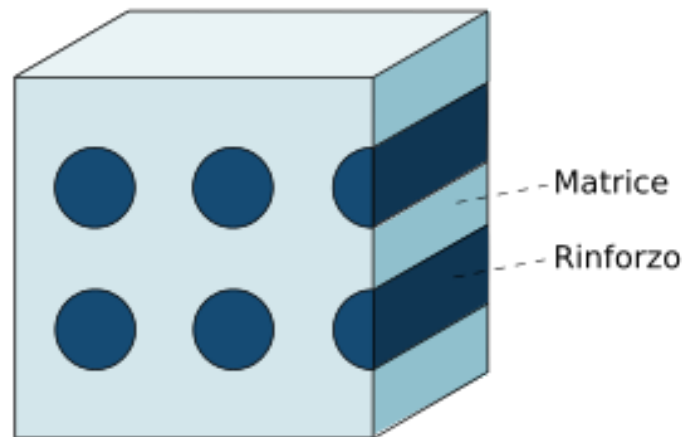


Figure 1.1: Structure of a fibre-reinforced composite material[37]

[29](both these aspects will be discussed in more detail in the next section 1.2). The quality of composite production is the discriminating factor in determining the success of an industrial process of this type. In aerospace applications, composite parts such as aileron ribs and fuselage spars, for example, perform very important structural functions in the economy of the proper functioning of the aircraft [25], and it is therefore essential that they reflect a certain degree of reliability. In order to achieve certain standards, the production of polymeric composites need to be well thought. It involves the laying of the pre-impregnated material by automated layering with adhesive tape [30]. The final result of this procedure is unidirectional tapes or fibres impregnated by a reactive epoxy resin; in the industry, they are usually referred to as "prepregs" [26]. They are laid one on top of the other, arranging the fibres as required by that specific production programme; then, depending on the type of fabrication used, the laminates, whose thickness usually goes from 1 to 10 millimetres, are placed on open or closed moulds that are called 'tools' [26]. These tools can also be made of metal or composite material with thicknesses of up to tens of centimetres [26]. The first priority of the tools is to be rigid and stable during the polymerization cycle, as they have to give the final shape to the composite laminates barring any residual stresses that may be present. At the end of the process, they will be separated from the laminates, which will then be subjected to machining processes, non-destructive testing and assembly operations [26]. In addition to uncured prepreg, typical laminated composite structures also include materials such as honeycomb core, pre-cured composite stiffeners and structural adhesives to join the various parts [3]. The industrial process that follows this layering of the fibres is the polymerization of the laminates.

## 1.2 Curing treatment

As already mentioned, today's composite components require perfect quality with reasonable production times and costs. The production time and, above all, the economic aspect are, however, considerably compromised by the use of the polymerisation process [23], which is generally a highly expensive and energy-intensive process. It is precisely for this reason that research in this field has ample room for growth. Polymerisation is achieved by placing the tools in a pressurised oven, called an autoclave, each with a composite laminate on it. In order to achieve high quality, it is important to prevent the temperature inside the parts from rising too much during polymerisation, as this can reduce the mechanical properties of the moulded part [20]. However, this can also occur if the temperature of the gas surrounding the part is below the critical temperature due to an exothermic reaction caused by the polymerisation itself [20]. It acts directly on the matrix of the composite laminate, which consists of a thermosetting resin, which is in fact polymerised through the application of heat [29]. The process in question involves an initial compaction phase, necessary to ensure that the maximum fibre volume fraction is achieved [31], and a thermal polymerisation phase proper. As can be deduced, the chemistry of this process is very important: the curing process involves a series of chemical reactions that lead to the conversion of low molecular weight monomers into a highly cross-linked macromolecular structure [3]. As explained in detail by Andrew A. Johnston [3], the kinetics of bond formation is the phase that controls the speed of the polymerization process; it is believed that the slowing of the bond formation rate during vitrification is a result of the reduction in the free volume of the resin and the molecular mobility that accompanies this transition. This increasingly restricted molecular mobility leads to a limiting degree of polymerization being reached immediately after vitrification. The extent of the chemical reaction of the resin is generally indicated by a measure known as the degree of polymerisation,  $\alpha$  which is usually defined by the measure of heat released by the bond formation, as follows [3]:

$$\alpha = \frac{1}{H_R} \int_0^t \left( \frac{dq}{dt} dt \right) \quad (1.1)$$

where  $\frac{dq}{dt} dt$  is the rate of heat generation and  $H_R$  is the total amount of heat evolved during a 'complete' reaction. One of the most popular techniques as part of the analysis of the chemical kinetics of resin is differential scanning calorimetry (DSC), used to obtain the kinetic parameters of exothermic reactions [29]. There are two major families of composite material production: wet layup and dry layup processes. Wet layup processes [31] are those in which resin and fabric have been mixed beforehand. The chemical polymerization reaction is 'frozen' by the low supply temperature (-20°C) until it is activated by the heat itself. When the resin is heated, its viscosity decreases and it can flow through the thickness of the part, which is why these 'parts' are supplied with an excess of resin in them. Due to this movement of resin through the thickness, the layers forming the laminate will be joined together. In contrast, dry processes [31] are characterised by the usual impregnation phase, which this time, however, takes

place directly inside the moulds. They have considerable advantages over wet processes because they allow production with the same quality but at a much lower cost; however, they also require a much more accurate knowledge of material behaviour and production techniques. Generally speaking, the objective of any composite manufacturing process is to impregnate the fabric with resin in the most efficient way and to evacuate all the pores or voids [31] which, as has already been said, reduce the mechanical properties of the parts by irreversibly compromising the functions they have to perform. What generally happens to thermosetting composites during a generic curing process is that they go through three different phases [32] as temperature and pressure changes occur: the three phases are solid, liquid and rubbery. The composite passes from the liquid to the rubber stage at the first temperature increase, which is responsible for the formation of a thermal gradient, which in turn will cause uneven resin flow and the formation of voids. There are two main heat sources for the composite in the curing process. One is heat transfer by convection of heated air and the other is heat conduction between the mould and the composite [32]. The interesting part of the curing process, is to study the behaviour of the forced heat transfer coefficient in a high turbulence environment [14]. Indeed, inside autoclaves it is common to observe a highly inhomogeneous field of motion, which goes against the prerequisites for a successful curing process. In order to reduce production costs, the logical thing to do would be to take advantage of tools with sizes and/or materials that reduce the time required for heating. However, in order to avoid distortions at the end of the curing process, it is necessary to manufacture tools with a large size and thickness. Furthermore, it is usual to deal within the same batch with 'parts' (tool and composite) that are heterogeneous with each other, i.e. with different heat transfer rates, and this leads to further difficulties in managing polymerization times [26]. Having several parts inside the autoclave at the same time also makes it clear how crucial it is to study their positioning in the chamber, as this clearly affects their polymerization times. Any strategy that is adopted with the aim of reducing the time the part spends in the autoclave, as well as the cost of carrying out the curing process, must, however, be balanced with the knowledge that a homogenous temperature field must be achieved within the machine. The polymerization process is in fact strongly linked to the thermal behaviour of the moulds used [28]; in order to control the heating process, it is usual to place thermocouples on the composites that measure the polymerization temperature in real time. An inhomogeneous temperature field (which can be generated through the phenomenon of forced convection and also due to so-called shading effects), in fact, affects the quality of the composite parts and can lead to residual stresses, voids and other production defects of the composite parts [32]. In this respect, it is possible to recognise two types of residual stress groups, those on the microscale and those on the macroscale [25]. The former develop between the fibres and the resin, but are self-balancing and do not lead to large deformations. On the other hand, macroscale residual stresses are the source of large dimensional changes. Overall residual stresses may be thermoelastic, and therefore reversible, or non-thermoelastic and permanent. The latter, which are clearly the ones we need to pay most attention to, are determined by very complex mechanisms such as the degree of polymerization, volume fraction gradients of

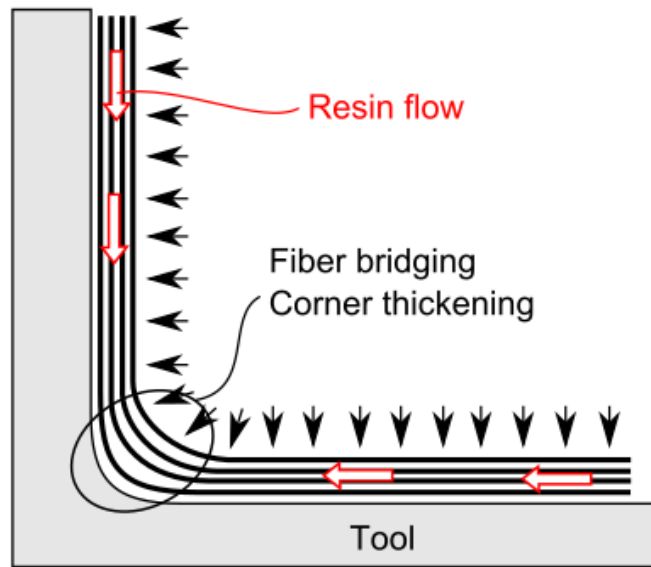


Figure 1.2: Effect of resin flow[25]

the fibres, chemical shrinkage of the resin and so on.

It is precisely the degree of polymerization that is one of the most important characteristics in determining whether or not the curing process has been successful. In the literature, this aspect is measured using different techniques. For example, Juan A. García-Manrique et al. [31] discuss Raman spectroscopy technology; it shows us how the degree of polymerization is directly related to the increase in temperature peaks. This technique, together with thermal analysis, provides relevant information for modelling the kinetic behaviour of resins in composite materials, thus allowing a clear improvement in associated problems such as shrinkage or surface defects. A further methodology is the one investigated by S. Anandan et al. [29]; this is a post-curing phase that is performed with the aim of increasing the degree of polymerization and cross-linking of composite laminates. In the experiments that have been carried out in this regard, it has emerged that this phase immediately following curing is beneficial for laminates produced using a modified polymerization cycle; the modifications consist of the introduction of a gradual temperature ramp that reduces the thermal peak while decreasing the degree of polymerization, which is, however, restored to acceptable values thanks to the post-curing phase. What is customary, therefore, is to give ample scope to the analysis of heat transfer in the chamber, especially where the air flow is most disturbed. What will be done in the following paragraphs is to introduce the concept of the autoclave and to explain its operation during a classic composite curing process, while also dwelling on the description of the internal fluid dynamics that take place and that are of crucial importance for a perfect understanding of the entire production cycle.



Figure 1.3: Example of an industrial autoclave. There are many types and sizes depending on what types of processing they need to accommodate inside.

### 1.3 State of art: Autoclave

The term autoclave indicates a type of hermetic closure in which the pressure difference between the inside and outside of the container facilitates the seal. In other words there is a kind of tailgate that leans on the opening from the inside of the container with the interposition of a gasket. Initially this door is kept in place by means of springs or screws with limited pressure; when the pressure level is sufficient this door tends to close by pressing against the seat with a force directly proportional to the pressure, so as to increase its tightness [36]. This type of locking system is normally used, for example, in large industrial containers for the fermentation of musts and in sterilisation ovens used in hospitals and in the food industry. However, autoclaves can also be found in many other areas: the glass industries, for example, use them for the stratification of laminated glass; more and more widespread are autoclaves for composite materials (in the aeronautical, naval, aerospace, etc.) that are used for the polymerization of carbon fibres and thermoplastics; also in the impregnation industry these machines are used for drying processes, as well as for impregnation [41]. The autoclave is a machinable machinery with horizontal or vertical axis; the control system for pressure and temperature levels is usually of type PLC ("Programmable Logic Controller") integrated to a man-machine interface [42]. Depending on the application, this industrial instrument can also reach considerable dimensions that consequently involve maintenance activities and considerable energy consumption. The market cost is therefore understandably high and may exceed the threshold of EUR 1 million.

### 1.3.1 Historical background

The history of the autoclave dates back to 1679. The autoclave with valve (safety door), which was also a prototype steam boiler, was invented by the French physicist, Denis Papin. At that time it was called "Papin's boiler". It was also used as a pressure cooker. His action was first demonstrated in 1682 at a reception for members of the Royal Society in London, where food could be autoclaved and served. Since then there have been many changes in the production and use of autoclaves. Most processes have been automated: currently the equipment is electronically controlled, supplied with distilled water or connected to the water supply system, and the processes are stored electronically. Some devices also have the function of a printer and are equipped with a display where you can see the various phases of operation of the machine [39]. If, as we have previously anticipated, the diffusion in some areas of the use of the autoclave involves the construction of large machinery, we must also point out that technological progress has made it possible to reduce the size of these machines in other sectors where, in fact, the practicality of their use is essential. Now this technology is widely used and indispensable in the industrial processes of many companies; consequently the interest in improving these machines is growing, as are all the studies and research that are developed in this regard.

### 1.3.2 Autoclave cycle

Autoclaves are widely used for the production of high-performance components, such as the previously described Carbon-Fiber-Reinforced-Polymers [20]. The main reason for this increasingly common use of the autoclave is due to the fact that in this way, more than in others, very high quality parts can be obtained. In addition, the use of the autoclave allows composite materials to be processed and fabricated directly into large, complex structures [3] without the need for time-consuming machining and fastening operations. This significantly reduces production costs. In most cases, a complete autoclave cycle involves a series of heating and cooling phases the material of interest and its substrate are exposed to [14]. The autoclave cycle is characterised by low heating rates with a maximum temperature of 180°C with a duration that is normally between 7 and 14 hours in order to allow the part to be cured correctly, avoiding possible damage due to the material overheating as a result of the exothermic polymerization reaction. To ensure a certain degree of polymerization without a temperature overshoot, composite processing cycles typically consist of heating ramps and holding times. As well described by Bhone [30], the flow in the autoclave enters the chamber through an annular space between the inner and outer wall. The flow at the bottom follows the shape of the hatch and collides with the flow from the top. Both flows are then deflected to the rear of the autoclave, creating recirculation zones. The flow takes the path of least resistance through the cross-section of the free flow over the load. Therefore, the flow velocity near the load surface and the heat transfer coefficient are relatively low [17].

The main objective of this 'process cycle' is to polymerize the resin according to the previously describe kinetics by promoting its flow within the laminate in order to achieve

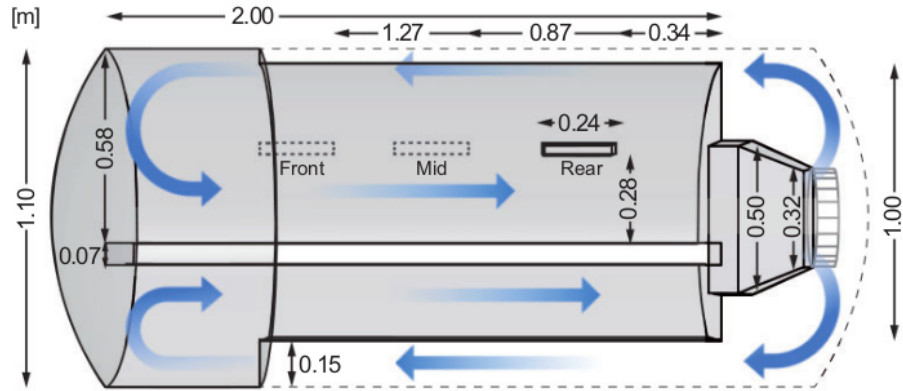


Figure 1.4: Autoclave air flow [30]. The image describes what is usually the path that is taken by the flow before it is fed into the chamber. The latter diffuses, reaches the bottom of the machinery and is collected and recirculated.

an optimal resin content and a void-free part. At the same time, it must be ensured that the structure produced respects the desired shapes, since in the vast majority of cases, these parts are used in applications with strict tolerance requirements [3]. Over the last few decades, researchers have realised that in order to obtain high-quality parts, the usual iterative procedure of trial and error, in addition to having a non-negligible economic burden, didn't guarantee the desired results. In the literature we therefore find various attempts to approach this through modelling. The computational modelling of the autoclave process, makes it possible to examine a very large number of potential machining scenarios and part and tool designs in order to verify the uniformity of resin polymerization and the deformation of the structure before building a single real part [3]. This creates 'virtual parts' that can predict machining results (such as process-induced deformation) a priori.

## 1.4 Fluid dynamics setup

Thoroughly investigating the heat transfer and airflow pattern within the autoclave gives a better understanding of the situation and how to intelligently position workpieces within the machine, and also reduces cycle times. A good analysis also requires the evaluation of certain boundary parameters such as internal pressure and inlet air velocity. For the generation of the physical model, in addition to the usual basic fluid-mechanical and thermodynamic equations, knowledge of the thermal properties of the material, the exothermic heat released and the temperature-dependent polymerization reaction kinetics is also required [17]. As has already been mentioned in the description of the curing process, the heating mechanism that dominates within an autoclave process is that of forced convection (since classic temperatures during an autoclave process remain below 200 degrees centigrade and the thermal contribution of radiation can therefore be

neglected [35]). This phenomenon greatly influences heat transfer, which is characterised by a heat transfer coefficient (HTC). Forced convection can be described by the HTC  $h$  according to the following expression [35]:

$$h = \frac{\dot{Q}}{A(T_w - T_f)} \quad (1.2)$$

where  $\dot{Q}$  is the total heat flow,  $A$  is the surface area,  $T_w$  is the wall temperature, and  $T_f$  is the bulk temperature. This is an analytical equation in simple form for the determination of the heat transfer coefficient; a more complicated approach can possibly be used by computational means. If a mass calorimeter is used, the equation 1.1 becomes [35]:

$$h = \frac{mc_p \frac{dT}{dt}}{A(T_f - T)} \quad (1.3)$$

where  $m$  is the plate mass,  $c_p$  is the heat capacity,  $T_f$  is the autoclave air temperature,  $T$  is the plate temperature, and  $A$  is the plate area of the top and bottom surfaces. The thermal mass calorimeter most often consists of an aluminium plate with thermocouples attached to the centre of the plate. For the correct use of this object, assumptions are made for a better evaluation of the heat transfer parameter:

1. Homogeneous temperature distribution within the calorimeter.
2. Perfect insulation of the plate edges.
3. No heat transfer through the sub-plate.

Meanwhile, heat conduction occurs in solid regions. In a solid region, the energy equation owing to heat conduction can be defined as follows [35]:

$$\frac{\partial(\rho_s c_s T)}{\partial t} = \text{div}(\lambda \text{div}T) + S_T \quad (1.4)$$

where  $\rho_s$  is the density of a solid,  $c_s$  is the specific heat of a solid, and  $S_T$  is the internal heat source. In general, the polymerization process of a thermosetting resin is very complex and also involves a series of chemical reactions. For this reason, another fundamental aspect of the fluid dynamics of an autoclave is the reaction kinetics of the resin [3] described mathematically by means of kinetic polymerization equations; they can be used to evaluate the temperature distribution during the polymerization of thermosetting resin systems. Using multiple isothermal DSC experiments, the cure kinetic equation can be derived. This equation accounts for the interplay between kinetics-controlled and diffusion-controlled reaction mechanisms [29]:

$$\frac{d\alpha}{dt} = \sum_{i=1,3} K_i \alpha^{m_i} (1 - \alpha)^{n_i} + \sum_{j=2,4} \frac{K_j \alpha^{m_j} (1 - \alpha)^{n_j}}{1 + e^D j \{ \alpha(\alpha_{c0,j} + \alpha_{cT,jT}) \}} K_l = A_l e^{\left(\frac{-E_{A,l}}{RT}\right)}, l = i, j \quad (1.5)$$

where  $A_n$  is the Arrhenius constant,  $E_{A,n}$  is the activation energy,  $R$  is the universal gas constant,  $m_i$  and  $n_i$  are reaction order-based fitting constants,  $D_j$  is the diffusion constant,  $T$  is the temperature,  $a_{c0}$  is the critical degree of cure at absolute zero, and  $a_{cT}$  accounts for the increase in critical degree of cure with temperature. These equation constants, together with the activation energies, regardless of the model used (which may be mechanistic or empirical) must be obtained experimentally.

#### 1.4.1 Numerical studies of computational fluid dynamics (CFD)

The development of numerical models, as it has already been said, is necessary for virtual design and optimisation of the composite manufacturing process, avoiding costly trial-and-error approaches (an approach that is often preferred to compensate for geometric variations such as interlocking angle) [25]. Therefore, if one could foresee well in advance all those consequences that result from the generation of residual stresses in the part, following the curing process of the composite, it would be possible to circumvent this costly process by trial and error during the assembly phase. In this regard, research and development in this field is striving towards ever more powerful computational models. The literature shows how the use of computational fluid dynamics (CFD), specifically, significantly aids the efficiency of heat transfer coefficient (HTC) modelling within the autoclave, while maintaining a high level of product accuracy. As explained by Zhu [35], the main challenge of a CFD approach for the estimation of thermal boundary conditions (crucial for providing accurate simulation results) is to find efficient modelling and meshing to compensate for the increased complexity of the mould and composite structures. What we set out to do with this work is to analyse the behaviour of the flow in an autoclave, in the absence of any kind of ingobar, in an empty chamber. In this way we intend to extrapolate kinetic energy values, in particular, but not only, which can then be useful as input for a more in-depth and complete study of the HTC. Hence, the concept is to set upstream, in a sense, of the extrapolation work from CFD simulations done in the work of Weber et al [23][28].

#### 1.4.2 RANS approach and unresolved issues

The turbulence model that is chosen for the fluid dynamic analysis of the internal environment of an autoclave is one of the most influential aspects due to the turbulent nature of the flow in the chamber. However, there is no consensus on the choice of a turbulence model for CFD simulations inside an autoclave, even though, in most studies, the RANS model (standard  $k-\epsilon$ ,  $k-\omega$  SST or Spalart-Allmaras whatever) is chosen. A detailed review of the literature [27] indicates that most CFD validation studies usually only use the stationary Reynolds-averaged Navier-Stokes (RANS) approach. However, RANS models fail to best reproduce turbulent kinetic energy, which is often too low, because they underestimate the effect of transient flow characteristics. While in the case of RANS simulations what is done is to solve the mean flow by modelling the entire turbulence phenomenon, the LES method, on the other hand, solves exactly both the mean flow and the large scales of turbulence, modelling turbulence only at the small scales.

In the case of the study by T. van Hooff et al. [27], which focused on the validation of cross-ventilation flow through a generic enclosure, clear differences (between RANS and LES) in the predicted flow ranges of mean velocity, turbulent kinetic energy and general flow pattern are revealed. The RANS model specifically is not able to correctly capture the dissipation of turbulence, unlike the LES, which is able to make more accurate predictions with a sufficiently small time step and adequate grid resolution [21][15]. The main reason for this superior accuracy on the part of large eddy simulations lies in the reproduction of anisotropic fluctuations in flow velocity. The latter are mainly caused by transient momentum transfer mechanisms in the flow that cannot be reproduced by simple RANS methods [33]. In the thesis path presented here what we intend to do is just to use a LES method, with the Smagorisky filter for the resolution of subgrid stairs, inside a model of autoclave free of any piece, with the sole purpose of understanding how it is possible to make homogenous an anisotropic and strongly heterogeneous turbulent motion field.

## 1.5 Thesis outline

Having laid the groundwork for understanding what an autoclave is and the thermal processes it houses, with all the difficulties that come with it, we can delve more into the actual thesis course. In the second section of the thesis, after introducing the concept of turbulence and turbulent flow, will be put under the magnifying glass the physical and mathematical model that have inevitably characterized the skeleton of the simulations and that have allowed, in fact, to model at best the real physical problem (which will be presented in detail in the third part) and around which the whole project revolves. The fourth chapter is nothing more than a discussion on the numerical methods used for the resolution of the motion field, with a syntactic treatment of the program used for the simulations, PLUTO 4.4.2. This chapter prepares us best to deal with the following, in which the results are presented. Finally, it is in the sixth part of this thesis that the sum of the entire project is drawn, illustrating the conclusions reached and proposing possible developments that could be considered for future analysis.



## Chapter 2

# Physical-mathematical model

In this second chapter we will go into the concept of turbulence and everything related to it. We will enter the debris by analyzing the Navier-Stokes equalization and various turbulence patterns. Finally, we will also talk about spectral analysis and how this is an extremely useful tool to better describe the characteristics of a turbulent flow (characteristics such as anisotropy and homogeneity, for example).

### 2.1 Navier-Stokes Equations

The Navier-Stokes equations are partial derivative equations that describe, from a physical point of view, the motion of a viscous fluid. Mathematically speaking, they represent mass and momentum balance equations and play a fundamental role in engineering because they enable the analysis and description of countless scientific phenomena (wave motion in the oceans, the movement of large atmospheric air masses, etc.). Within these equations, we therefore find mechanical and fluid quantities, such as velocity, pressure, density and temperature, which are assumed to vary continuously from point to point through the fluid [16]. When describing equations of this type, it is also necessary to decide, for the sake of consistency, which coordinate system is being used: in our case, we will refer to the Eulerian reference system<sup>1</sup>.

#### Continuity equation

$$\frac{\partial \rho}{\partial t} = \nabla \cdot (\rho \mathbf{U}) \quad (2.1)$$

This is the representation of the conservation of mass in differential form, where both density and velocity vector are functions of space and time. If a fluid with constant density is treated, then a simplification of the continuity equation can be obtained:

---

<sup>1</sup>Flow properties are considered as functions of space and time, e.g. in the case of velocity we would write  $\mathbf{u} = \mathbf{u}(\mathbf{r}, t)$ . The observer is able to observe, in its entirety, the field of any of the fluid motion's own quantities at each instant in time, without, however, having information about the trajectory of the individual fluid particle.

$$\nabla \cdot (\mathbf{U}) = 0 \quad (2.2)$$

This expression above represents a solenoidal velocity field. Concealed within it is the time dependence of the velocity field: at first glance, one might think that this is a stationary flow, but the assumption of a stationary velocity field has never been made.

**Momentum equation (N-S)** The momentum equation in differential form is represented as follows:

$$\frac{\partial \mathbf{U}}{\partial t} + \mathbf{U} \cdot \nabla \mathbf{U} = -\frac{\nabla(p)}{\rho} + \nu \nabla^2 \mathbf{U} + \mathbf{F} \quad (2.3)$$

dove  $\nu = \frac{\mu}{\rho}$  is a property of the fluid and is called kinematic viscosity. Two new quantities are then introduced, pressure and kinematic viscosity: the former is associated with the isotropic interactions that occur between two adjacent fluid volumes; the latter reflects the 'shear' stress, which is greater the larger the fluid's viscosity. The kinematic viscosity is then multiplied by the velocity Laplacian describing the expansion and compression motions of the fluid volume considered for the differential analysis. In the second member of the equation 2.3, finally, the vector also appears  $\mathbf{F}$  representing field forces (e.g. the presence of the gravitational field). We note how this equation is non-linear in the variable  $\mathbf{U}$ . This non-linearity characteristic comes from the dual behaviour of the velocity vector in determining the acceleration of a fluid particle. As can be easily understood, this characteristic of the momentum balance equation makes its analytical resolution very complicated, consequently the various results that can be obtained are experimental and/or computational in nature. The continuity equation 2.1 and the momentum equation 2.3 thus represent the physical laws that will be applied to all fluid particles of any flow studied [16]. The number of unknown variables is perfectly matched to those of the available equations: the unknown variables are in fact 4 (one scalar, the pressure<sup>2</sup>, and one vector, the velocity, which consists of 3 components); the equations congruently are 4, one scalar and one vector. As far as boundary conditions are concerned, where one or more fixed walls are present, the impermeability condition is met [6]

$$\mathbf{n} \cdot \mathbf{U} = 0, \quad (2.4)$$

with  $\mathbf{n}$  which is the normal to the wall, and, along with it, that of no-slip [6]

$$\mathbf{U} - \mathbf{n}(\mathbf{n} \cdot \mathbf{U}) = 0 \quad (2.5)$$

As we have already seen above, one of the most important characteristics of turbulent flow is that it is vortical (and therefore rotational). Together with the mass and momentum balance equations, we must also expound the vorticity equation, which is

---

<sup>2</sup>It must necessarily be an intrinsic variable for there to be enough variables to satisfy the basic laws of mechanics [16].

obtained from the Navier-Stokes (momentum) equation by applying the rotor operator to it:

$$\frac{D\boldsymbol{\omega}}{Dt} = \nu \nabla^2 \boldsymbol{\omega} + \boldsymbol{\omega} \cdot \nabla \mathbf{U} \quad (2.6)$$

The pressure term ( $-\nabla \times \nabla p / \rho$ ) vanishes for constant-density flows. Always at the second member of the equation 2.6 the term  $\boldsymbol{\omega} \cdot \nabla \mathbf{U}$  also appears the so-called vortex-stretching term, a phenomenon characteristic of turbulent flow, which makes turbulence a three-dimensional phenomenon. In its absence, in fact, the one non-zero component of vorticity evolves as a conserved scalar, characteristic of two-dimensional flows. Finally, if there is also independence from rotation and reflection of the coordinates of the relative reference system then the motion field is also said to be statistically isotropic [6].

### 2.1.1 Reynolds number

After having introduced the equations of motion and given the mathematical and physical background on how to approach the study of a turbulent flow (but not only), it is fitting to carve out some space to give a physics interpretation of the Reynolds number and how it is so important in understanding the dynamics of a physical process [16]. The Reynolds number is defined as the ratio between inertial phenomena and viscous:

$$Re \sim \frac{\text{inertia forces}}{\text{viscous forces}} \quad (2.7)$$

This means going straight back to the Navier-Stokes equation:

$$Re = \frac{UL}{\nu} \sim \frac{|\mathbf{U} \cdot \nabla \mathbf{U}|}{|\nu \nabla^2 \mathbf{U}|} \quad (2.8)$$

Observing the relation 2.8, it is possible to make some considerations in this respect; for **Reynolds numbers much smaller than unity**, viscous forces dominate over inertial ones. Again starting from the Navier-Stokes equation(2.3), we obtain

$$\nabla p = \mu \nabla^2 \mathbf{U} \quad (2.9)$$

There is a perfect balance between local pressure and viscous forces. This equation (2.9) is called creeping motion and accepts reversible solutions<sup>3</sup> [16]. Furthermore, an important characteristic of low Reynolds number flows is that viscous interactions extend to large distances [16]. For **high Reynolds number** flows, on the other hand, the viscous phenomenon is irrelevant compared to the inertial one and can therefore be neglected. In this case, the result leads us to much more complicated considerations; despite the fact that the result of increasing Reynolds number leads the viscous forces to decrease more and more, there are regions where this consideration 'loses its solidity', namely within the boundary layer[16]. Here, in fact, the flow develops within spatial scales that are much smaller than the characteristic scale of the system (difference that

<sup>3</sup>That is, solutions with the same streamline pattern but opposite pressure gradients [16]

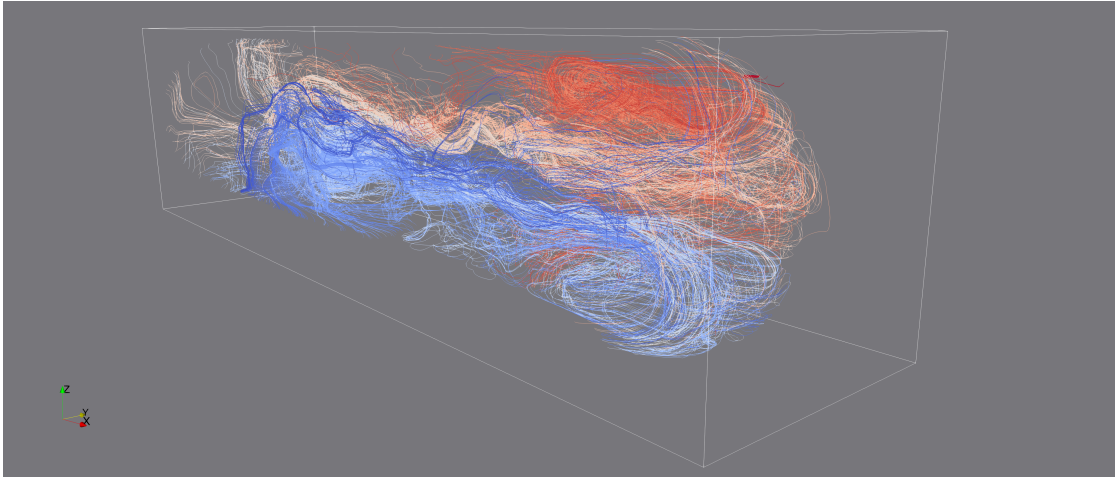


Figure 2.1: Streamlines of a turbulent flow inside an autoclave. The image was produced with ParaView [11] from one of many simulations performed.

becomes more and more pronounced as the Reynolds number increases :  $Re^{-\frac{1}{2}} \sim \frac{\delta}{L}$ . This is called boundary layer thickness  $\delta$ .

## 2.2 Concept of Turbulence

The most natural and, at the same time, the most complex condition of a flow is turbulent, a flow regime characterized by chaotic, stochastic property changes, such as rapid variation of pressure and velocity in space and time [13]. This fascinating complexity has attracted the attention of naturalists, philosophers, and poets alike for centuries [4]. In everyday experience there are hundreds of examples we encounter of turbulent flows: the smoke of a cigarette, the mixing of milk and coffee inside a cup, the irregular trail of a river downstream of a bridge pylon etc [7]. However, turbulence is also observed in flows such as atmospheric, oceanic, but also, for example, inside the planets and in the so-called stellar winds. Continuing to expose examples of turbulent flows, even the vast majority of engineering flows, such as in air conditioners and combustion engines, as well as most kitchen flows are turbulent [34]. These complex flows have multiple components that could be a combination of speed, temperature, density, and magnetic fields. Their complexity seems daunting, however, the mathematical models and tools developed over the past two centuries provide a reasonable understanding of such flows [34].

What is hard to understand about the phenomenology of turbulence is the effect it can have on the overall magnitude of the flow and how the latter can be so profoundly affected by a phenomenon that appears invisible and hidden. In all the examples made the characteristics that most of all shared almost all these physical phenomena are certainly the instability, the irregularity and also the unpredictable, random and chaotic movement of the dynamic structures that characterize their physics. Unpredictable

is the term used to indicate a random feature of non-uniqueness, for example the flow velocity field. This brings us closer to a clearer understanding of how turbulent flow development is extremely sensitive to small variations that affect both initial and boundary conditions [6]. Another important feature of turbulence is its ability to diffuse (and dissipate) very quickly and irregularly as well as much more effectively than the molecular agitation (can become two or even three orders of magnitude higher than the molecular diffusivity). Velocity fluctuations induced in the fluid by turbulent motion are capable of transporting a quantity (whether scalar or vector) even in the absence of mean motion [7]. The effectiveness of turbulence for transporting and mixing fluids is of prime importance in many applications [6]. Already from these first descriptions it can be well understood how the presence of a flow in turbulent regime can guarantee, for sure, better results than those that can be reached by a flow in laminar regime. For this reason in many fields of engineering it is usual to deal with turbulent flows, just think of pumps or compressors, or the fields of motion that are established around an airplane, a boat or a submarine. The key to the onset of turbulence in the flow is the loss of stability that occurs more and more rapidly as a result of the change in one of its control parameters. [4]. The most important control parameter is the Reynolds number,  $Re$ , which measuring the relative importance of inertial forces to viscous forces. In attempting to model the development of any type of turbulent (or even laminar that is) flow, it is necessary to have specific tools, physical-mathematical models that allow us to describe in detail the flow characteristics. The governing equations are the clearest example of this type of models and are embodied in the so-called Navier-Stokes equations. In the case of turbulent flows (and this tends to mean high Reynolds number flows), the enormous amount of information that comes from studying these equations is a double-edged sword, making a direct (DNS) approach impractical [6]. Thus, for the high Reynolds number flows that are prevalent in applications, the natural alternative is to pursue a statistical approach, which gets a real practical value. Over the years, various techniques of studying these types of flows have been experimented, allowing them to be categorized and better understood. One of those that has certainly been most successful is to distinguish between the small scales of turbulence and the large scales of motion. In fact, what you can notice when you reach a high number of Reynolds is the so-called separation of the scales: the largest scales are those that maintain strong links with the environment around them and therefore with those that are the boundary conditions, unlike the small scales of turbulence that instead tend to take on an almost universal character, as if they lost memory of what was their genesis (although in saying this you are partially making a mistake: turbulence is a highly nonlinear phenomenon, and the "non-linearities" it produces in turn bring with them long-term interactions that make even the smallest scales somehow related to the geometry of the system) [6]. To fully understand this discourse it is necessary to analyze what is undoubtedly one of the characteristics that distinguish the phenomenon of turbulence, the energy cascade.

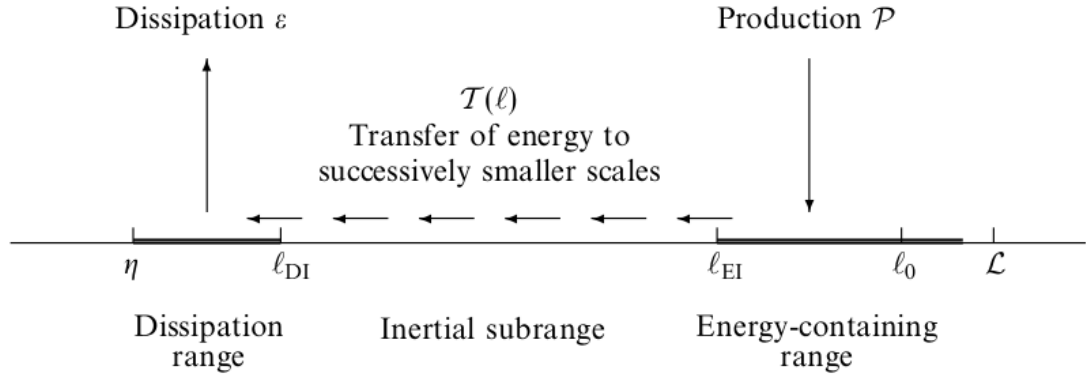
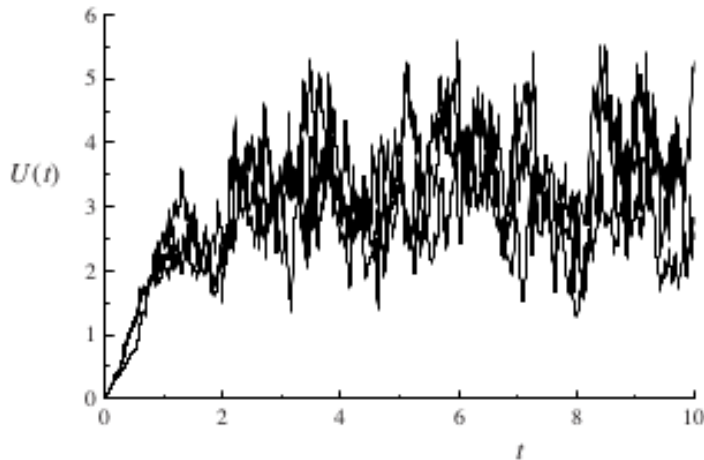


Figure 2.2: Energy cascade [6]

### 2.2.1 Energy cascade

Turbulent motion is a "continuous instability phenomenon", containing fluctuations, in three dimensions (as evidenced by the presence of the stretching and tilting phenomena), of different scales. In many examples from everyday life (some of which have already been explained above) there is underlying the concept of turbulence and in particular the concept of instability of large vortices that break into smaller and smaller vortices thus giving rise to the energy cascade [6]. It is important to understand that this is an intrinsic behavior of the system and is therefore activated even without the need to introduce energy.

Specifically, this is a true transfer of kinetic energy from larger to smaller structures. Analyzing the equations of motion, one realizes how this task is addressed by the non-linear terms, which do not affect the energy content. The question that tends to be asked, however, is whether this type of cascade can continue indefinitely; obviously the answer is negative, specifically we see how the viscosity present within the system places a "cutoff" on the minimum size of structure that can be generated in a flow, and this cutoff obviously depends both on the value of viscosity  $\nu$  and on how quickly the energy diffuses within the various scales of the system [7]. Interestingly, experimental evidence shows that when viscosity decreases, losing what is its dissipative power, the value of kinetic energy is not conserved; on the contrary, what is noted is the decrease of the smaller scales of motion and the increase, instead, of the gradients. This means that turbulence is, in fact, an inherently dissipative phenomenon and therefore the viscous term can never be completely neglected [7]. The vortices that animate the turbulent flow are called 'eddies'. A "eddy" eludes precise definition and moreover is a term not quite correct to render the concept well, but it is very useful in helping us develop the concept of turbulence. It is conceived as a localized turbulent motion within a region of size that is at least moderately coherent over this region [6]. In turn a large vortex may also contain smaller vortices. As can be easily deduced, large vortices are anisotropic and are, as mentioned above, conditioned by boundary conditions. Kolmogorov [1], on

Figure 2.3: Sample paths of  $\mathbf{U}(t)$  [6]

the other hand, found that at a sufficiently high Reynolds number, smaller scales of turbulent motion can be considered locally isotropic. These structures then acquire a universal shape, uniquely determined by two parameters:  $nu$  and  $epsilon$  (the dissipation rate). Thus is born the concept of Kolmogorov scale, the smallest dimension present in a turbulent system in which the energy cascade breaks down and the inertial and viscous terms assume a comparable size.

## 2.3 Statistical description of turbulent flow

Every time a flow changes and evolves because of its instability, it loses the ability to predict the details of its motion. There is therefore a need to take a kind of statistical approach, the best way to describe the random characteristics of turbulence (which occurs however through organized forms) [16]. The statistical approach is, usually, formulated from averages quantities; they represent a very powerful instrument for the description of the motion of any type of flow because conditions are created for which several points of the flow have the same values, which are precisely mediated values.

### 2.3.1 Reynolds equations for turbulent flows

The statistical approach, described previously, begins with explicitly distinguishing within the velocity and pressure field, both mean and fluctuating values. At each point, the individual physical quantity, such as the x-component of velocity, for example, will be decomposed in the following way:  $\langle U \rangle + u$ . The uppercase component indicates the mean motion component<sup>4</sup>, while the lowercase identifies the fluctuating component (which by

---

<sup>4</sup>One speaks in this case of ensemble averaging, i.e. a large number of identical systems are considered and the average, among all systems, of that precise magnitude is acquired [16]. It is customary to refer

definition we know to be zero,  $\langle \mathbf{u} \rangle = 0$ ). This type of approach is called *Reynolds decomposition* and can be applied to the balance equations 2.2 and 2.3.

This follows from the continuity equation:

$$\nabla \cdot (\mathbf{U}) = \nabla \cdot (\langle \mathbf{U} \rangle + \mathbf{u}) = 0. \quad (2.10)$$

Applying the averaging operator to this equation, and taking into account the possible commutation between the averaging and divergence operator, then we obtain:

$$\nabla \cdot (\langle \mathbf{U} \rangle) = 0, \quad (2.11)$$

then, by subtraction:

$$\nabla \cdot (\mathbf{u}) = 0, \quad (2.12)$$

For momentum, the procedure is slightly more complicated due to the presence of the usual non-linear terms. The final result is (in this case, for simplicity's sake, we opt for writing in index form):

$$\frac{\partial \langle U_i \rangle}{\partial t} + \langle U_j \rangle \frac{\partial \langle U_i \rangle}{\partial x_j} = -\frac{1}{\rho} \frac{\partial \langle p \rangle}{\partial x_i} + \nu \frac{\partial^2 \langle U_i \rangle}{\partial x_j \partial x_j} - \frac{\partial \langle u_i u_j \rangle}{\partial x_j} \quad (2.13)$$

This is the Reynolds equation. The fundamental difference with the Navier-Stokes equation lies in the presence of a new term, Reynolds stresses  $\langle u_i u_j \rangle$ . They, which appear as unknowns in the Reynolds equations, are determined by a turbulence model (closure problem). This, in fact, results from the presence of too many unknown variables within the system of equations. The Reynolds stresses are the components of a second-order tensor, which is obviously symmetric; the diagonal components are *normal stresses*, while the off-diagonal components are *shear stresses* [6]. It is then possible to calculate the turbulent kinetic energy from this tensor:

$$k \equiv \frac{1}{2} \langle u_i u_i \rangle \quad (2.14)$$

Reynolds stress arises from the correlation<sup>5</sup> between two velocity components at the same point in space. A non-zero value of this term therefore implies the two components in question are not independent of each other [16].

### 2.3.2 Homogeneous isotropic turbulence

In a turbulent flow, the velocity  $\mathbf{U}(\mathbf{x}, t)$  is a time-dependent random vector field [6]. In this regard, it is customary to speak of a statistically stationary, homogeneous and isotropic velocity field; these phenomena are recurring especially when dealing with

---

to a time average.

<sup>5</sup>Correlation is the 'measure' of the statistical dependence between two quantities (such as two velocity components). For a more detailed discussion, please refer to specific texts such as [6]

turbulent flows, and therefore statistical type treatments. The velocity field  $\mathbf{U}(\mathbf{x},t)$  is *statistically stationary* if all statistics do not change from one time instant to another. Similarly, the same field is *statistically homogeneous* if all its statistics remain unchanged from one point in space to another [6]. When one studies a flow that becomes turbulent from a certain moment onwards, within its evolution, then one notices how the production of turbulent energy is maximum for the first instants (linked to the characteristic length of the system in which the analysis is carried out) and then slowly decays until it is negligible. At this point, one can speak of turbulence that is essentially isotropic and homogeneous, where the production term in the turbulent kinetic energy<sup>6</sup> equation has been completely cancelled out by the phenomenon of viscous dissipation [16].

## 2.4 Spectral analysis

Another method of discovering the scales associated with turbulent flows is spectral analysis and, particularly, Fourier analysis [16]. Normally, the turbulent signal is acquired experimentally through the use of techniques such as hot-wire anemometry, Laser Doppler Anemometry (LVD), PIV and so on. Within this thesis path, however, a different route was taken, something one does not do often, as one could easily make mistakes; the necessary data were in fact collected directly from computational simulations and were then processed through the use of a simple Matlab code (which will be discussed in more detail when the results are presented). In this specific case, the spectral analysis technique was used to understand in more detail the benefit of using certain perturbative inputs, positioned here and there within the autoclave, in terms of the level of homogeneity achieved.

## 2.5 Turbulence models and numerical simulations

As has been repeated several times within this chapter, in a turbulent flow the velocity field  $\mathbf{U}(\mathbf{x},t)$  is three-dimensional, time-dependent and random. All these characteristics together make a simple theoretical analysis very difficult, especially if we then add, within the equations that describe its essence, the presence of non-linear terms (such as the convective term and the pressure gradient, the latter when written in terms of the velocity in the Poisson equation<sup>7</sup>) [6]. Technological advancement over the last few decades has certainly lent a big hand in this respect; indeed, the ability of computers nowadays to process and manipulate a large amount of data extremely quickly therefore

---

<sup>6</sup>

$$\frac{1}{2} \frac{\partial \langle u^2_i \rangle}{\partial t} + \frac{1}{2} U_j \frac{\partial \langle u^2_i \rangle}{\partial x_j} = - \langle u_i u_j \rangle \frac{\partial \langle U_i \rangle}{\partial x_j} - \frac{1}{2} \frac{\partial}{\partial x_j} \langle u^2_i u_j \rangle - \frac{1}{\rho} \frac{\partial}{\partial x_i} (p \langle u_i \rangle) + \nu \langle u_i \frac{\partial^2 u_i}{\partial x_j^2} \rangle$$

(2.15)

<sup>7</sup>

$$\nabla^2 p = -\rho \frac{\partial U_i}{\partial x_j} \frac{\partial U_j}{\partial x_i}$$

(2.16)

allows for an accurate numerical analysis of these types of flows (and more). Hence, there has been a move to develop both simulations of turbulent flows, where the equations are solved for a time-dependent velocity field, and turbulent models, which on the contrary solve the equations involved for certain average quantities, e.g.  $\langle \mathbf{U} \rangle$ ,  $\langle u_i u_j \rangle$  e  $\epsilon$  [6]. In the following paragraphs, three different types of simulation approaches will be analysed specifically. They differ from one another in the type of computational effort required and, above all, in the manner and quality of motion field resolution. In particular we shall see:

- DNS.
- RANS.
- LES.

### 2.5.1 DNS: Direct numerical simulation

The Direct numerical simulation (DNS) consists in solving all the scales of motion at once. It therefore does not involve any kind of approximation and each simulation produces a single realization of the flow [6]. One does not need anything else to realise that this approach, however, has a strong limitation that lies in the high computational demand; thus, DNS simulations are most likely to be found in studies of low Reynolds number flows, as the computational cost grows as  $Re^3$ . Other aspects that come into play are the geometry of the system and the grid used within the simulation: the size of the domain must be large enough to best represent the energy content of the system (from the large scales of motion down to the small eddies); the grid spacing, on the other hand, must be small enough to capture the dissipative scales, and finally the time-step used is strongly linked to the numerical accuracy of the method used (and hence the limit imposed by the *Courant number*, for a better understanding of this see Chapter 4). All these limitations have led to an increasingly less frequent use of this type of numerical simulation, which remains more of a research tool (as it allows projects that are impossible to carry out experimentally) than a true engineering tool.

### 2.5.2 RANS: Reynolds-averaged Navier-Stokes

The RANS involve the solution of Reynolds equations (2.13) to determinate the mean velocity field  $\langle \mathbf{U} \rangle$  [6]. Depending on how the Reynolds stress term is solved, either a viscosity-turbulent model or a system of transport equations will be developed.

#### Turbulent-viscosity models

Turbulent viscosity models are based on the turbulent-viscosity hypothesis [6], formulated by Boussinesq in 1877. According to this hypothesis, in analogy to the stress-rate-of-

strain relation for a Newtonian fluid<sup>8</sup>, the Reynolds stresses are given by:

$$-\rho \langle u_i u_j \rangle + \frac{2}{3} \rho k \delta_{ij} = -\rho \cdot a_{ij} = \rho \nu_t \left( \frac{\partial \langle U_i \rangle}{\partial x_j} + \frac{\partial \langle U_j \rangle}{\partial x_i} \right) \equiv 2\rho \nu_t \langle S_{ij} \rangle, \quad (2.18)$$

where  $k = \frac{\langle u_i u_j \rangle}{2}$  is the mean turbulent kinetic energy per unit mass,  $\langle S_{ij} \rangle \equiv \frac{1}{2} \left( \frac{\partial \langle U_i \rangle}{\partial x_j} + \frac{\partial \langle U_j \rangle}{\partial x_i} \right)$  and  $\nu_t$  is the **turbulent or eddy viscosity**. In this way, if the assumption made can be considered valid (the tensor  $a_{ij}$  is aligned with the tensor  $\langle S_{ij} \rangle$ , which is not true in many types of flows!) all that remains to be modelled is turbulent viscosity  $\nu_t(\mathbf{x}, t)$ . This can be written as the product of a velocity  $u^*(\mathbf{x}, t)$  and a length  $l^*(\mathbf{x}, t)$ :

$$\nu_t = u^* l^*. \quad (2.19)$$

This is certainly the most immediate definition, but there are others, such as those obtained from algebraic models and those with one or two equations. Let us therefore proceed in order.

**Algebraic models** These are the *uniform turbulent viscosity* and the *mixing-length model*.

1. The **uniform turbulent viscosity** can be written

$$\nu_t(x, y) = \frac{U_0(x) \delta(x)}{R_T}, \quad (2.20)$$

where  $U_0(x)$  and  $\delta(x)$  are the characteristic velocity scale and lengthscale of the mean flow, and  $R_T$  – which has the interpretation of a turbulent Reynolds number – is a flow-dependent constant. The range of applicability of this model is limited to the description of mean velocity profiles in free shear flows or in very simple wall flows [6].

2. Assuming the **mixing-length model**, the turbulent viscosity is given by:

$$\nu_t = l_m^2 \left| \frac{\partial \langle U \rangle}{\partial y} \right|, \quad (2.21)$$

where  $l_m(x, y)$  is the **mixing-length** which must be clearly established a priori. This method is applicable to all turbulent flows. Turbulent viscosity written in this way, for the relationship 2.19 leads to the statement that:

---

8

$$\tau_{ij} = -\mathbf{P} \delta_{ij} + \mu \left( \frac{\partial U_i}{\partial x_j} + \frac{\partial U_j}{\partial x_i} \right). \quad (2.17)$$

$$u^* = l_m \left| \frac{\partial \langle U \rangle}{\partial y} \right|, \tag{2.22}$$

this implies that the velocity scale is locally determined by knowledge of the velocity gradient at that point; in particular  $u^*$  is zero where  $\frac{\partial \langle U \rangle}{\partial y}$  is zero, which is not always true as there are circumstances in which the velocity gradient is zero, but the turbulence viscosity exists and is non-zero.

**Turbulent-kinetic-energy models (one equation model)** The inconsistency that emerged in the definition of the mixing-length model led physicists and mathematicians to develop this model to an equation that is analogous to the kinetic theory of gases. The turbulent-viscosity becomes:

$$\nu_t = ck^{\frac{1}{2}}l_m. \tag{2.23}$$

$k(\mathbf{x},t)$  that is the turbulent kinetic energy must be estimated in some way, possibly by means of a transport equation; the product  $ck^{\frac{1}{2}}$  defines the speed scale  $u^*$ . At this point the turbulent kinetic energy has been written:

$$\frac{\partial \frac{1}{2} \langle q^2 \rangle}{\partial t} = - \langle u_i u_j \rangle \frac{\partial U_i}{\partial x_j} - \langle \epsilon \rangle + T. \tag{2.24}$$

The first term in the second member is an energy production term;  $\epsilon$ , on the other hand, represents turbulent dissipation and finally  $T^9$  encapsulates turbulent energy transfer. At this point, reworking the terms of the equation a little, i.e. writing  $k = \frac{1}{2}q$ , applying the continuity equation and renaming the diffusion term,  $I_i^{10}$ , and the production term  $\Pi$ :

$$\frac{\partial k}{\partial t} + U_i \frac{\partial k}{\partial x_i} = \Pi - \epsilon^{11} - \frac{\partial I_i}{\partial x_i}. \tag{2.28}$$

This one-equation model has a modest advantage in accuracy over mixing length model with a larger number of constants to adjust.

9

$$T = -\frac{\partial}{\partial x_j} \left\{ \frac{1}{2} \langle q^2 \rangle U_j + \langle u_j \left( \frac{1}{2} \langle q^2 \rangle + \frac{p}{\rho} \right) \right\rangle - \nu \langle u_i \left( \frac{\partial u_i}{\partial x_j} + \frac{\partial u_j}{\partial x_i} \right) \rangle \}. \tag{2.25}$$

10

$$I_i = -\frac{\nu_t}{\sigma_k} \frac{\partial k}{\partial x_i}, \tag{2.26}$$

where  $\sigma_k$  is a constant. ....

11

$$\epsilon = C_D \frac{k^{\frac{3}{2}}}{l_m}. \tag{2.28}$$

**The k- $\epsilon$  model** The k-epsilon model belongs to the family of two-equation models and is the most widely used of the various turbulence models as it does not require the knowledge, or at least the specification of a 'mixing-length'. The greater completeness that characterises this model (incorporated in many commercial CFD codes) lies in the use of two transport equations, one supporting the other, for the resolution of two turbulent quantities, which in this case are k and  $\epsilon$  [6]. Starting again from the relation 2.19, the turbulent viscosity is assumed to be:

$$\nu_t = C_\mu \frac{k^2}{\epsilon}. \quad (2.29)$$

This time the velocity scale  $u^*$  is taken as the square root of the turbulent kinetic energy,  $u^* \approx k^{\frac{1}{2}}$ ; on the other hand the length scale is formed from k and  $\epsilon$  as,  $l^* \approx \frac{k^{\frac{3}{2}}}{\epsilon}$ . Instead  $C_\mu$  one of the five model constants (its value is determined experimentally). As for the equations used to model turbulence, one is the turbulent kinetic energy equation already described above (2.28); the determination of the equation for  $\epsilon$ , on the other hand, derives from a completely empirical approach:

$$\frac{\partial \epsilon}{\partial t} + U_i \frac{\partial \epsilon}{\partial x_i} = C_{\epsilon 1} \frac{\epsilon}{k} \Pi - C_{\epsilon 2} \epsilon^2 k + \frac{\partial}{\partial x_i} \left( \frac{\nu_T}{\sigma_\epsilon} \frac{\partial \epsilon}{\partial x_i} \right). \quad (2.30)$$

The k- $\epsilon$  model has been applied to a diverse range of problems, including heat transfer, combustion, and multi-phase flows. However, it is mostly acceptable for simple flows, while it makes some errors in more complex flows (i.e. in the presence of separation, boundary layers with unfavourable pressure gradients, recirculation zones, secondary flows, strong vortices, strong curvature of flow lines, low Reynolds numbers), where the inaccuracy of the method emerges (inaccuracy stemming from the turbulent-viscosity hypothesis and from  $\epsilon$  equation) [6]. Over the decades, however, other two-equation models have been proposed. Of these, the ones that have attracted the most interest are the k- $\omega$  model and the Spalart-Allmaras model.

### Modelled Reynolds-stress transport equations

In Reynolds-stress models, model transport equations are solved for the individual Reynolds stresses  $\langle u_i u_j \rangle$  and for the dissipation  $\epsilon$ , consequently the turbulent-viscosity hypothesis is not needed [6]. The exact transport equations for Reynolds stresses has been obtained from the Navier-Stokes equations:

$$\begin{aligned} \frac{\partial \langle u_i u_j \rangle}{\partial t} + U_k \frac{\partial \langle u_i u_j \rangle}{\partial x_k} = & - \langle u_i u_k \rangle \frac{\partial U_j}{\partial x_k} - \langle u_i u_k \rangle \frac{\partial U_i}{\partial x_k} - \frac{\partial \langle u_i u_j u_k \rangle}{\partial x_k} + \dots \\ & \dots - \frac{1}{\rho} \left\{ \langle u_i \frac{\partial p'}{\partial x_j} \rangle + \langle u_j \frac{\partial p'}{\partial x_i} \rangle \right\} + \nu \left\{ \langle u_i \frac{\partial^2 u_j^2}{\partial x_k \partial x_k} \rangle + \langle u_j \frac{\partial^2 u_i^2}{\partial x_k \partial x_k} \rangle \right\}. \end{aligned} \quad (2.31)$$

However, all second-member terms require closure models as they cannot be exactly expressed by the basic variables of the model,  $\langle U_i \rangle$ ,  $\langle u_i u_j \rangle$ ,  $\epsilon$ .

### Wall functions

In describing the RANS models, the difficulty emerged in dealing with the flow characteristics near the domain contours, which in the case of a wall bounded turbulent flows, for example, are represented by walls themselves. These are regions where there are high-velocity-gradient and where the viscosity dissipation play an important role. There is always a need for modifications or additions to all proposed models. The idea of the ‘wall-function’ approach is therefore to apply boundary conditions (based on log-law relations) some distance away from the wall, so that the turbulence-model equations are not solved close to the wall [6].

Near the wall, Reynolds stresses must go to zero and thus momentum transport is dominated by viscous forces [18]. In that so-called inner region, the relevant velocity and length scales are recast in nondimensional form:

$$u^+ = \frac{u}{u_\tau}, y^+ = \frac{\rho_w u_\tau y}{\mu_w}, u_\tau = \left(\frac{\tau_w}{\rho_w}\right)^{\frac{1}{2}} \quad (2.32)$$

$u$  is velocity parallel to the wall;  $\tau_w$  is wall shear stress;  $\rho_w$  is wall density;  $\mu_w$  is wall molecular viscosity;  $y$  is the distance to the wall;  $u_\tau$  is friction velocity. In 1930, Millikan assumed, given the significantly lower thickness of this inner region, compared to the outer one, that there must be an overlap region where both the inner and outer scalar could be applied [18]. He then deduced the presence of a so-called logarithmic zone in which the mean velocity profile respected the following law:

$$\langle U \rangle = u_\tau \left( \frac{1}{k} \ln y^+ + B \right), \quad (2.33)$$

where  $k$  denotes the von Kármán constant and  $B$  is an intercept coefficient.

The wall functions are therefore designed to provide ‘robust’ boundary conditions under all circumstances and to be able to return to the relationships described in this chapter under ideal conditions [6].

### 2.5.3 LES: Large-eddy simulation

In every turbulent flow at sufficiently high Reynolds number, the statistics of the small scale motions may be assumed to have an universal form. Hence, it is customary to make a distinction between large scales of motion and smaller ones. In this regard through the large-eddy simulation (LES) approach the larger three-dimensional unsteady turbulent motions are directly represented, whereas the effects of the smaller-scale motions are modelled [6] (unlike the DNS model). This decomposition of the system’s scales brings with it the application of a spatial filter (in the ideal case the filter width is somewhat smaller than  $l_{EI}$  – the size of the smallest energy-containing motions [6]): thus the velocity field  $\mathbf{U}(\mathbf{x},t)$  will be the sum of a filtered component  $\bar{\mathbf{U}}(\mathbf{x},t)$  (represents the

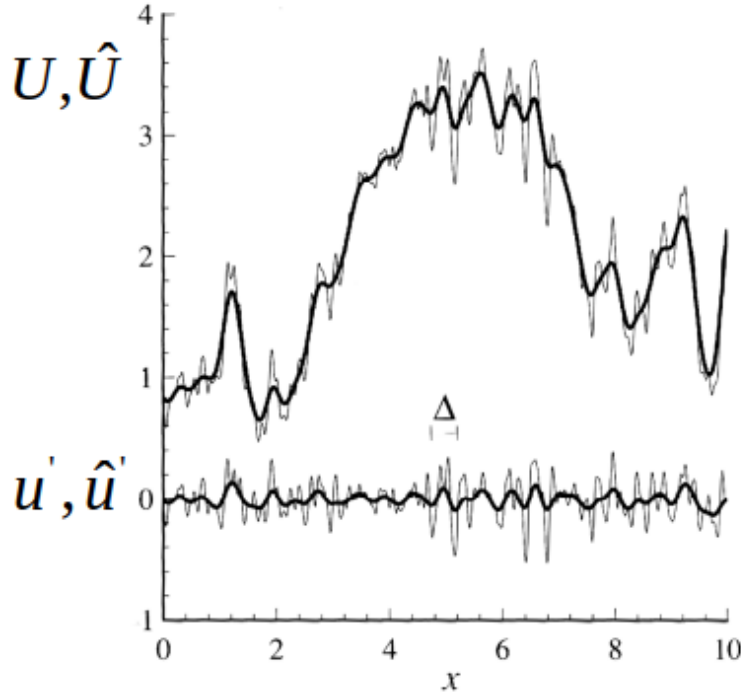


Figure 2.4: Example of filtered velocity field component, using Gaussian filter [6]. The lines in bold are those corresponding to  $\bar{\mathbf{U}}(\mathbf{x})$  and  $\bar{\mathbf{u}}'(\mathbf{x})$ .

motion of the large eddies) and a residual component  $\mathbf{u}'(\mathbf{x},t)$ . This way of acting is highly reminiscent of the RANS development procedure, although the difference between the two is substantial. In fact  $\bar{\mathbf{U}}(\mathbf{x},t)$  is a random field, and the filtered residual is not zero:

$$\overline{\mathbf{u}'}(\mathbf{x},t) \neq 0. \quad (2.34)$$

The general filtering operation consists in applying to the velocity field the convolution:

$$\bar{\mathbf{U}}(\mathbf{x},t) = \int G(\mathbf{r},\mathbf{x})\mathbf{U}(\mathbf{r},\mathbf{x})d\mathbf{r}, \quad (2.35)$$

where integration is over the entire flow domain, and the specified filter function  $G$  satisfies the normalization condition

$$\int G(\mathbf{r},\mathbf{x})d\mathbf{r} = 1. \quad (2.36)$$

In practice, the filtering operation functions as a kind of low-pass filter typical of the electronic field, removes scales smaller than  $O(\Delta^{12})$ , producing a filtered velocity field which contains only scales of size  $O(\Delta)$  and above.

<sup>12</sup> $\Delta$  is the filter width, which is usually proportional to the mesh size.

Name	Filter function
General	$G(r)$
Box	$\frac{1}{\Delta} H(\frac{1}{2}\Delta -  r )$
Gaussian	$\left(\frac{6}{\pi\Delta^2}\right)^{\frac{1}{2}} \exp\left(-\frac{6r^2}{\Delta^2}\right)$
Sharp spectral	$\frac{\sin \frac{\pi r}{\Delta}}{\pi r}$

Table 2.1: Filter functions for one-dimensional filters [6]

It is therefore understandable how important it is to choose the filter to be used for resolving the scales of motion and, above all, how this choice leads to the creation of multiple LES models.

The table 2.1 show the most commonly used filters (found in the literature).

### Filtered conservation equations

Once the mathematical structure of these spatial filters has been described, it is necessary to apply them to the governing equations (2.1 and 2.3) to try to obtain the filtered field of motion  $\bar{\mathbf{U}}(\mathbf{x},t)$ . It must be noted, however, that the filter may not commute with the spatial derivatives, to avoid this it is assumed to take a uniform (in space) filter. The evolution of the filtered flow is described by the following version of **continuity equation**,

$$\frac{\partial \bar{U}_i}{\partial x_i} = 0, \quad \frac{\partial \bar{w}'_i}{\partial x_i} = 0, \quad (2.37)$$

and the **momentum equation** (in the conservative form),

$$\frac{\partial \bar{U}_i}{\partial t} + \frac{\partial \bar{U}_i \bar{U}_j}{\partial x_j} = -\frac{1}{\rho} \frac{\partial \bar{p}}{\partial x_i} + \nu \frac{\partial^2 \bar{U}_i}{\partial x_j \partial x_j} \quad (2.38)$$

The filtered product  $\bar{U}_i \bar{U}_j$  is different than the product of the filtered velocities  $\bar{U}_i \bar{U}_j$ . The difference is the residual-stress tensor (less density  $\rho$ ), defined by:

$$\tau_{ij}^R \equiv \bar{U}_i \bar{U}_j - \bar{U}_i \bar{U}_j \quad (2.39)$$

By introducing two additional filtered quantities, the momentum balance equation can be rewritten as follows:

$$\frac{\partial \bar{U}_i}{\partial t} + \bar{U}_j \frac{\partial \bar{U}_i}{\partial x_j} = -\frac{1}{\rho} \frac{\partial \bar{p}}{\partial x_i} - \frac{\partial \tau_{ij}^a}{\partial x_j} + \nu \frac{\partial^2 \bar{U}_i}{\partial x_j \partial x_j} \quad (2.40)$$

where  $\tau_{ij}^a = \tau_{ij}^R - \frac{1}{3}\tau_{ij}^R\delta_{ij}$  is the anisotropic residual-stress tensor and  $\bar{p} = \bar{p} + \frac{1}{3}\tau_{ij}\delta_{ij}$  the modified filtered pressure. Also in this case we are dealing with an unclosed equation, which therefore needs an additional term to be 'closed'. This is achieved by modelling the residual stress tensor  $\tau_{ij}^a$ . All these fields ( $\bar{\mathbf{U}}(\mathbf{x}, t), \bar{p}(\mathbf{x}, t), \tau_{ij}^a(\mathbf{x}, t)$ ) are random, three-dimensional and unsteady, even if the flow is statistically stationary or homogeneous [6]. They also depend, more or less explicitly, on the type of filter and its size. It has just been mentioned how this new set of equations necessarily requires the addition of a term, the residual stress tensor, for closure. The simplest and probably also the most popular method is the model proposed by Smagorinsky.

### The Smagorinsky model

This model is usually described by two distinct sections. First, a proportionality relationship is defined between the anisotropic residual stress tensor and the filtered rate of strain:

$$\tau_{ij}^a = -2\nu_r\bar{S}_{ij}. \quad (2.41)$$

The link between these two tensors occurs through the coefficient  $\nu_r$ , which represents the eddy viscosity of the residual motions. The central problem in LES is the construction of subgrid models, which amounts to an appropriate choice of expression for  $\nu_r$  (if an eddy viscosity model is used). In analogy to the mixing length hypothesis, for high Reynolds number, the eddy viscosity can be modelled as

$$\nu_r = l_S^2\bar{S} = (C_S\Delta)^2\bar{S}, \quad (2.42)$$

where  $\bar{S} = (2\bar{S}_{ij}\bar{S}_{ij})^{\frac{1}{2}}$  is the characteristic rate of strain and  $l_S$ , taken proportional to the filter width  $\Delta$  through the Smagorinsky coefficient  $C_S$ , is the Smagorinsky lengthscale. With a specification of the Smagorinsky lengthscale  $l_S$ , the LES equations can be solved without the explicit specification of the filter.

The numerical solution of LES equations involves discretization in space and time, consequently the choice of numerical solution scheme assumes great importance. Although Smagorinsky's model is a good solution for successfully solving the system of LES equations in the case of many different types of flow, it also has some weaknesses. Specifically, the greatest difficulty concerns, once again, the modelling of near-wall effects: in fact, the small-scale anisotropy in this region cannot be taken into account by the model. In this respect, it is necessary to introduce damping functions or make changes to the  $C_S$  coefficient, so that it can dynamically adjust to local changes in the flow structure.



## Chapter 3

# Physical problem

In this third chapter, we will present the geometric and physical setup of the simulation and thus of the autoclave domain. Specifically, we will carry out what can be described as a general overview of the actual construction of the model and operating conditions.

### 3.1 Simulations set-up

The basic concept of this work was to reproduce an extremely simplified model of an autoclave. As has been repeatedly stated in the previous chapters, the main focus was on the study of the turbulence created inside the pressurising chamber of the machine and its strongly anisotropic and non-homogeneous characteristics. With regard to this, the geometric construction of the model is characterised by an annular inlet for the air flow (see figure 3.1), as is often the case in real autoclaves.

In order to replicate the typical flow pattern in an autoclave (well described in the section 1.3.2 of the introductory chapter), the function of a 'half dome' was implemented manually in order to reconstruct the collision of the upper and lower flows, which are then deflected towards the rear of the machinery. As far as the actual creation of the simulation domain inlet is concerned, what was done in Pluto (CFD programme used, which will be discussed in much more detail in the next chapter, 4) was to 'manipulate' the cells concerned with a precise velocity characteristic: specifically, this is an air flow with an inlet velocity only characterised by the  $V_x$  component and with a modulus equal to 5  $m/s$ , as shown in figure 3.2.

A similar approach was also maintained for the creation of the dome mentioned earlier; in this case too, the script manipulated the 'nature' of the cells, this time to impose them as real walls where the flow would collide, giving rise to that recirculation and deflection phenomenon typical of the autoclave structure, which in some form alludes to the shape of a dome and which is shown in figures 3.3

In these figures, what is the basic idea is thus well represented: recreating the flow path that is 'guided' by the shape of this dome, which is the closing door of the autoclave. In the first, the 3.3a and 3.3b, the contour of the velocity component  $V_x$  is depicted and thus a 3D representation of the anterior shape of the domain. The 3.3c, on the other

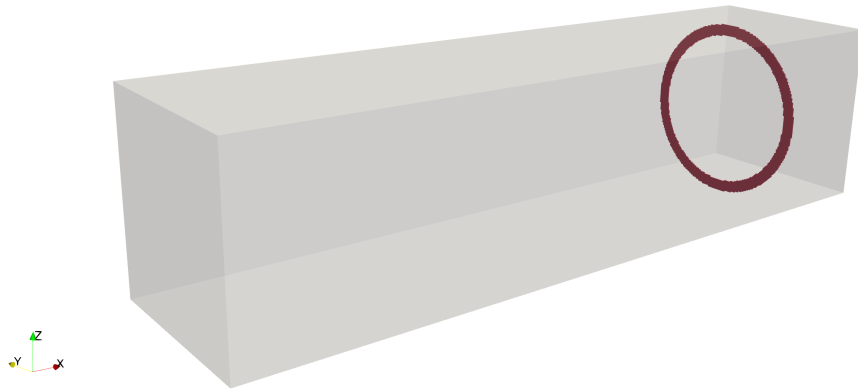


Figure 3.1: Injection ring. It's an annular inlet for the air flow, as is often the case in real autoclaves. The flow enters the chamber in the positive x-axis direction and develops.

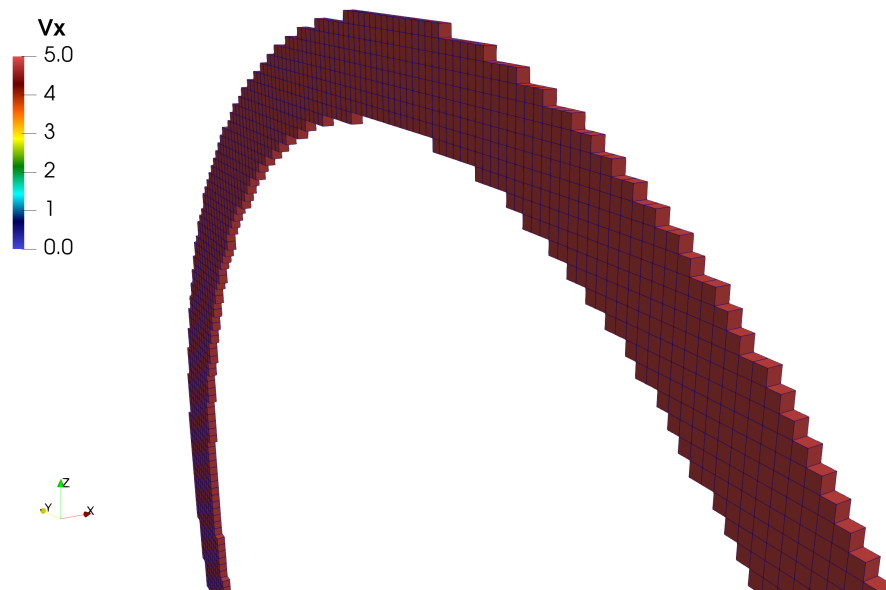


Figure 3.2: The figure shows us what is a zoom on the geometric construction of the injection ring of the presented autoclave model. The thickness, as can be clearly seen, is that of a single mesh cell.

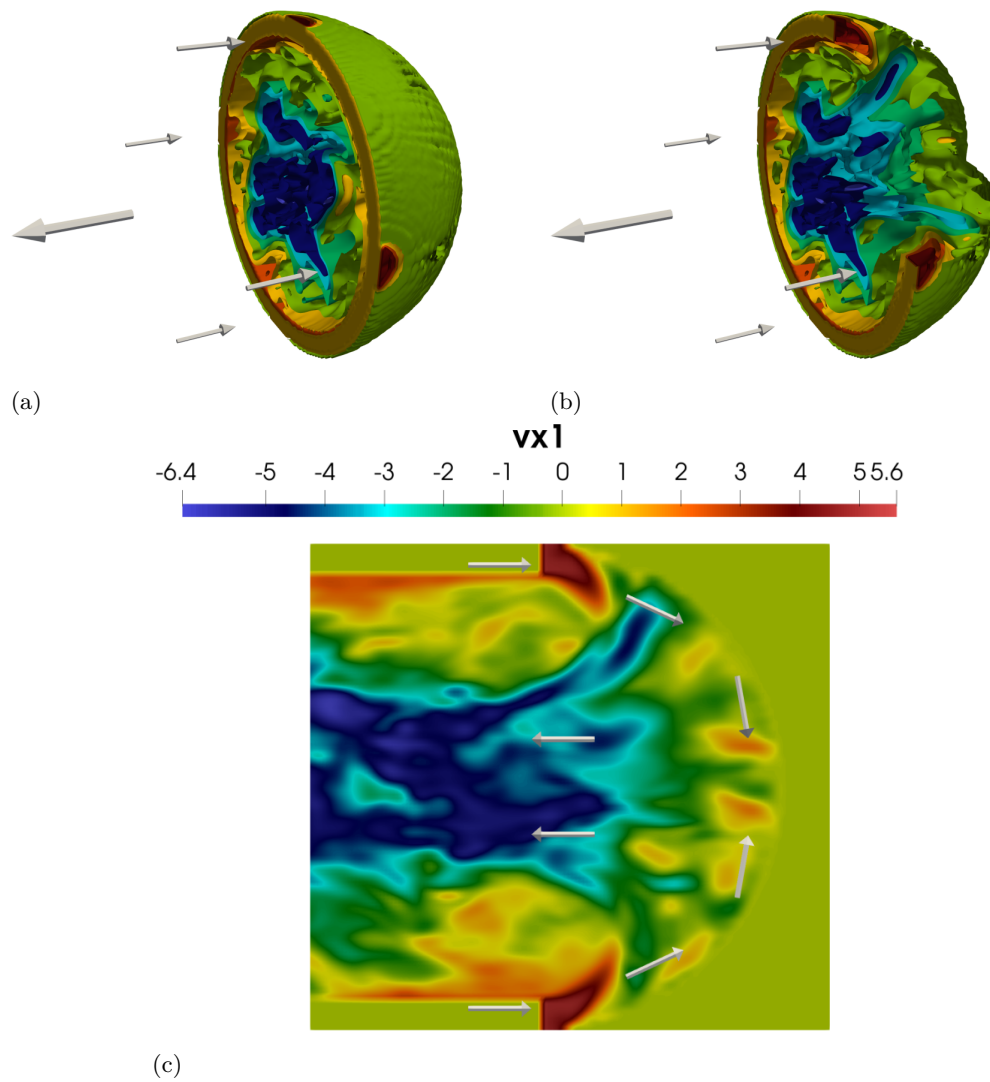


Figure 3.3: (3.3a and 3.3b) Contour of the x-component of velocity. (3.3c) Cross-sectional plane of the autoclave at  $y=0$ . Arrows have been manually added to the images to indicate what is the path that the flow is forced to follow before it can develop freely in the chamber.

hand, gives us a two-dimensional perspective of the path taken by the air flow, and the separation between the motion field cells and those set as walls is highlighted. In both of these, grey arrows appear to indicate even more clearly the inlet ring and the deflection of the flow, which, moving backwards from the positive axis of the autoclave, takes on a negative modulus value. In order to create this axial airflow inlet, it was necessary to define two radii,  $r_0$  and  $r_v$ , which could delimit the thickness in the y-z plane 'of the ring'. The first represents the lower extreme and consequently also the 'ceiling' of the machine. In fact, the geometry of the autoclave is restricted, always maintaining a constant cross-section, moving from the point of entry of the flow, positioned at abscissa  $x_0$ , towards the bottom of the autoclave itself. The second radius,  $r_v$ , identifies the upper boundary of the injection ring and again the 'ceiling' of the autoclave which, from  $x_0$  towards the autoclave inlet door (what has been referred to several times in this chapter as the 'dome') widens.

### 3.1.1 Notes on simulations with Openfoam

The geometric preparation of the autoclave model is the step that probably created the most difficulties. The fluid-dynamic simulation programme used by its very nature did not allow the creation of 'over-complicated' geometries but merely provided the tools for setting up domains such as cylinders, parallelepipeds, spheres, etc. An attempt was therefore made to reproduce a geometry reminiscent of that of an autoclave, possibly by means of a step structure, as is done in Openfoam, by means of a 'snapping' operation.

To overcome this problem, it was decided to act not so much from a purely geometric point of view, but rather in terms of the physical nature of the cells constituting the mesh. This has already been discussed in the chapter on the construction of the inlet ring; the same has therefore been done for this clipping operation, which at this point is to be considered as a fictitious operation.

The starting point was a parallelepiped of spanometric dimensions: 6.0 x 0.75 x 0.75 (x-y-z). From this notion, the figure 3.6 depicts this important operation even better.

### 3.1.2 Operating conditions and Viscosity modelling

The air flow studied is incompressible and viscous. The evolution of the density during the simulation is almost non-existent, in the sense that this physical quantity remains practically constant throughout. This condition is also evidenced by the time-line of the Mach number, which shows us a value that starts at about 0.006 to increase as the flow evolves and reach values of about 0.02, which identifies a subsonic flow, clearly, and incompressible. In these types of flows, density is independent of pressure, and pressure influences only the velocities, through the momentum equations. As far as viscosity is concerned, however a modelling of the quantity in question is necessary; the use of Sutherland's law<sup>1</sup> was chosen. It specifies the viscosity of the fluid in a selected

---

<sup>1</sup> $\mu = \frac{C_1 \cdot T^{\frac{3}{2}}}{T + C_2}$ , where  $C_1 = 1.458e - 6 \left[ \frac{kg}{m^2 s k^{\frac{1}{2}}} \right]$  and  $C_2 = 110.4[K]$  are two empirical constants; while T is the temperature in Kelvin [K].

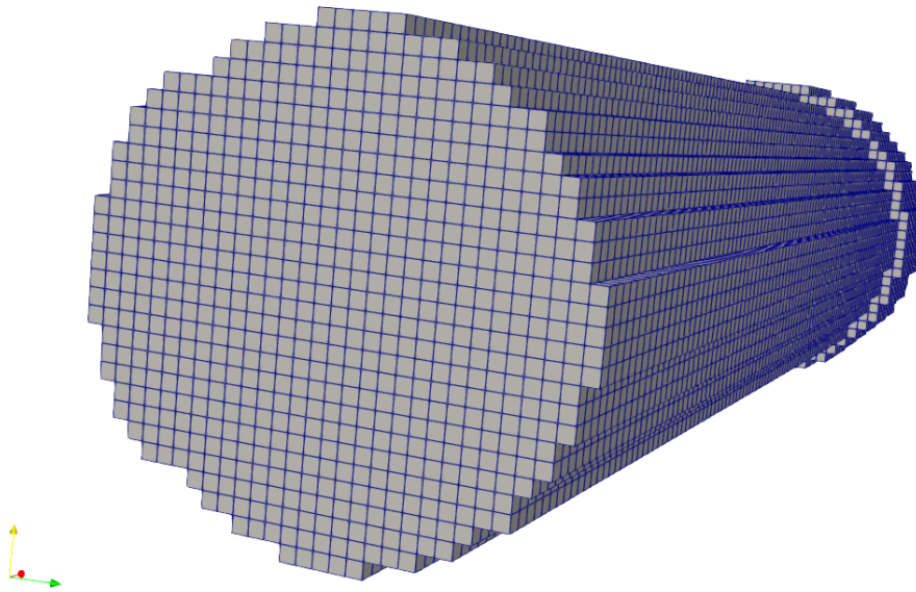


Figure 3.4: The one presented in this image is the geometry of the autoclave made using the techniques available in Openfoam that allow the desired shape to be cut out directly from the source domain.

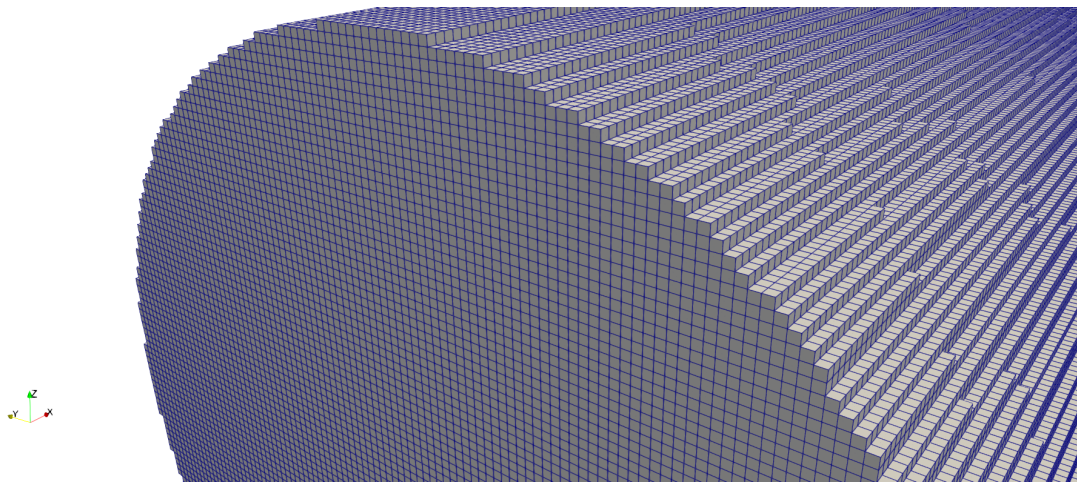


Figure 3.5: The figure shows the successful dummy cut operation of the geometry in PLUTO. Despite the difficulties encountered, it can be seen that the result is very similar to that obtained in Openfoam (3.4).

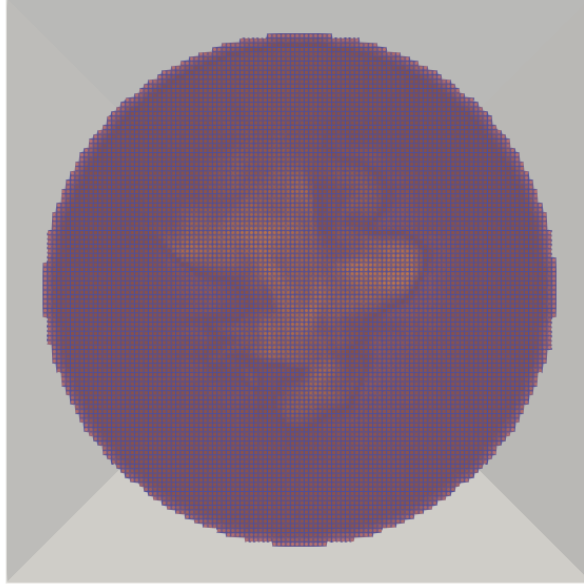


Figure 3.6: Difference between geometric box and autoclave. From the initial parallelepiped, the representative step shape of the autoclave was derived.

volume in terms of dynamic viscosity ( $Pa \cdot s$ ). It should be specified that in this case the modelling is done for only one of the two viscosity terms that appear within the viscous stress tensor<sup>2</sup>, the shear one ( $\nu_1$ ); the other (bulk coefficient,  $\nu_2$ ) is set equal to zero as specified by molecular theory for monoatomic gases. It is well known from the theory in the literature, and even more so from observing the modelling law just described, that viscosity is therefore a function of temperature (as well as pressure) and strongly depends on it, and in gases, as in our case, as temperature increases, viscosity also increases. Regarding the physical quantity of temperature, it has previously been 'processed': since PLUTO is an astrophysical code, when using it, as in this case, for low Mach airflows, it is necessary to dwell on the question of units of measurement. What has been done is to calculate the temperature value during the simulation through the ideal gas law<sup>3</sup> and then normalise it by multiplying it by the square of the **unit-velocity** (which will be taken up in the programme description in Chapter 4).

With regard to the initial conditions, the values chosen, which are congruent with what are usually the operating conditions of industrial autoclaves during a normal curing process, are as follows:

$$> \rho = 1.225 \left[ \frac{kg}{m^3} \right], \text{ i.e. the ambient air value}$$

---

2

$$\Pi = \nu_1 [\nabla \mathbf{v} + (\nabla \mathbf{v})^T] + \left( \nu_2 - \frac{2}{3} \nu_1 \right) (\nabla \cdot \mathbf{v}) \mathbf{I} \quad (3.1)$$

---

<sup>3</sup> $T = \frac{p}{\rho R}$ , where  $R = 287.3 \left[ \frac{J}{kg \cdot K} \right]$  is the universal gas constant.

- >  $p = 101\,325\text{[Pa]}$ , it too, like the density before, is the typical ambient value of air.
- >  $v = 5\left[\frac{\text{m}}{\text{s}}\right]$ . This value is typical for many autoclaves, taking into account the inevitable losses that the flow undergoes within the recirculation channels.

These variables are initialised and normalised. The normalisation, once again, must be carried out to ensure that the units of measurement considered by the simulation are the correct and desired ones for us. This is done by dividing the quantities each by the corresponding units of reference; thus, writing this as code, we will have that:

```
v[RHO] = g_inputParam[RHO_AMB];
v[RHO] /= UNIT_DENSITY;

v[PRS] = g_inputParam[P_AMB];
v[PRS] /= UNIT_DENSITY*UNIT_VELOCITY*UNIT_VELOCITY;

d->Vc[VX1][k][j][i] = g_inputParam[VEL]/UNIT_VELOCITY;
```

The simplifications of the autoclave model also affect the definition of initial conditions and boundary conditions. In fact, the literature shows how most autoclaves provide for the passage of the air flow inside some ducts, inside which there are thermal resistances used for the purpose of heating the air flow before it enters the chamber. This, specifically, serves to ensure that the environment reaches a certain temperature level, which is very important for a good result during the curing treatment. In our case, the heating part by means of resistors was not simulated in any way and therefore initial conditions, typical of the external environment, were assumed for pressure and density and from these, as already mentioned, the temperature was calculated. The air flow is then assumed to be clean and undisturbed at the inlet; it moves inside the autoclave, colliding with those cells that have been transformed into real walls, and exits from the surface to the bottom of the autoclave, which is characterised by an outflow-type boundary condition.

### 3.2 Implementation of additional perturbations ('hatches')

The main focus of this work is to implement a practical solution that gives a real benefit with regard to the attempt to homogenize an anisotropic turbulent structure that habitually develops within the closed environment of an industrial autoclave, as also shown by the results (Chapter 5). An attempt in this regard was made by installing some velocity perturbations around the walls of the autoclave model. Physically, these are a number of small doors that 'open' randomly and remain in this condition for a certain amount



Figure 3.7: Hatches - start configuration. In one of the two head configurations, the hatches are placed at the top and bottom, corresponding to the axis of the autoclave.

of time, only to close and open again. This frenetic and completely random alternation is thought to be useful in an attempt to recreate an environment with a high degree of unpredictability.

### 3.2.1 C script

Initially, for simplicity's sake, it was decided to position these objects at the top and bottom in correspondence with the symmetry axis of the chamber.

However, in order to best reflect that concept of randomness which allows us to achieve a high degree of unpredictability within the simulations, it was decided to generate randomly created hatches in different positions on the external surfaces of the autoclave. In order to realise the random opening of these hatches, we first asked ourselves the question as to what relationship the individual object in question could have with the surfaces of the autoclave. A point, from a Cartesian point of view, is characterised, in a three-dimensional environment, by three coordinates  $(x,y,z)$  that represent exactly the numbers that can be randomly generated within an arbitrarily established range (and constrained in particular by the dimensions of the autoclave itself). In combination with a function, already implemented within PLUTO, which takes as input a SEED, and then generates values (in our case numbers in floating point format) randomly<sup>4</sup>, a sort of matrix structure was created containing in each row the three coordinates of the

---

<sup>4</sup>The computer never generates random numbers, but rather a deterministic sequence of uncorrelated numbers with statistical properties equivalent to those of a sequence of random numbers. Each sequence is precisely associated with a given seed, so if we have two different scripts with the same seed, then the sequence of random numbers output will be the same.

point, the centre of hatches:

```

if (first_call){
    RandomSeed(g_inputParam[SEED],0);
    first_call = 0;
}

if(g_time >= t_change){
    for(coord = 0; coord <= 9; coord++){
        coord_boc[coord][0] = RandomNumber(0.0+0.5*dx[i]+..
        ... +8.0*dx[i], x0-8.0*dx[i]-0.5*dx[i]);
        coord_boc[coord][1] = RandomNumber(-r0, r0);
        coord_boc[coord][2] = RandomNumber(-r0, r0);
    }
    t_change = floor(g_time) + 1.0;
}

```

The first thing to note is the input within the 'if-statement', which occurs if and only if the 'g time', i.e. the simulation time, is greater than or equal to a certain threshold value, which is then incremented before exiting the if-statement. This means that it is intended to scan the opening of new hatches after a specific time period set by the user (in this case it is set to one second). This threshold variable, called *t\_change*, has, from a purely computer language point of view, been defined as a simple *double*, but as a *static\_double*<sup>5</sup>. This ensures that the random number generation function is not called several times. In this regard, the matrix variable containing the centres of the hatches is also defined as a *static\_double* because otherwise it would assume random values after the first cycle, affecting the Cartesian coordinates of the single point. Then there is the actual core of random generation, which is done as many times as the number of hatches to be 'opened'. At this point for the creation of the three co-ordinates, it is necessary to take into account the dimensions of the chamber (as mentioned earlier) in the three directions x, y and z. All of this clearly allows us to set stakes and thus circumscribe what is the random generation of numbers, thus carrying out an initial "skimming". At this stage, in which the centres of the hatches will simply be generated in terms of Cartesian terms, it is also necessary to establish which values are actually acceptable, in terms of the results to be achieved, and which are to be discarded. This discussion mostly refers to y- and z-coordinates: it is indeed true that the autoclave extends, symmetrically,

---

<sup>5</sup>A static variable is a type of variable that retains its value from call to call, i.e. it is initialised only once; for example, if the initialisation made is worth 1, then from the second call onwards it will retain the value it took at the end of the current call.

from  $-r_0$  to  $r_0$ , but to ensure that the point in question is always positioned on the autoclave wall and not inside it, not all combinations of numbers are acceptable; in particular, the radius that is constructed using the y and z co-ordinates of the point ( $r = \sqrt{y[j] \cdot y[j] + z[k] \cdot z[k]}$ ) must be equal, barring an error, to the extreme value  $r_0$ , which indicates the limiting dimension of the autoclave. A further constraint that is intended to be respected is the one that allows us to construct hatches that are not too close to each other, but on the contrary are equally spaced. This creates a set of **adapted** co-ordinates that can be used for the actual geometric construction of the hatches. The next step was to 'flag' the cells intended to geometrically represent the surface of the hatches and thus the input of a velocity perturbation. In this regard, it is very important to bear in mind the external shape of the autoclave (already described at length within the chapter). We scan, one at a time, all the "mouths" that we intend to open by means of a for loop; the condition that allows us to perfectly integrate the mouths with the "stepped" geometry is:  $|r - r_0| < 0.5 \cdot dx[i]$ , this means that the cells chosen must be those on the side perimeter of the autoclave; the actual size is instead provided by these other 3 conditions:  $|x[i] - coord_{boc}[coord][0]| < 8.0 \cdot dx[i]$ ,  $|y[j] - coord_{boc}[coord][1]| < 8.0 \cdot dx[i]$  and  $|z[k] - coord_{boc}[coord][2]| < 8.0 \cdot dx[i]$ <sup>6</sup>; they act on the extent of the object by selecting the cells to be opened starting from its centre and continuing to the right and left in a perfectly symmetrical manner.

---

<sup>6</sup>In order to understand the writing of the code, some clarification is needed:

1. the inequality condition  $8.0 \cdot dx[i]$  identifies the geometric extension of the hatches (in the various directions).
2. objects defined as  $coord_{boc}[...][...]$  are matrix structures in which the Cartesian triads of points are stored, each coordinate of a single triad per column.

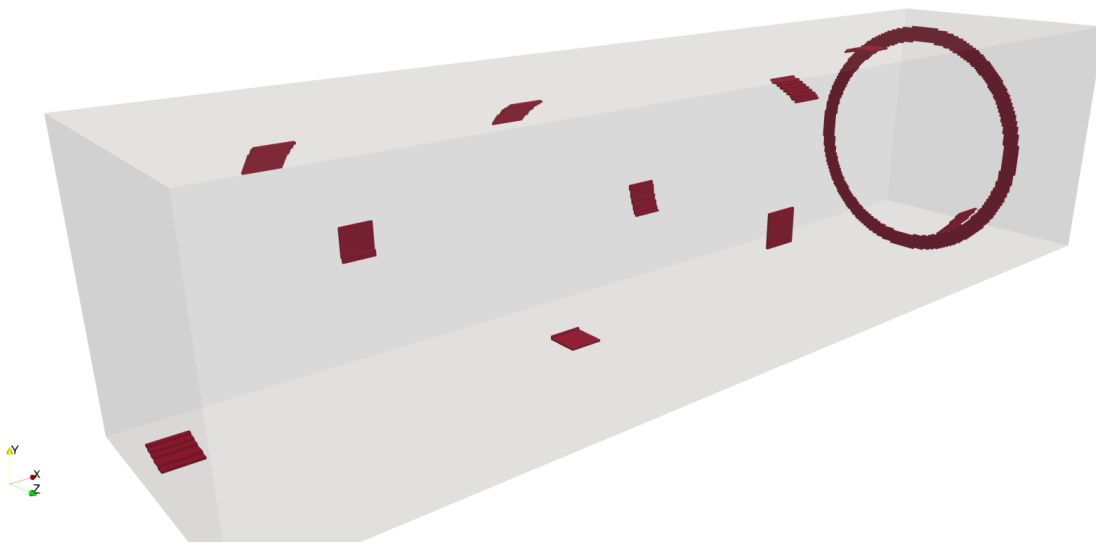


Figure 3.8: Hatches arrangement. Such a solution is the one that will prove most promising and involves totally random placement of the hatches around the side surface of the autoclave.

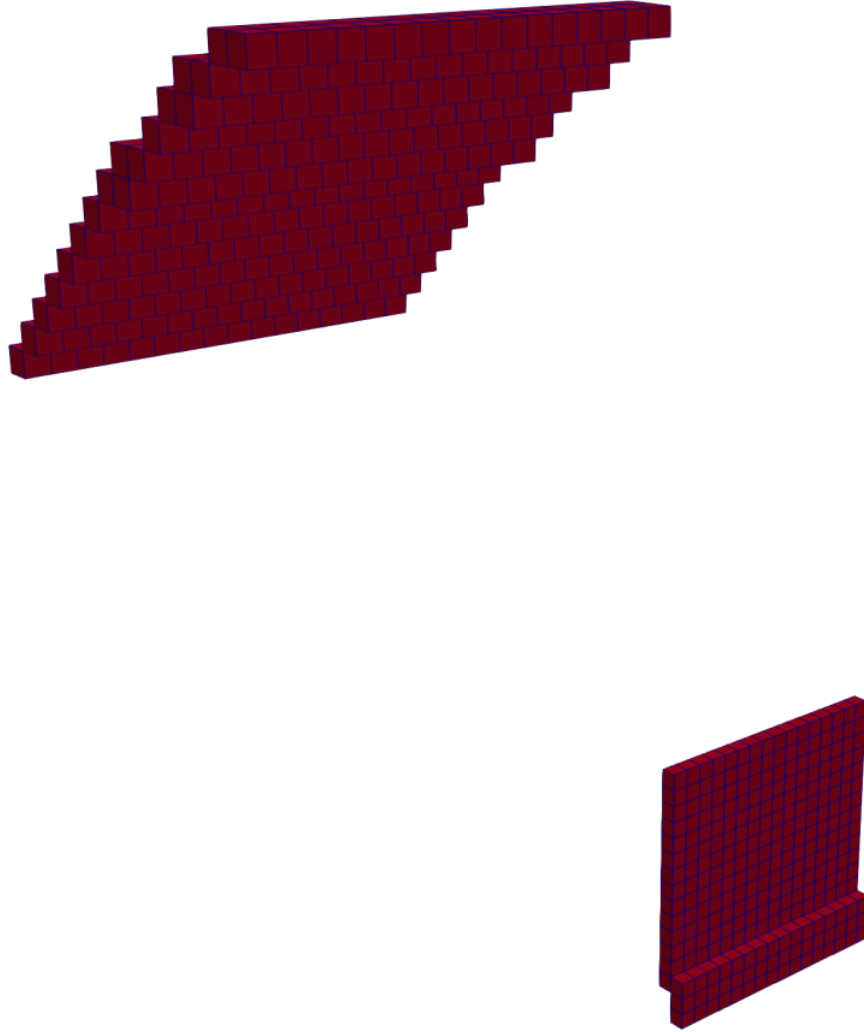


Figure 3.9: The image depicts the structure of the hatches in detail. It can be understood, from this figure, how their geometry is such that they fit perfectly with the course of the autoclave surface.

## Chapter 4

# Numerical methods

Up to this point, moving within the first chapters, one has been able to familiarise oneself with what is the characteristic environment of an autoclave, as well as with the physical modelling carried out in favour of computational simulations. At this point, therefore, it is necessary to describe the numerical/mathematical apparatus underlying the entire simulation framework. Indeed, along with the analytical basis, made up of equations, algebraic models and various assumptions, the numerical system that makes sense of the entire physical system is equally important. The use of this fluid-dynamic simulation code, in spite of some difficulties encountered with regard to a correct adaptation to the physical problem to be studied<sup>1</sup>, has guaranteed us the use of spatial resolution methods that are decidedly higher than usual; if, in fact, one usually has an approach based on RANS, in this case the resolution strategy is direct (DNS) and concerns the analysis of the impact of the vortical structures. A peculiarity of the programme is also, as we shall see, that of using explicit integration methodologies, without resorting to iterative processes.

### 4.1 Initial description of software: PLUTO code v4.4.2

PLUTO [10] is a finite-volume/finite-difference code designed to integrate a system of conservation laws

$$\frac{\partial \mathbf{U}}{\partial t} = -\nabla \cdot \mathbf{T}(\mathbf{U}) + \mathbf{S}(\mathbf{U}), \quad (4.1)$$

where  $\mathbf{U}$  denotes a state vector of conservative quantities,  $\mathbf{T}(\mathbf{U})$  is a rank 2 tensor, the rows of which are the fluxes of each component of  $\mathbf{U}$ , and  $\mathbf{S}(\mathbf{U})$  defines the source terms.

The code, like the vast majority of numerical codes, provides a common discretization recipe, involving three general steps: a piecewise polynomial reconstruction followed by the solution of Riemann problems at zone interfaces and a final evolution step. This

---

<sup>1</sup>The code provides a multiphysics, multialgorithm modular environment particularly oriented toward the treatment of astrophysical flows in presence of discontinuities [10].

succession of steps allows us to thoroughly analyse the numerical methods used. PLUTO adopts a structured mesh approach for the solution of the system of conservation laws (4.1). The grid, within which the evolution of the flow is described, can be static (entirely written in the C programming language), as in our case, or, through the implementation of an additional library (Chombo library), there is the possibility of also describing the calculation domain through adaptive mesh refinement (AMR), written in C++ and Fortran. All these structured calculation grids are enclosed by a boundary and augmented with guard cells or ghost points to implement boundary conditions on a given calculation stencil [10]. When starting a simulation with Pluto for the first time, what one needs to do is to outline a kind of setup of the problem being analysed. This procedure, activated by launching a Python script, results in the creation of a header file in which the backbone of this setup is stored. Within this chapter, what we are going to do is precisely to describe this setup from start to finish, dwelling on the more or less in-depth and detailed description of the numerical methods used.

## 4.2 The Hydrodynamics (HD) Module

Depending on the type of physical problem one is dealing with, and thus depending on the flow equation that must be solved for a complete description of the field of motion, the software provides different hydrodynamic modules and algorithms. In the case of the study of an incompressible, viscous flow inside an industrial autoclave, the most suitable choice is the HD module, which uses the Euler equations to describe classical fluid dynamics. With the HD module, PLUTO evolves in time following system of conservation laws:

$$\frac{\partial}{\partial t} \begin{pmatrix} \rho \\ \mathbf{m} \\ E_t + \rho\Phi \end{pmatrix} + \nabla \cdot \begin{pmatrix} \rho\mathbf{v} \\ \mathbf{m}\mathbf{v} + p\mathbf{I} \\ (E_t + p + \rho\Phi)\mathbf{v} \end{pmatrix}^T = \begin{pmatrix} 0 \\ -\rho\nabla\Phi + \rho\mathbf{g} \\ \mathbf{m} \cdot \mathbf{g} \end{pmatrix} \quad (4.2)$$

where  $\rho$  is the mass density,  $\mathbf{m} = \rho\mathbf{v}$  is the momentum density,  $\mathbf{v}$  is the velocity,  $p$  is the thermal pressure and  $E_t$  is the total energy density:

$$E_t = \rho e + \frac{\mathbf{m}^2}{2\rho} \quad (4.3)$$

An equation of state provides the closure  $\rho e = \rho e(p, \rho)$ . Finally, to complete the description of the variables,  $\Phi$  is gravitational potential and  $\mathbf{g}$  the acceleration vector. The conservative variables  $\mathbf{U}$  and the flux tensor are

$$\mathbf{U} = \begin{pmatrix} \rho \\ \mathbf{m} \\ E_t + \rho\Phi \end{pmatrix}, \mathbf{T}(\mathbf{U}) = \begin{pmatrix} \rho\mathbf{v} \\ \mathbf{m}\mathbf{v} + p\mathbf{I} \\ (E_t + p + \rho\Phi)\mathbf{v} \end{pmatrix}^T. \quad (4.4)$$

The set of primitive variables  $V \equiv (\rho, \mathbf{v}, p)^T$  is given by density, velocity and thermal pressure  $p$ . Primitive variables are generally more convenient and preferred when

assigning initial/boundary conditions and in the interpolation algorithms [10].

### 4.3 Finite Volume Method

When studying any physical problem, irrespective of the context in which one finds oneself, from an engineering point of view, computational modelling (as well as, of course, the entire experimental set-up) proves fundamental. Among the various steps that make up the modelling of the phenomenon studied, there is the need to structure an appropriate mathematical model, which together with the choice of appropriate initial and boundary conditions, allows us to proceed to the solution of the problem. To be considered reliable and valid, this model must possess specific properties of stability, accuracy and consistency, which can certainly make a difference in obtaining realistic solutions to the physical problem studied. The most classic and well-known of these are the finite volume method, the finite element method and the finite difference method. These just mentioned are all approximations of a system of partial differential equations (PDEs), since, as is understandable, one is almost never able to obtain the exact solution of the equations that characterise the problem being studied. The equations one intends to model derive from the physical problem one intends to analyse, and, for example, may be precisely the system of conservation equations 4.2, described above. In PLUTO, numerical integration of the conservation law 4.1 is achieved through shock-capturing schemes using the finite volume (FV) formalism where volume averages evolve in time [10]. More generally, the finite-volume method is an approach based on a conservative scheme, where the flux on the boundary of one cell equals that on the boundary of the adjacent cell [9]; this balance approach means that the numerical flows are locally conservative [5]. Reference is made to the integral form of the conservation equations and the integration itself is done by taking a control volume as a reference. The model equation in integral form, for steady state, is:

$$\int_S \rho \phi \mathbf{v} \cdot \mathbf{n} dS - \int_S \Gamma \nabla \phi \cdot \mathbf{n} dS \equiv \int_V q_\phi dV \quad (4.5)$$

Finite volumes are therefore a class of discretisation schemes very often used in the approximation of the solution of these systems of conservation equations. These methods are characterised by great numerical robustness [8]. This discretization procedure is distinctive and involves two basic steps. In the first step, the partial differential equations are integrated and transformed into balance equations over an element. The result is a set of semi-discretized equations. In the second step, the approximation profiles of the variables within the individual cells are chosen and consequently the surface values of the variables are related to their cell values [22]. In this way, it is possible to transform the algebraic relationships into true algebraic equations. Typically, the physical domain is discretized in finite volumes (cells) that only intersect at their edges, and a computational node is assigned to the center of each cell (cell center schemes)<sup>2</sup>. The boundary conditions are instead assigned to the boundary surface of the computational domain.

---

<sup>2</sup>Another approach assigns the computational cells at the nodes (cell vertex schemes).

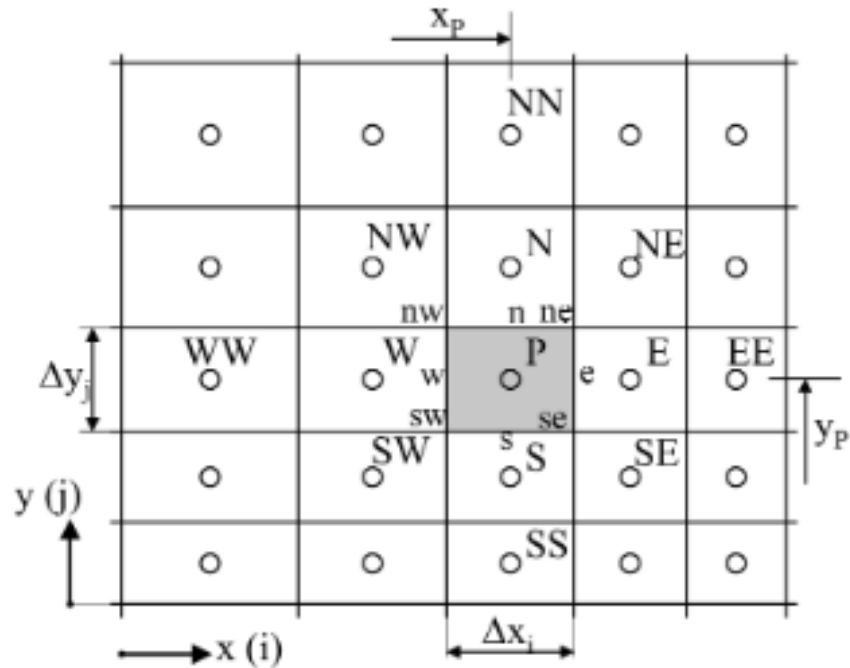


Figure 4.1: Two-dimensional Cartesian grid for finite volumes

With the finite volume method, discontinuities of the coefficients will not be any problem if the mesh is chosen such that the discontinuities of the coefficients occur on the boundaries of the control volumes. Thus, the finite volume scheme differs from the finite difference scheme in that the finite difference approximation is used for the flux rather than for the operator itself [5]. Although the finite-volume schemes currently in PLUTO guarantee at most second-order accuracy (as opposed to the third or fifth typical of finite-difference methods), they have been preferred because they are less costly in terms of CPU and hence computation time. Furthermore, it will be seen that with the implementation of WENO methods it is possible to increase the spatial resolution order by so much. Indeed, by changing the slope of the linear reconstruction in the cells, non-oscillatory resolution of discontinuities can be achieved. ENO methods have begun to be developed in this regard.

#### 4.4 Reconstruction: WENOZ Schemes

Reconstruction methods have to satisfy monotonicity constraints in order to avoid spurious oscillations in proximity of discontinuities and steep gradients [10]. One of the most popular spatial reconstruction methods concerned with mitigating the problem of oscillation in the value of the interpolated solution are WENO schemes. These refer to a class of weighted essentially non-oscillatory schemes and are the natural and improved

evolution of ENO schemes (essentially non-oscillatory), where a weighted average is taken from all the stencil candidates. The WENO schemes are very robust and they are frequently employed for solving hyperbolic conservation laws in finite volume and finite difference form. The reconstruction schemes that are implemented for the two forms of discretization differ substantially: in the finite difference WENO scheme the reconstruction is based on node values, while finite volume WENO schemes use cell averages for the interpolation. In the finite volume formulation, cell averages,  $\bar{\phi}_i$ , are used to obtain point values at the right and left faces,  $\bar{\phi}_{i+\frac{1}{2}}^\pm$  [19]. The main idea of the WENO schemes is to form a weighted combination of several local reconstructions based on different stencils (usually referred to as small stencils) and use it as the final WENO reconstruction [24]. In the case studied in this thesis, in particular, the fifth-order WENOZ method was used: it is less dissipative and provide better resolution at critical points at a very modest additional computational cost. The classical fifth-order WENO scheme uses a 5-points stencil which is subdivided into three 3-points stencils. The innovative idea, compared to the basic WENO method, is to use the entire 5-point stencil to devise a new smoothness indicator of a higher order than the classic smoothness indicators [12]. By doing so, it is possible to obtain a less dissipative scheme, with a lower computational cost, but still maintaining the non-oscillatory characteristic of the interpolated solution. If we write the integral form of a general one-dimensional hyperbolic conservation law<sup>3</sup> approximated by the finite volume method in the following way:

$$\frac{d\bar{u}_i(t)}{dt} + \frac{1}{\Delta x_i} (f(u_{i+\frac{1}{2}}) - f(u_{i-\frac{1}{2}})) = 0, \quad (4.7)$$

where  $\bar{u}_i = \frac{1}{\Delta x_i} \int_{I_i} u(x, t) dx$ , then for a fifth order WENO scheme, the approximation  $u_{i+\frac{1}{2}}^-$  uses cell average values in cells  $I_{i-2}, I_{i-1}, I_i, I_{i+1}, I_{i+2}$  while the approximation  $u_{i+\frac{1}{2}}^+$  use those in cells  $I_{i-1}, I_i, I_{i+1}, I_{i+2}, I_{i+3}$ . With a monotone numerical flux and WENO reconstructions, the integral form 4.7 can be written as

$$\frac{d\bar{u}_i(t)}{dt} + \frac{1}{\Delta x_i} (\hat{f}(u_{i+\frac{1}{2}}^-, u_{i+\frac{1}{2}}^+) - \hat{f}(u_{i-\frac{1}{2}}^-, u_{i-\frac{1}{2}}^+)) = 0 \quad (4.8)$$

Here,  $u_{i+\frac{1}{2}}^-, u_{i+\frac{1}{2}}^+$  (and alos,  $u_{i-\frac{1}{2}}^-, u_{i-\frac{1}{2}}^+$ ) are approximations based on cell average values in stencils one cell biased to the left and one cell biased to the right, respectively. The function  $\hat{f}$  is a monotone numerical flux which works, for example in the case of Godunov-like fluxes, works as follows:

$$\hat{f}(a, b) = \begin{cases} \min_{a \leq x \leq b} f(u) & \text{if } a \leq b \\ \max_{b \leq x \leq a} f(u) & \text{if } a > b \end{cases} \quad (4.9)$$

---

3

$$u_t + f(u)_x = 0 \quad (4.6)$$

<b>RK3</b>
$\mathbf{U}^* = \mathbf{U}^n + \Delta t^n \mathcal{L}$
$\mathbf{U}^{**} = \frac{1}{4}(3\mathbf{U}^n + \mathbf{U}^* + \Delta t^n \mathcal{L})$
$\mathbf{U}^{n+1} = \frac{1}{3}(\mathbf{U}^n + 2\mathbf{U}^{**} + 2\Delta t^n \mathcal{L})$

Table 4.1: Solution to the next time level: where  $\Delta t^n = t^{n+1} - t^n$  is the time increment between two consecutive steps and  $\mathcal{L}$  denotes the discretized spatial operator on the right hand side of Eq.(4.1) [10].

## 4.5 Time stepping: Runge-Kutta (RK3)

After discussing the spatial reconstruction methods, we analyze the algorithms used within the code for temporal discretization. The method that was chosen for the simulations performed within this paper is TVD (total variation diminishing) Runge-Kutta, a family of explicit and implicit temporal integration schemes.

The setup described, i.e. a spatial reconstruction using the WENOZ method and a time\_stepping using explicit multi-step algorithms (such as RK3, three-stage), is found to have better stability properties for interpolations above the second order. In this regard, it is also important to evaluate the Courant number, which in the specific case of our simulation system was set to a value of 0.25. It represents an important quantity in the study of numerical stability. In fact, the numerical solution is asymptotically stable (i.e. the numerical cell averages all remain bounded as the number of time steps increases) if and only if the CFL (Courant, Friedrichs and Lewy) condition in the table 4.2, relating to the Runge-Kutta time reconstruction scheme used, is verified. This condition, which is precisely an inequality condition, guarantees that the exact solution at the next time instant  $t_{n+1}$  in a single  $i$ -th cell depends on the values at the previous time instant  $t_n$  of cells  $i$ ,  $i+1$  and  $i-1$ , i.e. that same cell and the two adjacent cells.

### 4.5.1 Time Step Determination

The time step  $\Delta t^n$  is computed using the information available from the previous integration step and it can be controlled by the Courant-Friedrichs-Lewy (CFL) number  $Ca$  within the limits suggested in 4.2, and as described in the previous paragraph. If  $\Delta l$  is the cell physical length, the time step roughly scales as  $\sim \Delta l$  for hyperbolic problems and as  $\sim \Delta l^2$  when parabolic terms are included via a standard explicit scheme. Instead for what it regards the initial  $\Delta t$  it has been chosen in full autonomy a value that typical of the simulations and that is evidenced to be good from the point of view of the stability of the simulation. In our case, a value of the order of  $10^{-6}$  was taken as the initial  $\Delta t$ .

<i>Scheme</i>	<i>CFL Limit</i>
<i>RK</i>	$\frac{\Delta t^n}{N_{dim}} [\max_{ijk} (\sum_d \frac{ \lambda_d }{\Delta l_d}) + \max_{ijk} (\sum_d \frac{2\tau_d}{\Delta l_d^2})] = C_a \leq \frac{1}{N_{dim}}$

Table 4.2: CFL condition [10].

## 4.6 Numerical Integration of Diffusion Terms

With the explicit time integration typical of this calculation code, parabolic contributions are added to the upwind hyperbolic fluxes at the same time in an unsplit fashion [10]:

$$\mathbf{F} \rightarrow \mathbf{F}_{\text{hyp}} + \mathbf{F}_{\text{par}}$$

where "hyp" and "par" are, respectively, the hyperbolic and parabolic fluxes.

## 4.7 Riemann solver: Roe

The evolution step requires the solution of non-linear Riemann problems at each cell interface; also in the case of PLUTO-code what is done is to calculate the fluxes by solving the Riemann problem. A Riemann problem is a specific initial value problem composed of a conservation equation together with piecewise constant initial data which has a single discontinuity in the domain of interest. Solving a Riemann problem therefore means to follow in time the evolution of an initial discontinuity. It is natural that, as is very often the case in these areas, it is difficult to obtain the exact solution of the system of equations studied. It is therefore immediate to switch to an approximate resolution; the same thing also happens with the resolution of the Riemann problem, especially, as in our case, the resolution of a general state equation (EOS). Solvers, i.e. approximate resolution methods, are then introduced. In the specific case subject to analysis, in this thesis work, the solver used is **Roe**: it is a linearized Riemann solver based on Godunov schemes that consists in finding a matrix (Roe matrix) assumed constant between two contiguous cells. The Roe solver computes the numerical fluxes according to

$$\mathbf{F} = \frac{1}{2} [\mathbf{f}_L + \mathbf{f}_R - \sum_k |\lambda_k| \mathbf{L}_k \cdot (\mathbf{U}_L - \mathbf{U}_R) \mathbf{R}_k] \quad (4.10)$$

remembering that  $\mathbf{F}$  is the numerical flux functions. For the case studied, and in combination with the rest of the numerical methods, this solver was considered the best in terms of robustness and lower numerical dissipation. Inside the log file (one of the output files of the code) are printed, among other things, the number of Mach and the maximum number of iterations required by the Riemann solver during the current step. The maximum Mach number is a very sensitive function of the numerical method it may be used as a "robustness" indicator. Very large Mach numbers or rapid variations usually indicate problems and/or fixes during the computation [10].



## Chapter 5

# Numerical simulations and results

Simulations with the different setups prepared during the thesis period were carried out using the HPC cluster system of the Politecnico di Torino [40]. This is an Academic Computing project managed by LABINF (Laboratory of Advanced Informatics) under the supervision of DAUIN (Department of Automation and Informatics). Specifically, the various 'runs' were all performed using the cluster named 'Legion' and in particular the 'global' partition. This is a cluster based on the SLURM scheduler with the specifications described in detail in the following table:

<b>Architecture</b>	Cluster Linux Infiniband-EDR MIMD Distributed Shared-Memory
<b>Interconnection of nodes</b>	Infiniband EDR 100 Gb/s
<b>Service network</b>	Ethernet 1 Gb/s
<b>CPU model</b>	2x Intel Xeon Scalable Processors Gold 6130 2.10 GHz 16 cores
<b>GPU node</b>	24x nVidia Tesla V100 SXM2 - 32 GB - 5120 cuda cores
<b>Performance</b>	90 TFLOPS (luglio 2020)
<b>Computational cores</b>	1824
<b>Number of nodes</b>	57
<b>Total RAM memory</b>	22 TB DDR4 REGISTERED ECC
<b>OS</b>	CentOS 7.6 - OpenHPC 1.3.8.1
<b>Scheduler</b>	SLURM 18.08

Table 5.1: Technical specifications of the cluster used for the development of the thesis project. This is one of the three clusters of the HPC of the Politecnico di Torino; the *global* partition was used [40].

The problem we initially encountered was in getting the simulations to 'run' on the cluster due to the fact that the programme we were supposed to use was not installed. Therefore, in order to speed up times and avoid excessively long waiting times, we opted for the path of containerization. Specifically, we made use of the **Singularity** module through which we loaded the compressed PLUTO folder and the simulation setup, which was prepared locally from time to time. In short, the container is an environment in which one can run one's own programmes in complete isolation from the rest of the system, and above all without the need for them to be present and therefore pre-installed. Basically, it is an image file where the applications and all their dependencies, libraries and other binary files and configuration files required for execution are grouped together. All simulations prepared during the time span of this thesis were run with only one node per simulation and using 32 processors. Clearly, all these simulations were simulated in parallel; parallelization of the processors was done beforehand, when preparing the entire setup to be 'run'. The starting point for all the work done was a real 'blank sheet'. We had to interface with an open-source programme with which we were completely unfamiliar and with which to recreate a concept from scratch. In this fifth chapter, what will be done is to show the results of the simulations carried out, giving ample scope for all the necessary considerations, mostly through the careful analysis of the motion field images and spectral analysis graphs of the various physical quantities investigated. The case study was for a parallelepiped-shaped geometry that could resemble the shape of an autoclave. As it has already been mentioned in the introductory part of the thesis, obviously the structure of the autoclave has been simplified enormously, excluding from the simulated geometry all those components that were not indispensable to the purposes of the study of turbulence made inside the hermetic chamber of the industrial machinery. This aspect, which was repeatedly mentioned during the writing of the thesis, is very important to keep in mind for a better understanding of the work.

## 5.1 Scaling and simulation time

As in any self-respecting computational work, one of the first things to do, when constructing the calculation domain, as well as its modelling by mesh, is to carry out a scaling of the mesh itself in order to allow the programme executor to understand what type of grid quality to apply in order to optimise both the numerical results and, of course, the calculation times. This preliminary work is of great importance because it can save time and resources, which, as can easily be guessed, are two fundamental aspects in engineering, and more generally in the computational world. Clearly, the quality of the grid, more or less fine, influences the final result in most cases. However, there is always a compromise between a grid that is neither too coarse nor too fine, that can give very good results, but at the same time uses a number of resources appropriate to the type of project and that can deliver the results in a reasonable time and always correctly proportionate to the complexity of the simulation. This important process is called scalability or scaling. It is widely used to indicate the ability of hardware and software to provide more computing power when the amount of resources is increased.

Number of processors	Elapsed time	Speedup
1	3d:17h:54m:18s	1
4	1d:11h:32m:19s	2.53
8	0d:11h:57m:32s	7.52
16	0d:8h:55m:19s	10.01
32	0d:4h:15m:11s	21.14

Table 5.2: This is the result of the scaling performed for the simulations with two million cells. Indeed, the table shows us that the elapsed time trend is roughly linear as the number of processors used increases.

Especially in the case of HPC clusters, this capability is very important. Specifically for software, which is the issue of most interest, scaling is sometimes referred to as parallelization efficiency, i.e. the ratio between the actual speed and the ideal speed obtained by using a certain number of processors [43]

$$Speedup = \frac{t(1)}{t(N)} \quad (5.1)$$

where  $t(1)$  is the computational time for running the software using one processor, and  $t(N)$  is the computational time running the same software with  $N$  processors. Ideally, an almost linear trend should be achieved as the number of processors used for the individual simulation grows. Clearly, however, reality leads us to an almost asymptotic trend as the number of processors used in parallel increases. The scaling test, in this case, was done with a computational grid structured with two million cells, all of the same size (2 cm). The characteristic procedure of this scaling process was based on "running" a basic setup, the same for all the simulations involved, each with a different number of processors (all powers of two). The set of simulations thus consisted of the one with 1 processor, 2 processors, 4 and so on up to a maximum of 32. The test was clearly performed for short physical times of a few tenths of a second, as the intention was not to obtain valid results of a perfectly developed motion field, but instead the interest lay in calculating this speedup value.

The table 5.2 clearly shows us the trend in speedup (which runs concurrently with the elapsed time<sup>1</sup>) and how this grows quite linearly with the increase in the number of processors employed in the computational computation.

## 5.2 Development of the simulation process

The results that will be shown in the following part of the chapter are therefore the result of the use of a large number of simulation hours on the *Legion* cluster, exploiting

<sup>1</sup>The elapsed time corresponds exactly to a silo time of five tenths of a physical second.

all 32 processors of the single node from time to time. When computationally very time-consuming work of this type is carried out, time is clearly an enemy; taking into account the fact that in order to obtain simulations that had completed 8.0 physical seconds, it was necessary to wait around 10 full days of computational computation, obviously in the case of the most complex and numerically heavy setups. This is something that must be taken into account, certainly in the all-round evaluation of the thesis, but also in the inevitable consideration of the need for future developments to complete the entire project. As for the indispensable post-processing work that was done at the end of each simulation, a visualisation programme called **ParaView** was used.

### 5.2.1 ParaView

**ParaView** is an open-source, multi-platform scientific data analysis and visualization tool that enables analysis and visualization of extremely large datasets. In this specific case ParaView has been used to read VTK files containing the fluid-dynamic variables that are the object of the analysis carried out. The VTK, the Visualization Toolkit, model is based on the data-flow paradigm. In this paradigm, data flows through the system being transformed at each step by modules known as algorithms. For further details on the full operation of the programme, please refer to the software guide [11].

### 5.2.2 Spectral analysis

This very brief section is useful to point out to the reader that in presenting the results obtained, we will also make use of some spectra for a deeper and more complete investigation. Spectral analysis is an almost indispensable tool in the detailed study of the turbulent nature of any fluid. In this specific case, it is functional in the study of flow homogenization and gives a measure of the success or otherwise of this attempt. The spectral analysis of the turbulent flow in an autoclave was carried out using a Matlab<sup>2</sup> script that makes use of the usual Fast Fourier transform (FFT) function, which is written  $Y = \text{fft}(X)$ . This function computes the discrete Fourier transform (DFT) of  $X$  using a fast Fourier transform (FFT) algorithm. In the graphs to be presented, however, it was decided not to report the values of the various quantities analysed in the frequency range, but rather in the wave number range. This has entailed necessary modifications to the Matlab code which, in this specific case of the `fft` function, is written to work precisely in the frequency range. This choice was dictated by the fact that in the literature these spectra are mostly found described in this way, and it is therefore easier to compare them with characteristic trends.

---

<sup>2</sup>It is a proprietary multi-paradigm programming language and numeric computing environment written in C. It allows matrix manipulations, plotting of functions and data, implementation of algorithms, creation of user interfaces, and interfacing with programs written in other languages [38]

### 5.2.3 Visualization of results

This paragraph will be written by scrolling through in sequential order exactly the same steps, and thus the same logical thread, that we have gone through during these months of work and that have led us from time to time to add an extra piece to the simulations and the setup, often and often improving the final result.

#### Preliminary phase

Given the start without any real reference points, the first tests performed served to understand a little about the numerical behaviour of the software used. Approximate setups were therefore prepared, and meagre in terms of the numerical methods applied. The first results therefore show us a motion field that is fairly 'crude' and not very representative of the physical flow pattern inside the pressurised chamber of the autoclave. It must always be borne in mind, as already discussed in detail in the third chapter of the thesis, that before starting with any type of simulation, the autoclave domain had to be concretely constructed in order to avoid simulating the motion field inside a simple parallelepiped. The first setups correspond to clearly less refined meshes, with a number of cells around 1.5 million and a size of 3 cm, thus quite coarse. Clearly this way of doing things in a DNS approach such as PLUTO's does not allow the visualisation of all scales of the turbulence because the excessive cell size does not allow the capture of the smallest structures of the turbulence. In particular, the geometric domain was constructed as follows:

1.	X1-grid	1	0.0	256	u	7.68
2.	X2-grid	1	-0.96	64	u	0.96
3.	X3-grid	1	-0.96	64	u	0.96

This is the grid script in PLUTO; the first term is self-explanatory and indicates the preferred direction, after which the first number, which in all three directions is always a 1, indicates the number of non-overlapping, adjacent one-dimensional grid patches making up the computational domain (in our case this choice is the optimal one since we are dealing with a uniform grid covers the whole physical domain). Moving to the left (*double*)(*int*)(*char*) represents respectively the extreme left-hand side of the domain, the number of points (and thus cells) and the type of grid (thus uniform in this case). Finally, the last value is clearly the one representing the extreme right of the domain. This set-up is characterised by numerical solutions that are still not very accurate; for example, with regard to spatial and temporal reconstitution, models have been adopted, respectively the linear and the RK2 (i.e. the 2-stage Runge-Kutta), which are not sufficiently robust numerically.

Looking at the two figures, one realises that the motion field representing the x-component of the velocity vector brings to light an obvious problem. The flow enters correctly through the annular inlet and follows the path dictated by the 'dome', which as already mentioned several times represents in a certain sense the autoclave door;

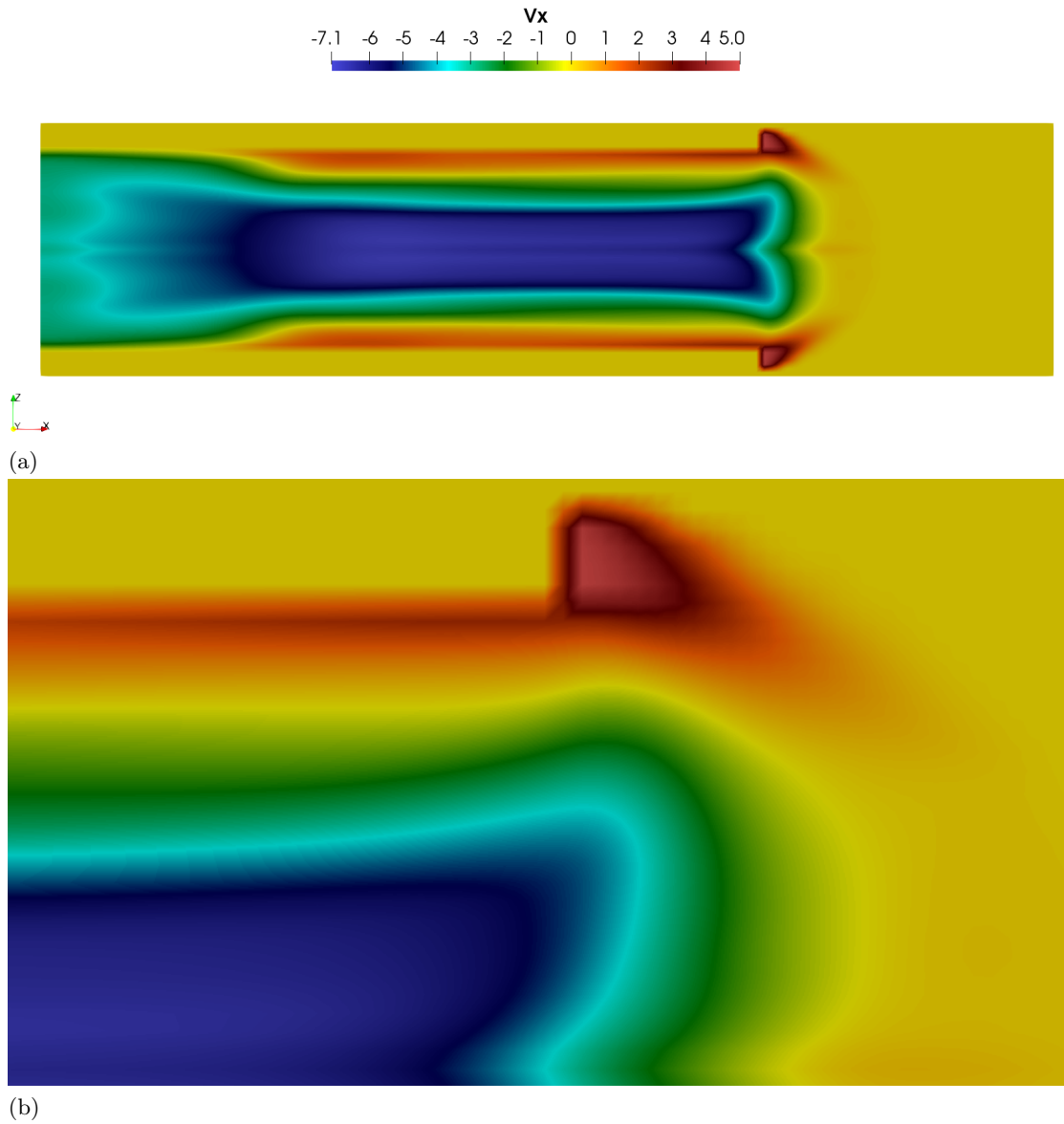


Figure 5.1: The figures 5.1a and 5.1b represent the motion field of the x component of the velocity vector after 2.0 physical seconds of simulation. By zooming in, we can see that there is a powerful backflow that continues along the wall to the bottom of the autoclave. This is clearly a numerical error that has no physical meaning whatsoever and will therefore have to be corrected.

however, the problem arises at the wall where a reflux problem is quite evident. The air in fact tends to flow backwards and this phenomenon creates a large recirculation zone that in no way represents valid physical behaviour but simply a numerical problem. This phenomenon was created when the *INTERNAL\_BOUNDARY\_REFLECT* flag was activated in conjunction with the *INTERNAL\_BOUNDARY* flag (the latter, which was used to 'freeze' the selected cells in time and which was discussed at length in chapter three); this flag, which is specified inside the basic *definitions.h*, is called in the file of interest *fluid\_interface\_boundary.c*. Here, the code has been reworked precisely to avoid this symmetry problem at the solid-fluid interface. In particular, what was happening was that the 'null flow' condition was not being met, so action was taken by implementing a *reflect* condition on the edge, i.e. a true *no\_slip* condition imposed on the wall. We went to take what is *the internal boundary* and then some cells formally internal to the mesh and considered them as boundary cells by applying a reflect condition. In this way, as we shall see, the problem is perfectly solved. In fact, without this modification, but trivially deactivating the *INTERNAL\_BOUNDARY\_REFLECT* flag, the phenomenon still remains, because this reflection problem at the solid-fluid interface persists. This can be clearly seen in the figures 5.2a and 5.2b. At the same time, however, it is very curious to note that the use of the WENOZ spatial reconstruction method enables this phenomenon to be greatly reduced; the reason for this is probably the greater stability of the method itself.

The same situation, obviously starting from the same physico-geometric setup described above 5.2.3, is also found in the attempt to discretize the equations of motion using the finite difference method, rather than the usual finite volume method. This approach will gradually be abandoned in order to concentrate exclusively on the second of the two, which gave us more numerical certainty and greater speed of calculation. In spite of this, figures 5.3a and 5.3b show us once again how the WENOZ method, compared to WENO3, guarantees a better spatial reconstruction, providing us with a more detailed field of motion and richer fluid structures.

The next step was therefore to modify the file *fluid\_interface\_boundary.c* in the manner explained above to resolve this problem encountered in the display of the motion field. From now on, the finite volume approach will be taken for granted in the treatment of the conservation equations as well as the use of WENOZ and RK3 as numerical methods for the spatial and temporal reconstruction of the solution. Then, for a better discretisation of the motion scales and with the aim of obtaining more accurate numerical results, the number of cells characterising the mesh was increased. At this point, therefore, the grid is made up as follows:

1.	X1-grid	1	0.0	320	u	6.4
2.	X2-grid	1	-0.8	80	u	0.8
3.	X3-grid	1	-0.8	80	u	0.8

As a result, we end up with a grid of cells with a uniform size of exactly 2.0 cm, and thus an improved spatial resolution compared to the previous configuration. The

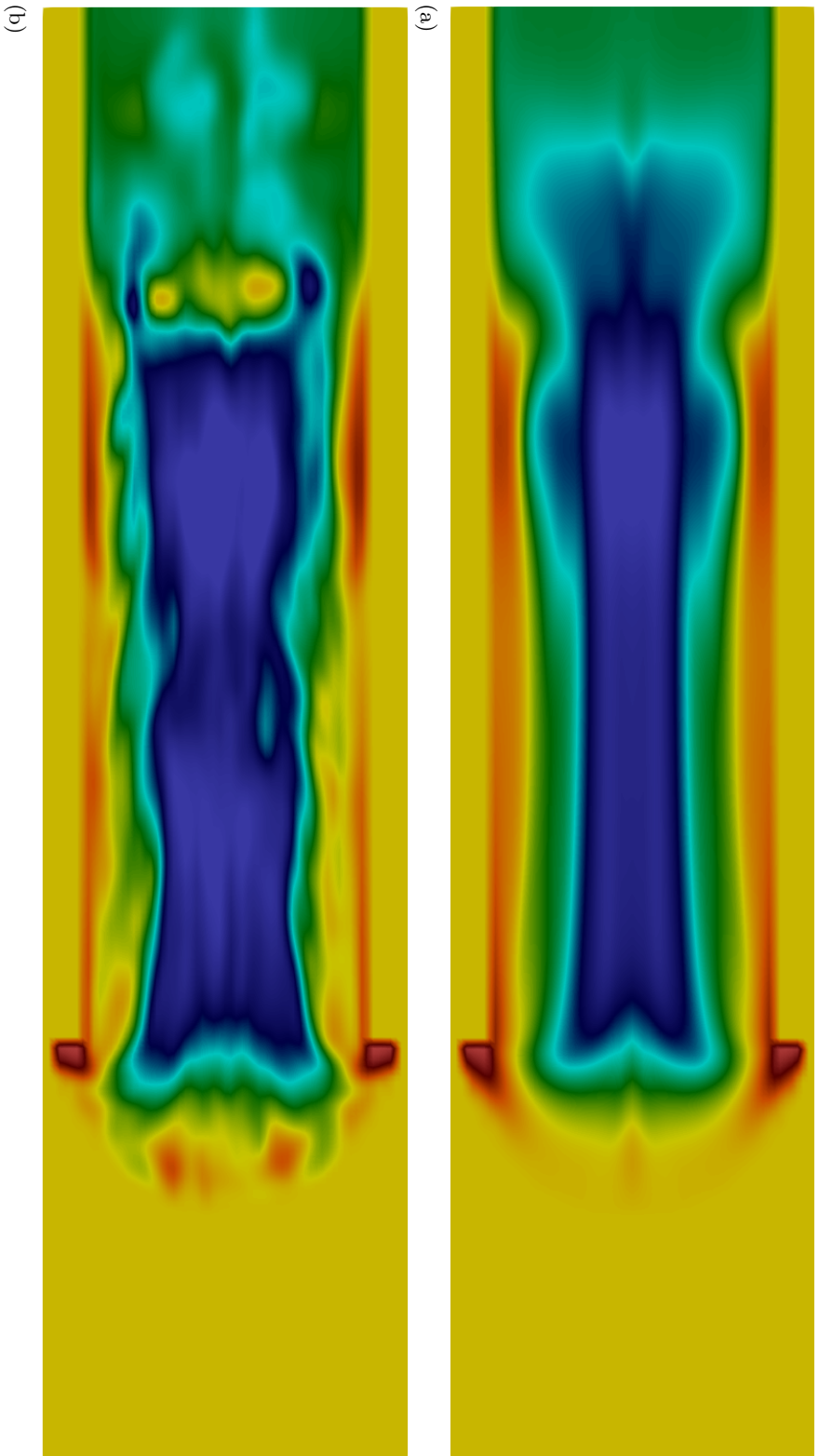


Figure 5.2: These two figures are the representation of the motion field<sup>a</sup> of the x-component of the velocity vector. In figure 5.2a, the numerical method of spatial reconstruction WENO3 was used, in contrast to figure 5.2b where the method applied is WENOZ. It is noticeable how, thanks to WENOZ, the problem of the large recirculation of the near-wall flow is somewhat alleviated without having intervened on the *fluid\_interface\_boundary.c*

<sup>a</sup>The colour bar has not been reported again, but the range of values also in this space is between -7.1 and 5.0.

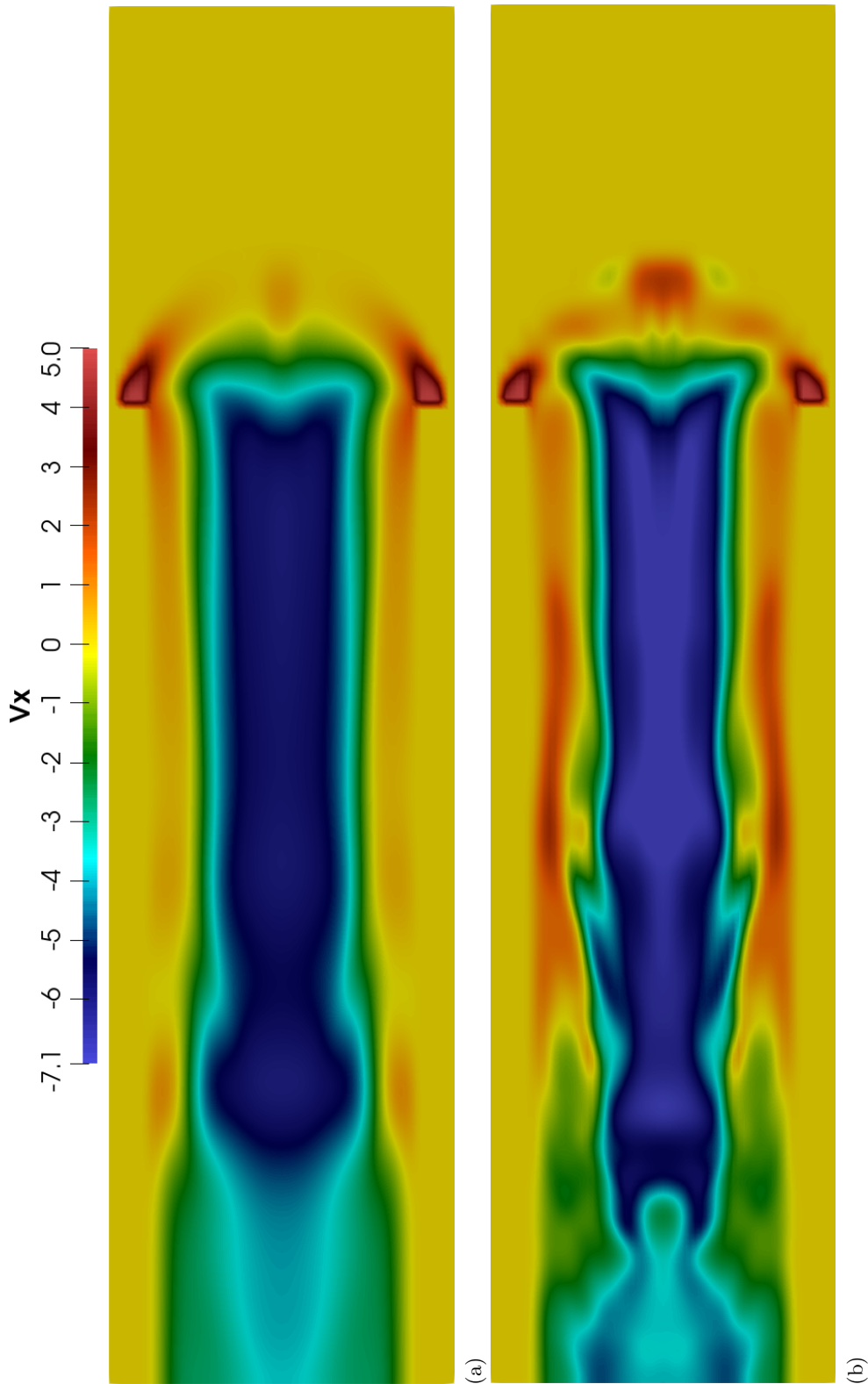


Figure 5.3: These image pairs were realised using finite difference discretization. Here, too, the backflow phenomenon appears; moreover, it must be considered that the finite difference method is much more time-consuming in terms of simulation time than the finite volume method. Between the figure 5.3a and the figure 5.3b, the WENOZ method gives us a better structured motion field with more scales of motion.

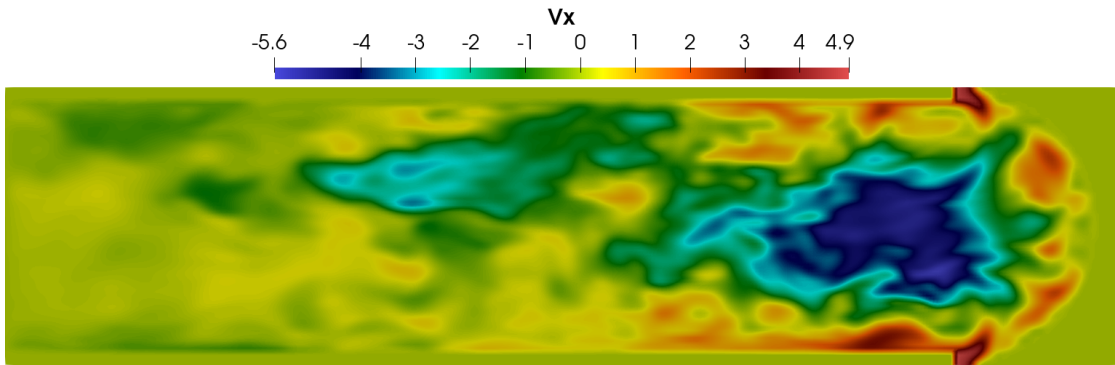


Figure 5.4: This is the visualisation of the velocity motion field captured with a grid of 2 million cells. There are a few swirling zones beginning to form here and there within the autoclave, giving the impression of a turbulent motion field. The snapshot shown above is that of a physical simulation time of 8.0 seconds, which is quite representative of an already highly developed field of motion.

DNS simulation leads us to highlight field structures that we were previously unable to visualise. Looking at the figure 5.4 we can observe a much more complex and complete field of motion, with the presence of the first vortices and turbulent structures. Despite a suction zone near the airflow outlet, the backflow problem that extended dangerously along the entire axial extension of the autoclave seems to have practically disappeared thanks to the modifications made.

If we try to increase the number of cells beyond eight million, thereby considerably thickening the mesh, the results we obtain are far superior in quality. This can be clearly seen in figure 5.5; the increase in spatial resolution allows smaller sized cells to numerically resolve motion scales of a comparable size. Clearly, at the time of post-processing, the visualisation of the motion field is benefited by this and the study of the turbulence structure is thus more detailed.

This preliminary analysis made it possible to observe the first snapshots of the internal motion field of an autoclave; first by inspecting and solving a few problems that had arisen, then by gradually increasing the number of cells and consequently also decreasing the size of the individual cell, it was possible to reach a condition whereby a wide range of motion scales began to be distinctly visible. The initial conclusions reached show how the approach of more precise and stable numerical methods makes it possible to reproduce a physical situation that is certainly more realistic and thus also more reliable. From now on, the geometric and numerical setup will be the same as in the rest of the developments.

### Tracer

At this point, it was decided to go ahead and definitively choose a geometric setup and mesh that would always be kept the same to ensure a certain type of continuity and

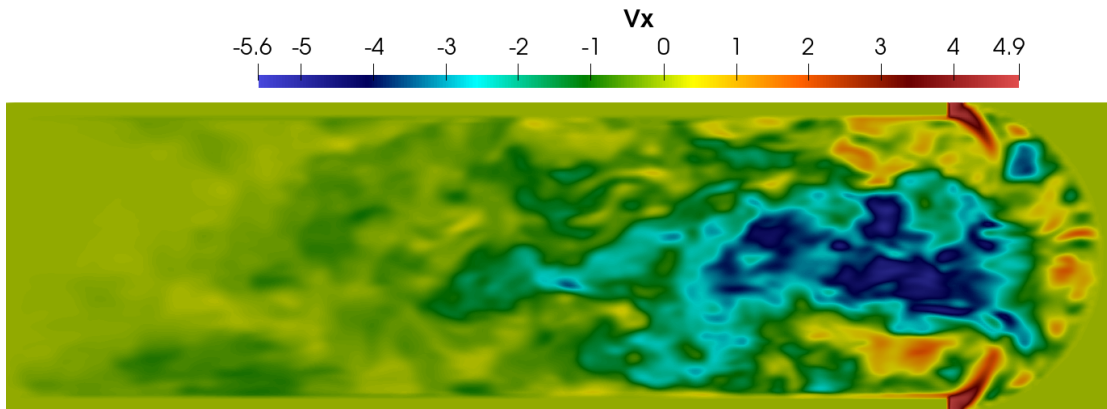


Figure 5.5: This is the visualisation of the velocity motion field captured with a grid of 8 million cells and after about 8.0 seconds of simulation. These times are sufficient for the airflow to reach the bottom of the autoclave and for the turbulence to fully develop. The system of vortex structures in this case is even more evident.

uniformity in the results obtained from the various simulations. The geometry of the autoclave was ultimately constructed as follows:

1.	X1-grid	1	0.0	512	u	6.144
2.	X2-grid	1	-0.768	128	u	0.768
3.	X3-grid	1	-0.768	128	u	0.768

The dimensions are very similar to those of a common industrial autoclave used for the polymerisation of large laminates used in aerospace and other fields. The aim is clearly, albeit with all the necessary simplifications, to remain as faithful as possible, as far as the external structure is concerned, to that of these large industrial machines. We then sampled the physical domain with a fairly fine mesh made up of more than 8 million cells equal to each other (8'388'608 cells, to be precise), each of them with a size of 1.2 cm uniform in all three dimensions. The physical results, referring back to the preliminary process, are in this sense realistic and reliable again due to the stability of the numerical methods chosen but also due to the high spatial resolution dictated by the sufficiently small size of the grid cells. The first detail that was added to enrich the fluid-dynamic simulation was to implement the injection of a kind of passive scalar that could give a measure of how and how fast the turbulence of the autoclave flow 'spreads' it across the domain. This passive scalar in PLUTO is called **Tracer** and obeys simple advection equations:

$$\frac{\partial Q_k}{\partial t} + \mathbf{v} \cdot \nabla Q_k = 0 \iff \frac{\partial \rho Q_k}{\partial t} + \nabla \cdot (\rho Q_k \mathbf{v}) \quad (5.2)$$

The second form gives the conservative equation and it is the one actually being discretized by the code.

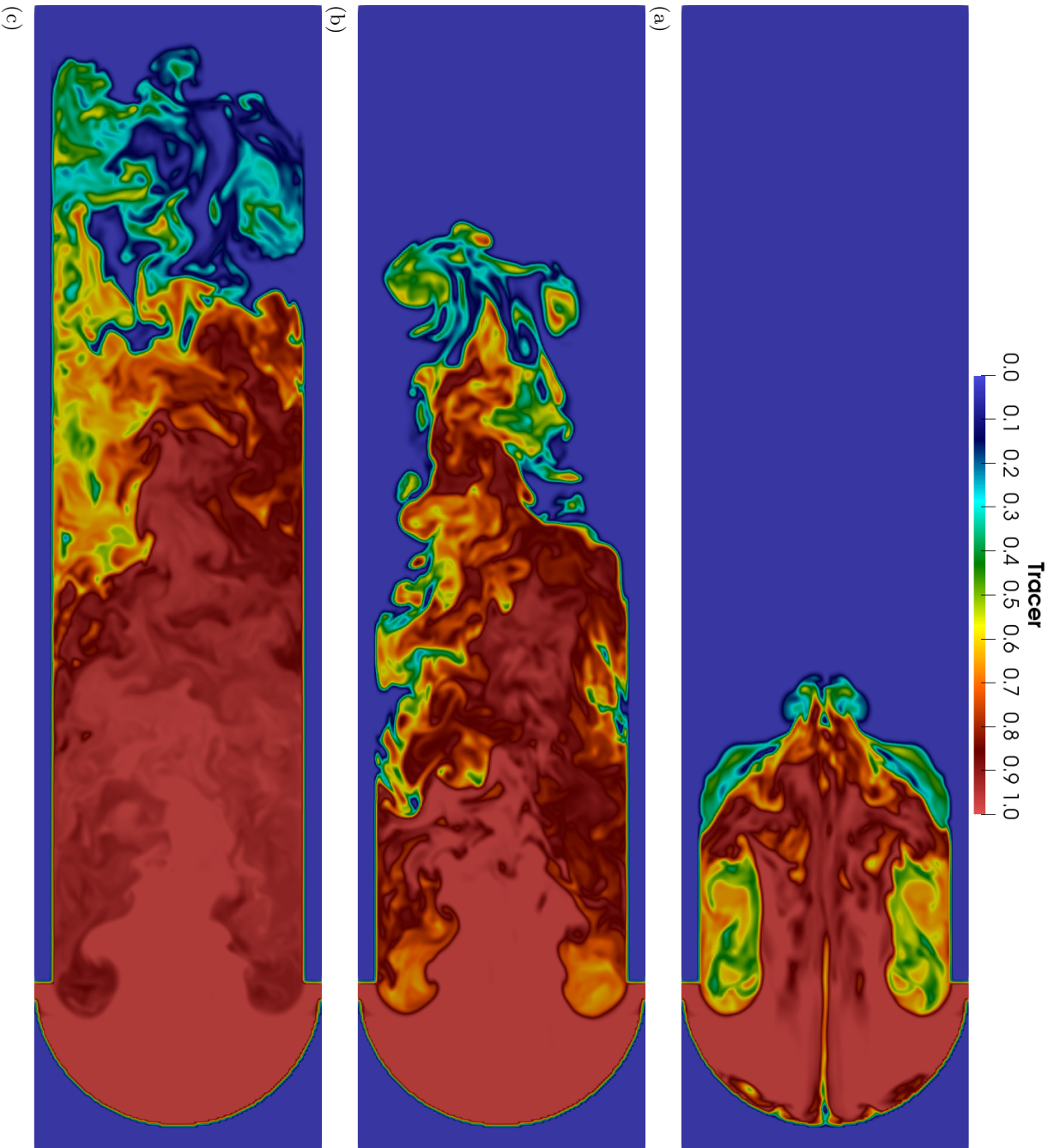


Figure 5.6: Shown are 3 snapshots of the Tracer diffusion inside the autoclave. The succession of the figures, at three different instants (from figure 5.6a to figure 5.6c we go from 1.0 seconds, 2.5 seconds up to 4.4 seconds of simulation), allows us to observe how it is slowly diffused throughout the volume, as a direct action of the turbulence present. The value of the passive scalar is in a range between 0.0 and 1.0.

These visualisations are real thermometers that help us in some way to assess the degree of turbulent homogenization achieved within the system. This concept, which may be somewhat obscure at the moment, will be clarified in a much better way later on when mechanisms that help the turbulence phenomenon to homogenize will be introduced and a comparison will be made between the momentum field obtained with and without their implementation in order to grasp their possible beneficial contribution.

### **LES filter - activation subgrid model**

PLUTO is a fluid-dynamic computation software that uses a DNS approach for solving the equations of motion. In order to switch to the LES approach, an additional module must be implemented to the rest of the source files. The main problem we have to deal with is the limited, albeit considerable, computational resources. This makes it impossible to adopt an overly refined grid type in the case of DNS simulations for purely practical reasons. So what we are going to do is to adopt a kind of local 'probe' aimed at monitoring the presence of small scales; in the case where their presence is negligible then what is done is to solve DNS directly, otherwise a large-eddy approach is adopted in those areas where the indicator is above the threshold (a threshold value for vorticity). In this specific case, the LES involves enriching the stress tensor with an additional term that is described by the Smagorinsky model 2.5.3. In this way, there is theoretically also a saving in terms of the actual calculation time. Looking at the two figures 5.7a and 5.7b, one can already glimpse the advantage of the LES approach to some extent: with the same mesh size, thanks to the introduction of a modelling system for the smallest scales of motion one is able to visualise during post-processing a wider range of scales within the energy cascade; without this modelling in fact the DNS simulation would not be able to resolve vortical structures smaller than a certain size which is precisely dictated by the size of the cells that make up the grid and the only way to escape this problem would be to reduce the size of the cells themselves.

Having thus reaffirmed the convenience of LES in describing a fully developed turbulent flow such as we find within the autoclave, we can now focus on the problem of homogenization and the methods that can be employed to aid its achievement.

### **Introduction of the hatches system**

Before proceeding, it may be useful to make a brief summary of all the choices and improvements that have been made from time to time within the simulation setup. Starting practically from scratch, we began by first constructing the actual computational domain in detail, going some way to 'cut out' the autoclave geometry; then, after various attempts and comparisons, the optimal numerical configuration was chosen in terms of stability and numerical convergence and in terms of the most realistic representation of the modelled physical phenomenon; we then opted for a sufficiently refined grid, without exaggeration, sampled through the use of an LES model. At this point, one can then concentrate, as mentioned at the end of the previous paragraph, on the concept of turbulent homogenization, which is the nerve centre of the entire project, and on the

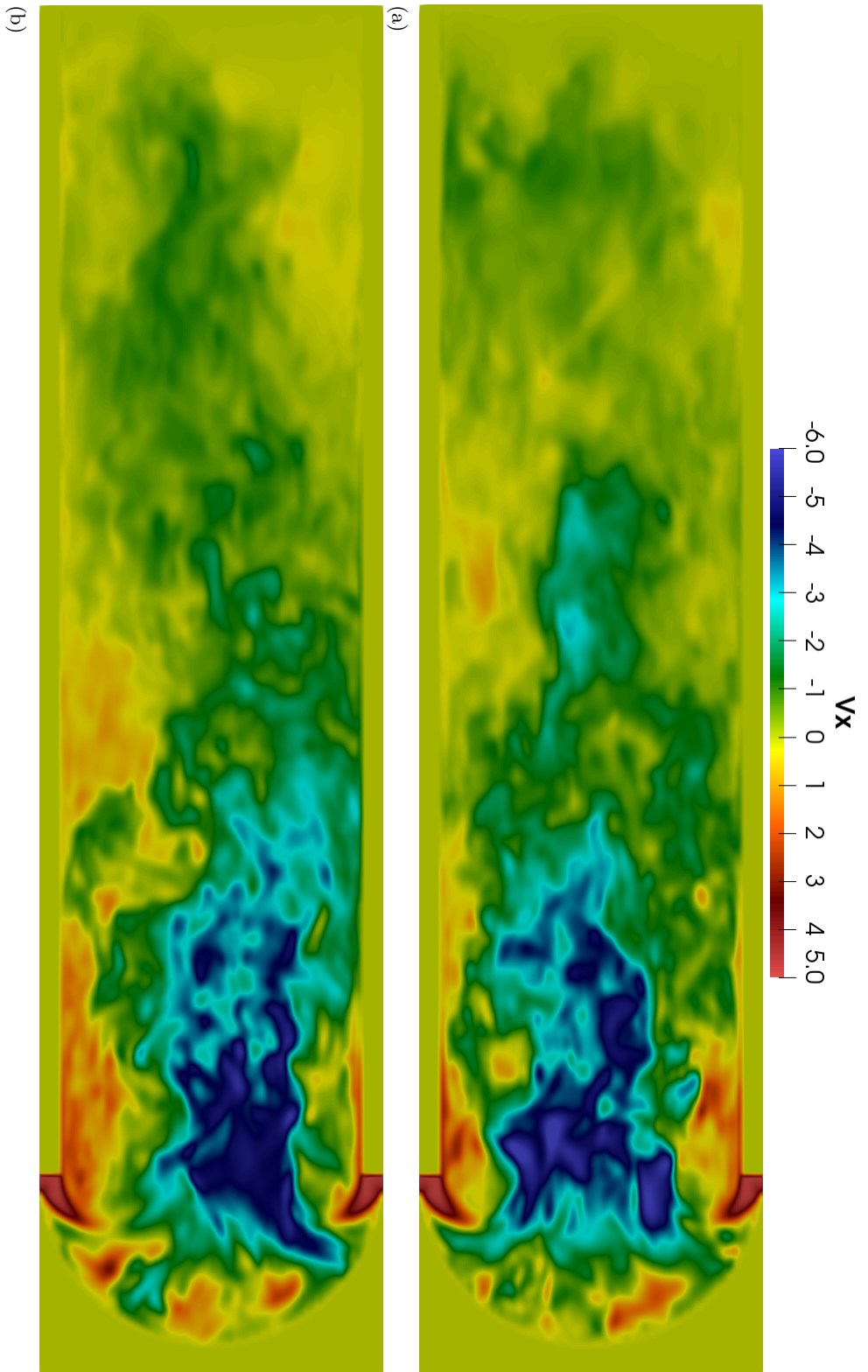


Figure 5.7: The figure 5.7a represents the velocity component parallel to the longitudinal axis of the autoclave and is the result of a direct approach (DNS) for solving the equations of motion. In the image 5.7b, on the other hand, the LES filter has been applied and thus a new criterion for solving the smallest scales of motion. In both cases, the simulation time is approximately 4.5 seconds.

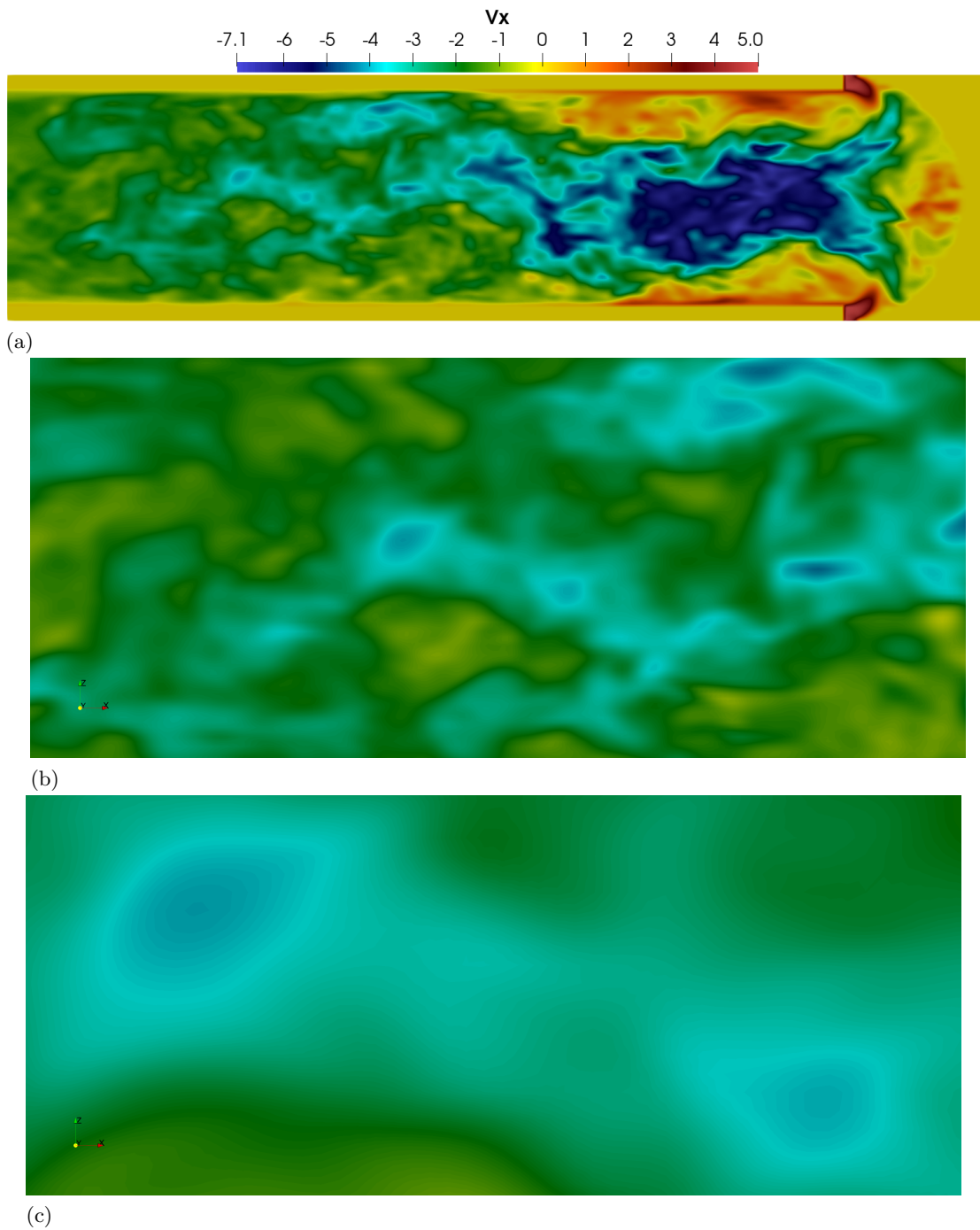


Figure 5.8: The motion snapshot shows how the air flow, after 7.5 seconds, has already reached the end of the autoclave. The simulation was performed with the LES filter present. The 5.8b and 5.8c represent the zoom of two vortical structures captured and resolved by the computational calculation clearly and distinctly.

installation of certain mechanisms aimed at achieving it. The idea was to build on the computational domain what we independently called hatches. These are a few openings positioned where in theory in industrial autoclaves the air recirculation ducts are placed; the air flow is diverted inside these 'windows' and made to enter the chamber that hosts the laminate processing. In this sense, it was decided to compare two different configurations: in the first, these openings are located at the top and bottom of the autoclave in correspondence with the longitudinal axis, and of all the 8 hatches present, 4 open randomly at a time; the second configuration instead involves the random generation of 10 hatches each time in different positions, always on the internal surface of the autoclave. In both the first and the second case, a timer of 1.0 second<sup>3</sup> is used to scan the supply of air through these openings. An interesting aspect is to analyse the exit velocity from the hatches, as the flow will suffer an inevitable pressure drop. Compared to the value, in modulus, that the velocity vector has at the outlet of the annular inlet, at these openings the modulus of the velocity is  $3\frac{m}{s}$ .

**Kinetic energy** In an attempt to understand the real effectiveness of hatches, the quantity that, as we shall see later, together with the Q-criterion, can give us interesting feedback is the kinetic energy<sup>4</sup>. If in fact the visualisation of the field of motion shows us that this scalar magnitude is distributed more uniformly and therefore homogeneously over the analysed plane, then this means that there has certainly been a good result in terms of the homogenization of the system.

In this regard, in the two groups of images 5.9 and 5.10 we can observe the motion field of kinetic energy at an intermediate time of 4.0 seconds. Although this time instant is not entirely ideal, as the momentum field is not fully developed, it is already possible to see improvements in terms of a more effective homogenization of the system. Particularly in the snapshot of figure 5.10c, compared to 5.10a and 5.10b, this analysis is placed even more prominently: these images, which depict the transverse plane of the autoclave at a station approximately halfway<sup>5</sup> along the length of the entire chamber, show how a more uniform distribution of kinetic energy is achieved in the case of hatches placed at random positions within the chamber. These results, albeit preliminary, have led us to the conclusion of continuing the turbulence homogenization analysis by omitting the configuration with the hatches placed at the top and bottom along the longitudinal axis of the autoclave and keeping only the one in which the hatches are from time to time generated in different and random positions around the entire side wall of the autoclave.

This time if instead we analyze the two cases, with and without hatches, at a more advanced time period, where the flow has managed to develop completely, then the differences should become even more marked. Looking at the two groups of figures,

---

<sup>3</sup>This, along with others, is definitely one of the parameters on which you can work to see if you can get improvements as far as the final result of the simulations. These things will be discussed in the final chapter of the thesis 6.

<sup>4</sup>A kinetic energy per unit mass was calculated in Paraview and thus:  $E = \frac{1}{2}(v_{x1}^2 + v_{x2}^2 + v_{x3}^2)$ .

<sup>5</sup>It was considered for the analysis of the problem that this position was the most appropriate for a consistent analysis of the results brought by the hatches against those of the autoclave without these openings.

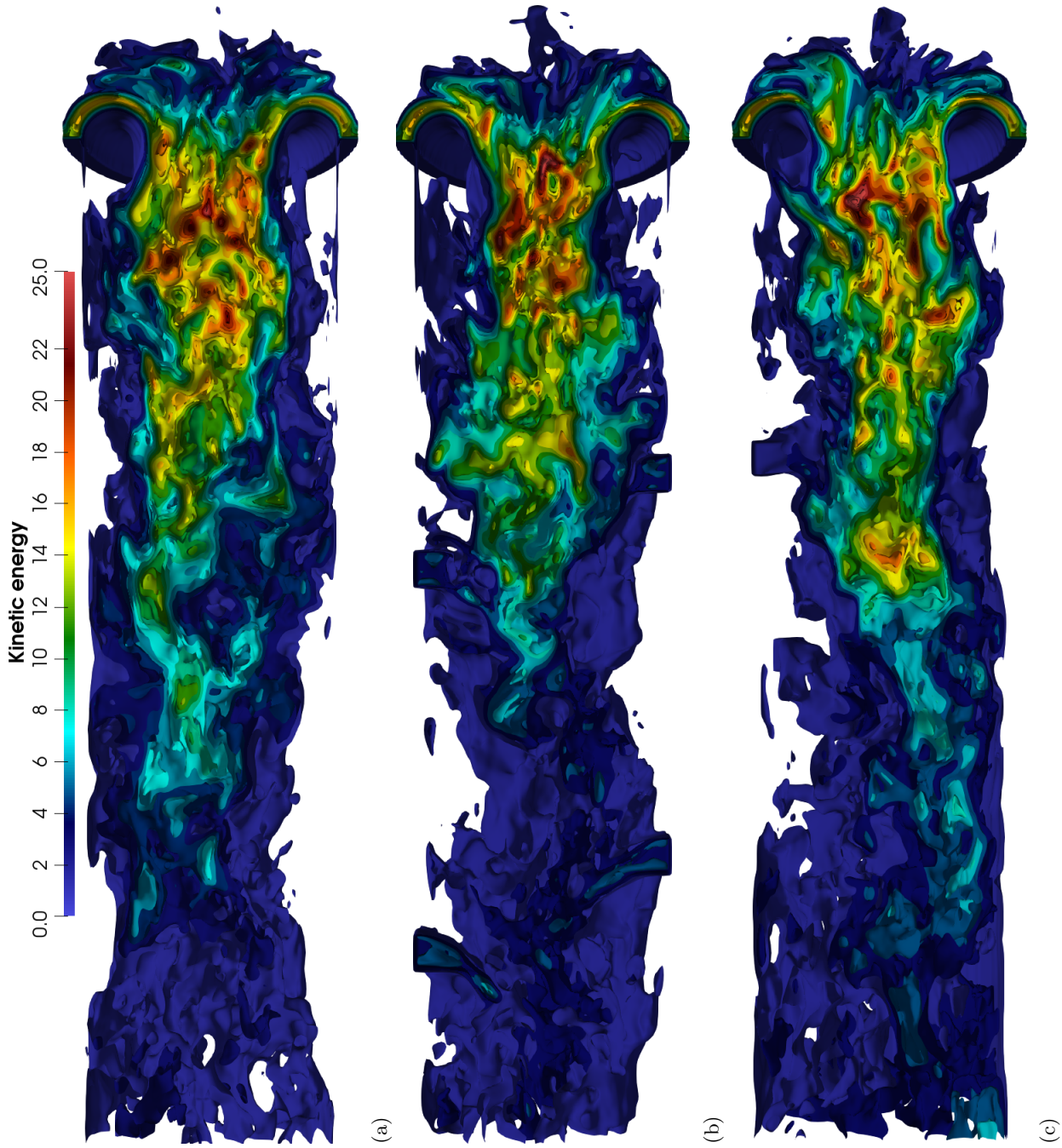


Figure 5.9: Shown here are three images depicting the motion field of kinetic energy on the longitudinal axis of the autoclave. It is a very important parameter in understanding the homogenization of turbulence. The figure 5.9a represents the condition with no hatches; the figure 5.9b depicts the condition where the hatches are placed high and low; finally, the third and last image (5.9c) represents the condition where the apertures are placed randomly.

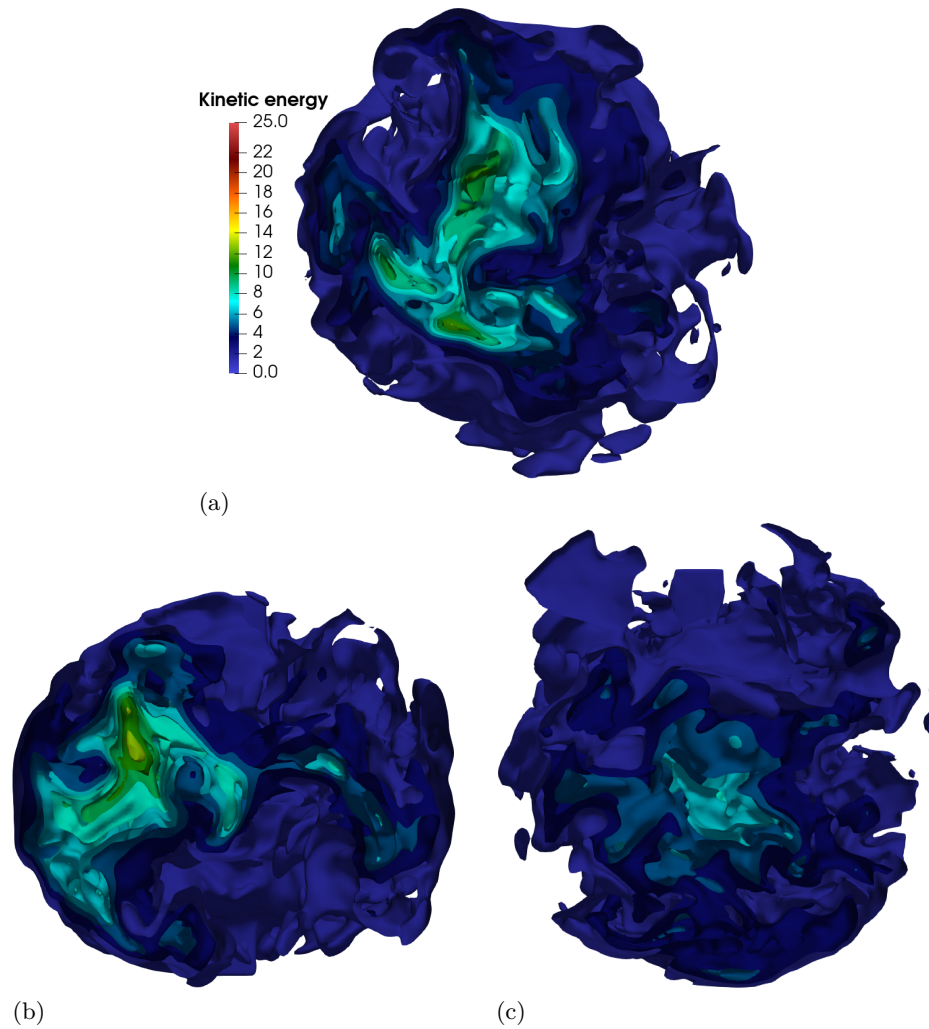


Figure 5.10: Here, the motion field of kinetic energy is depicted in a plane transverse to the autoclave axis at a station  $x = 2.55$  m. The first figure at the top, (5.10a), represents the condition without hatches; in the line below from left to right we find the figure (5.10b) depicting the condition in which the hatches are placed at the top and bottom, and the (5.10c) representing the condition in which the hatches are placed randomly.

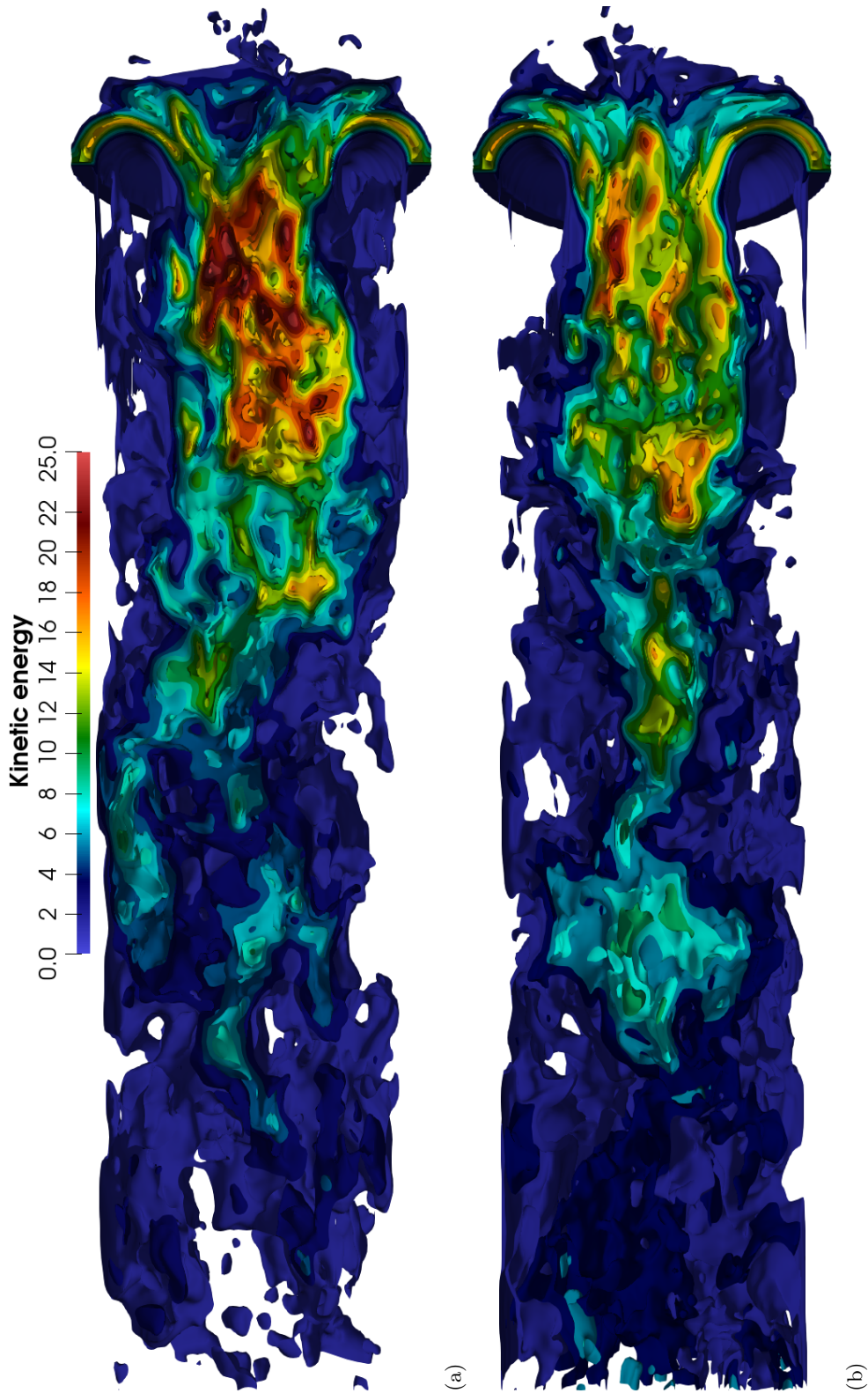


Figure 5.11: These are 3D contours of the kinetic energy of the xz plane exactly on the axis of the autoclave ( $y = 0$ ) after 7.5 seconds of simulation. The figure 5.11a represents the base case, while the 5.11b represents the autoclave with hatches.

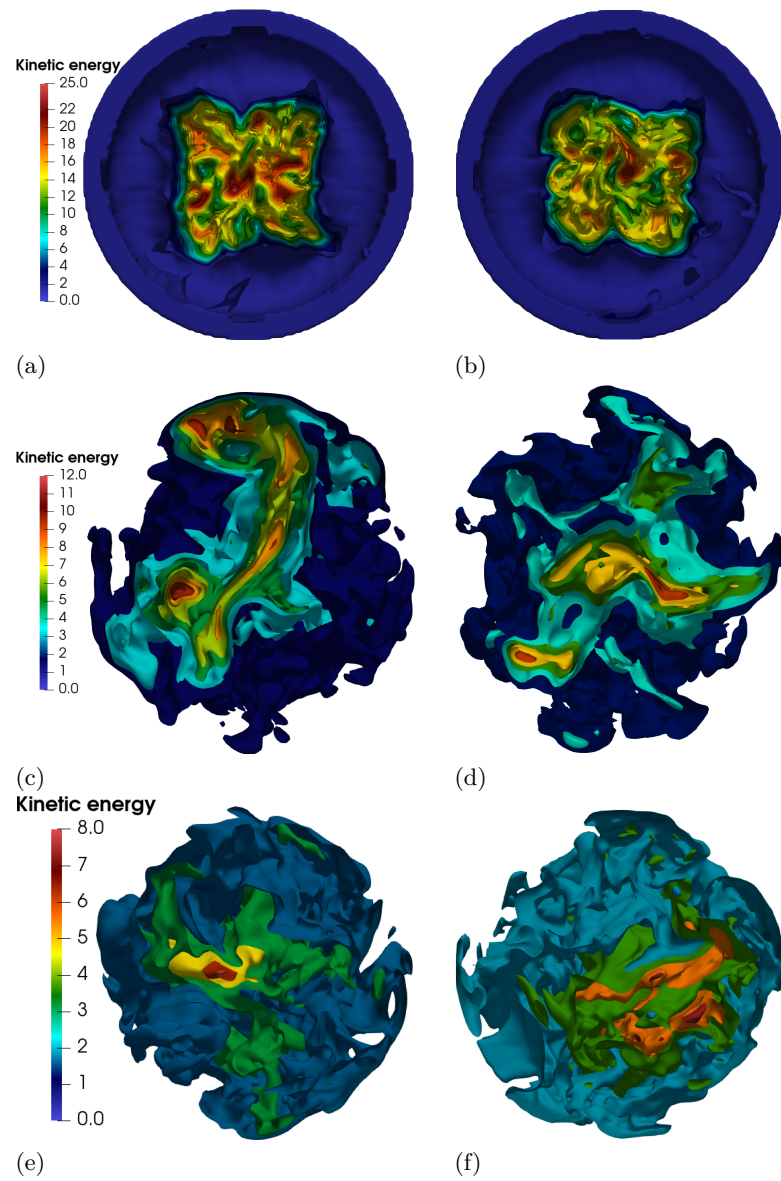


Figure 5.12: The figures represent once again the contours of the kinetic energy on the  $yz$  plane at different positions along the longitudinal axis of the autoclave, at the same time (7.5 seconds). The left column belongs to the case without implemented hatches, while the right column belongs to the case with the hatches in random positions. The three stations considered, from top to bottom, moving towards the bottom of the chamber are:  $x = 5.1\text{m}$  (5.12a and 5.12b);  $x = 2.55\text{m}$  (5.12c and 5.12d);  $x = 1.275\text{m}$  (5.12e and 5.12f).

5.11 and 5.12, we can see just how the presence of some disturbing spots here and there scattered around the room can actually favor the homogenization of the flow in autoclave. This behaviour is also emphasised by the characteristic of turbulence itself to carry the passive scalar, as we can observe in figure 5.13.

That of figure 5.13 is a very important result. In fact, this shows us how the importance of achieving a homogenous turbulence field inside the autoclave also relates to the speed at which it is achieved. This is because the curing process is a multi-step process with different temperature ramps alternating with holding periods, and if homogenization in the chamber is achieved in less time then the whole process benefits. Supporting all these considerations are the spectral analysis graphs. It was decided to take the kinetic energy values at a single time instant in both the xy and yz planes and thus plot the values in the wave number range, and not in the frequency range as is usual with Fourier analysis.

Spectral analysis was done by sampling the Kinetic Energy data in two planes of the domain, one parallel to the autoclave axis and the other transverse to it. This sampling work was done during post-processing, directly from ParaView. As can be seen in the proposed graphs (5.14, 5.15, 5.16, 5.17, 5.18, 5.19), the basic idea was to select multiple stations of the z-coordinate at which to take kinetic energy values, so that an analysis could be made on the degree of homogeneity of the turbulence that would take into account the possible difference that is created in moving from the center of the chamber to a position very close to the side wall. In fact, the graphs of the two cases (with and without hatches) do not show all these large differences that were more apparent. However, the spectra corresponding to the y-z planes show, most of all, how this phenomenon of turbulent homogeneity is actually enhanced in the case where the localized velocity perturbations, placed here and there in the autoclave, are present. This is especially evident in the center of the autoclave. It is however necessary to reiterate how all the results presented here are entirely preliminary and subject to future more in-depth and detailed analysis.

**Q-Criterion** The concept of a vortex is something that has not yet found a specific definition. One often hears, in connection with vortices related to the turbulent motion of any flow, of coherent structures. Vortex dynamics therefore governs the interaction, combination and evolution of these structures [2]. One of the most popular methods of visualising vortices and one that also returns the best results is undoubtedly that of the Q-criterion. Some researchers defined an 'eddy' as the region with positive second invariant,  $Q$ , of  $\nabla\mathbf{u}$ , with the additional condition that the pressure be lower than the ambient value [2].  $Q$  is defined as:

$$Q \equiv \frac{1}{2}(u_{i,i}^2 - u_{i,j}u_{j,i}) = \frac{1}{2}u_{i,j}u_{j,i} = \frac{1}{2}(\|\boldsymbol{\Omega}\|^2 - \|\mathbf{S}\|^2) \quad (5.3)$$

Thus positive values of  $Q$  are indicative of areas in the flowfield where the vorticity dominates and negative values of  $Q$  are indicative of strain rate or viscous stress dominated areas. This is what we will use to visualize vortical structures in the flow. Having

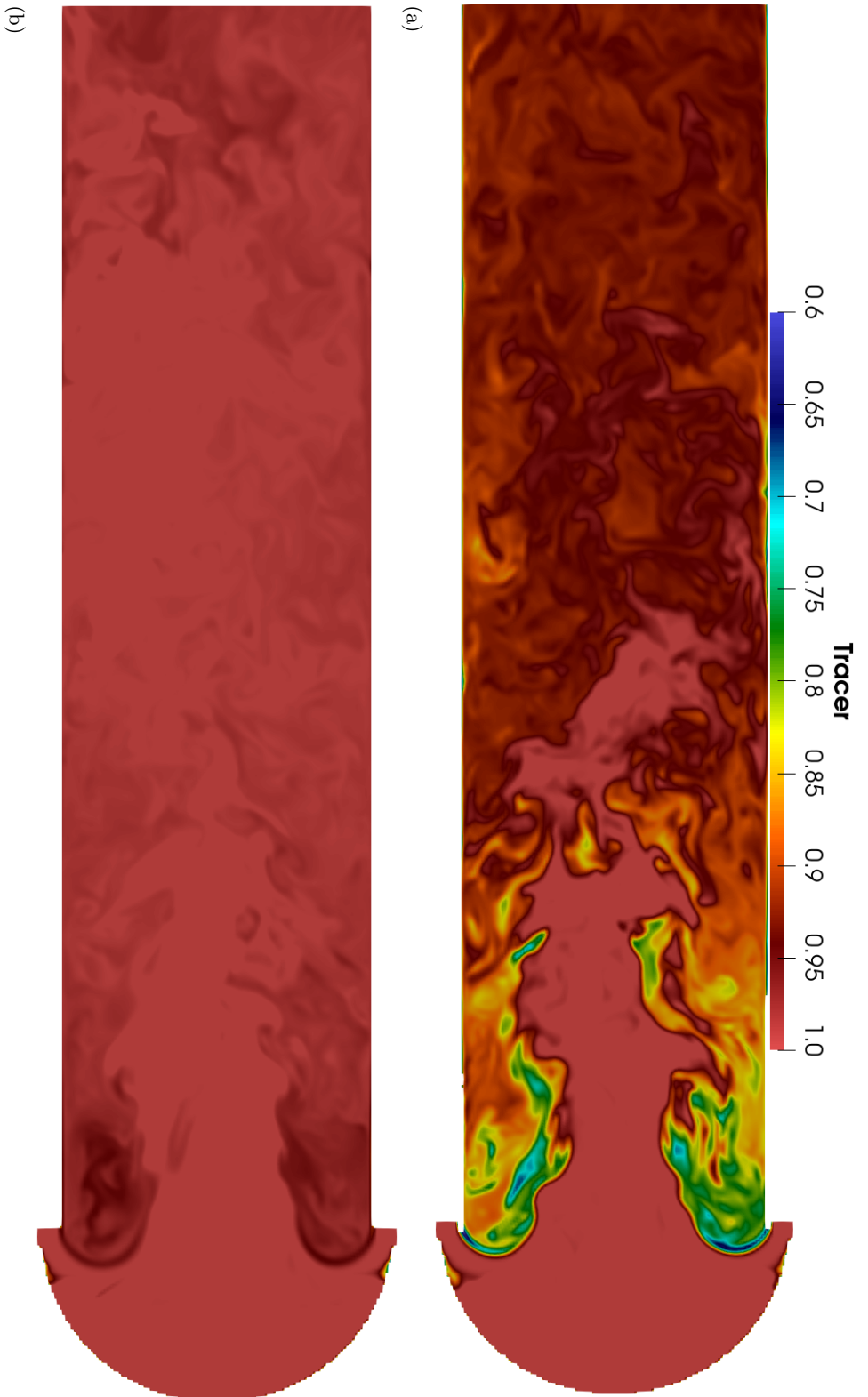


Figure 5.13: In these two figures we can clearly see the concept of improved and accelerated homogenization that is dictated by the presence of the hatches. In the figure 5.13a without the hatches it is noted that the passive scalar introduced in the system has not yet been well distributed throughout the volume, unlike the figure 5.13b where instead the implementations of localized perturbations of better speeds and you accelerate just such distribution process. Both are snapshots taken after 7.5 physical seconds of simulation.

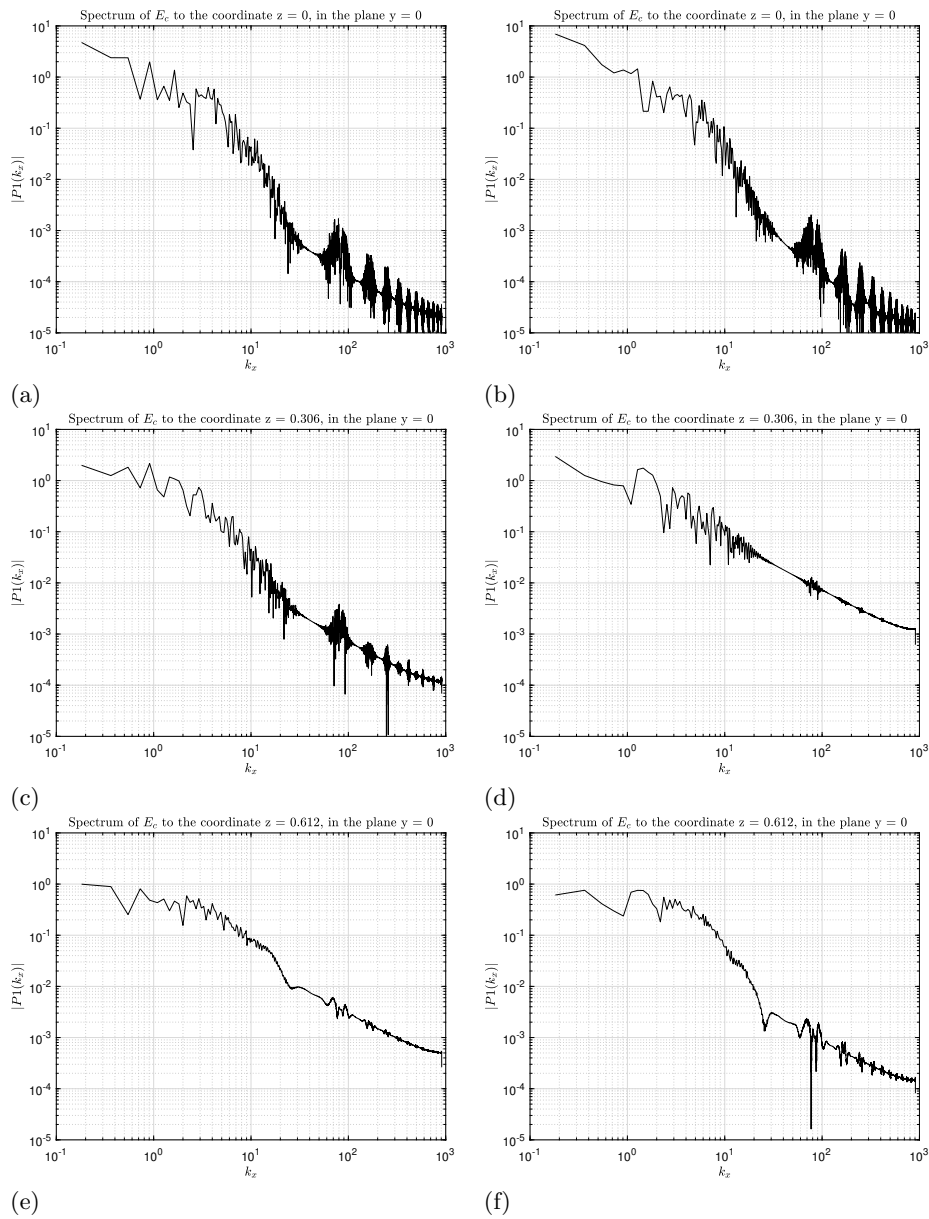


Figure 5.14: These figures represent the spectra of Kinetic Energy in the wave number range. The comparison made is between simulations with the autoclave configuration with random hatches (left column) and those with the autoclave without these additional tools (right column). In this case the  $y=0$  plane, parallel to the autoclave axis, is analyzed; then in this which is more generally the  $x$ - $z$  plane 10000 points along the  $x$  direction are sampled at three different stations of the  $z$  coordinate:  $z=0$ ,  $z=0.306$  and  $z=0.612$ .

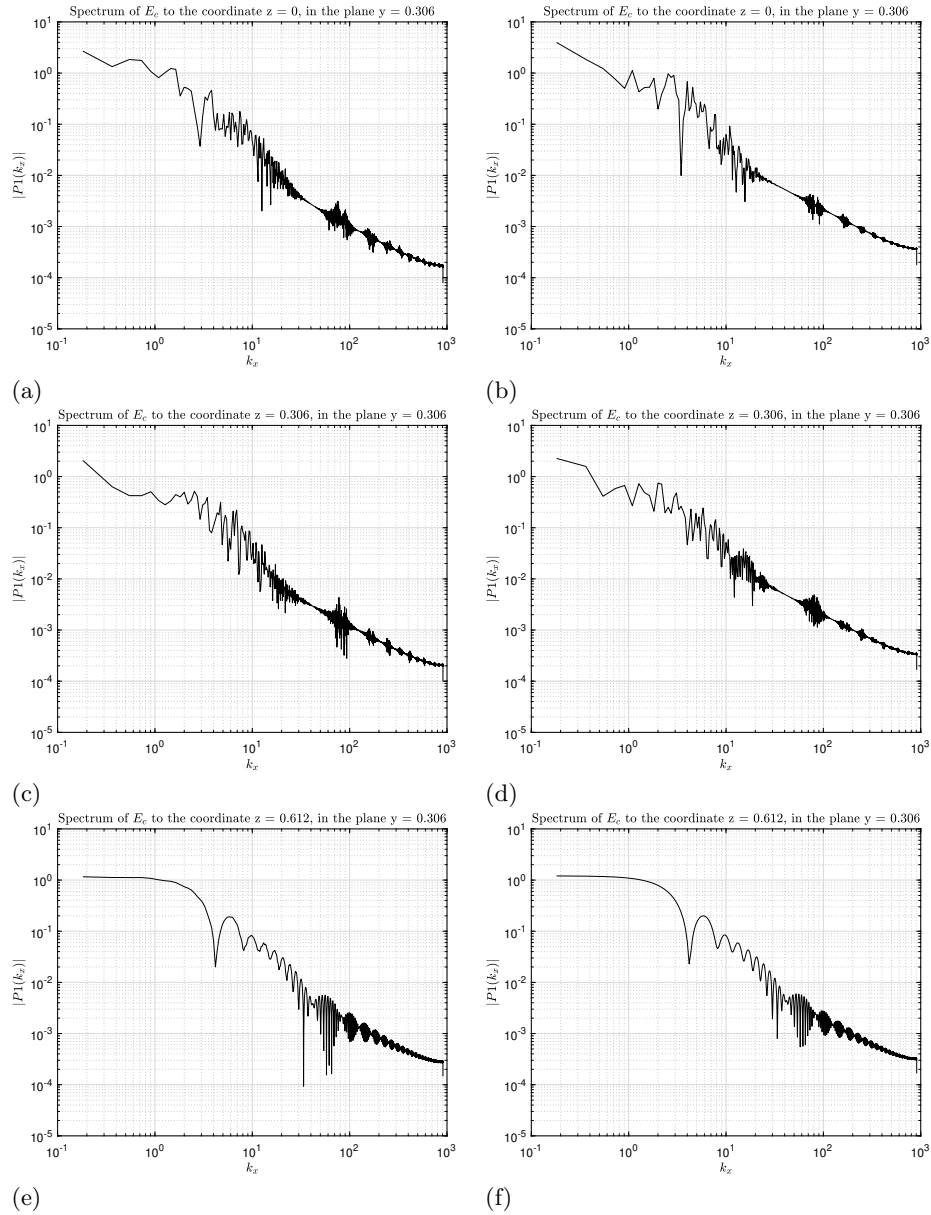


Figure 5.15: These figures represent the spectra of Kinetic Energy in the wave number range. The comparison made is between simulations with the autoclave configuration with random hatches (left column) and those with the autoclave without these additional tools (right column). In this case the  $y=0.306$  plane, parallel to the autoclave axis, is analyzed; then in this which is more generally the  $x$ - $z$  plane 10000 points along the  $x$  direction are sampled at three different stations of the  $z$  coordinate:  $z=0$ ,  $z=0.306$  and  $z=0.612$ .

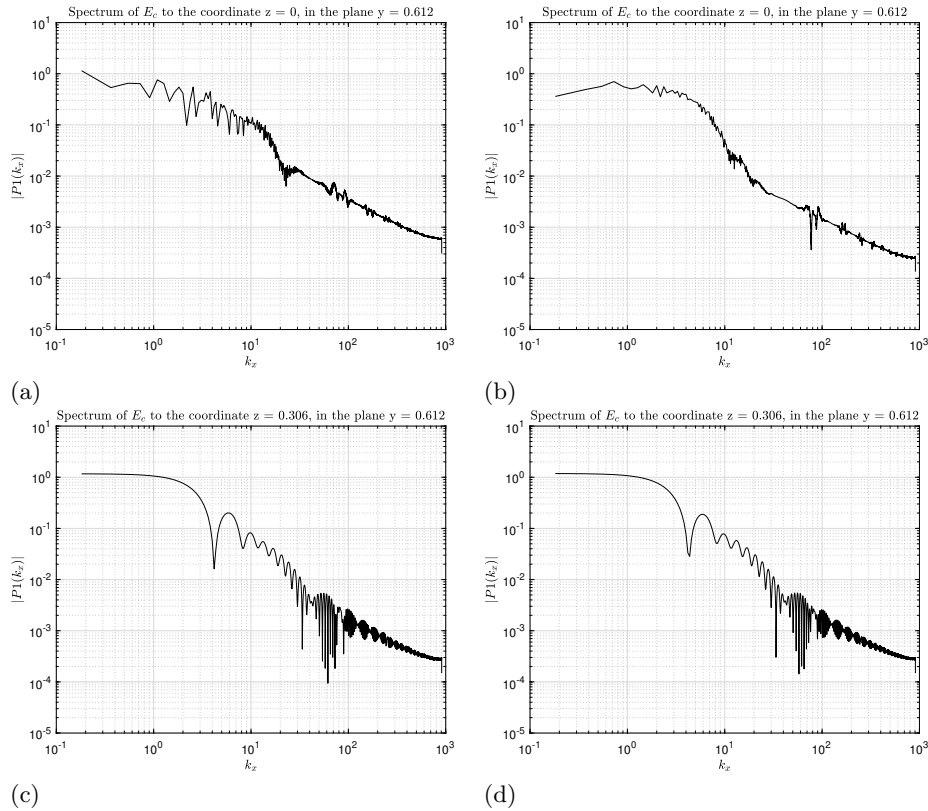


Figure 5.16: These figures represent the spectra of Kinetic Energy in the wave number range. The comparison made is between simulations with the autoclave configuration with random hatches (left column) and those with the autoclave without these additional tools (right column). In this case the  $y=0.612$  plane, parallel to the autoclave axis, is analyzed; then in this which is more generally the  $x$ - $z$  plane 10000 points along the  $x$  direction are sampled at three different stations of the  $z$  coordinate:  $z=0$ ,  $z=0.306$  (in this case the  $z=0.612$  coordinate was characterized by null values and for this reason it was left out).

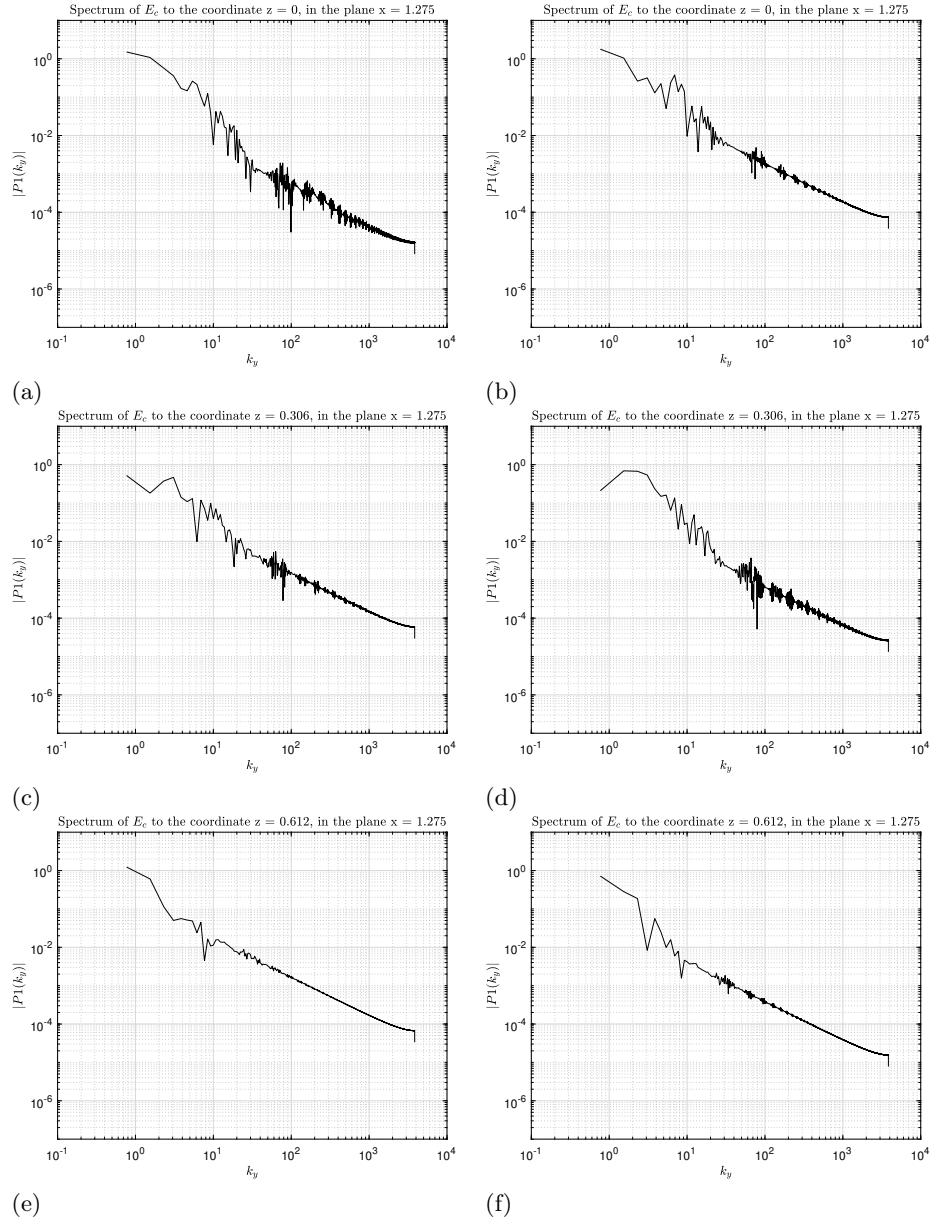


Figure 5.17: These figures represent the spectra of Kinetic Energy in the wave number range. The comparison made is between simulations with the autoclave configuration with random hatches (left column) and those with the autoclave without these additional tools (right column). In this case 10000 points are sampled along the y-direction, in y-z planes transverse to the autoclave. The plane corresponding to these graphs is  $x=1.275$  and on it three different stations of the z-coordinate are selected:  $z=0$ ,  $z=0.306$ ,  $z=0.612$ .

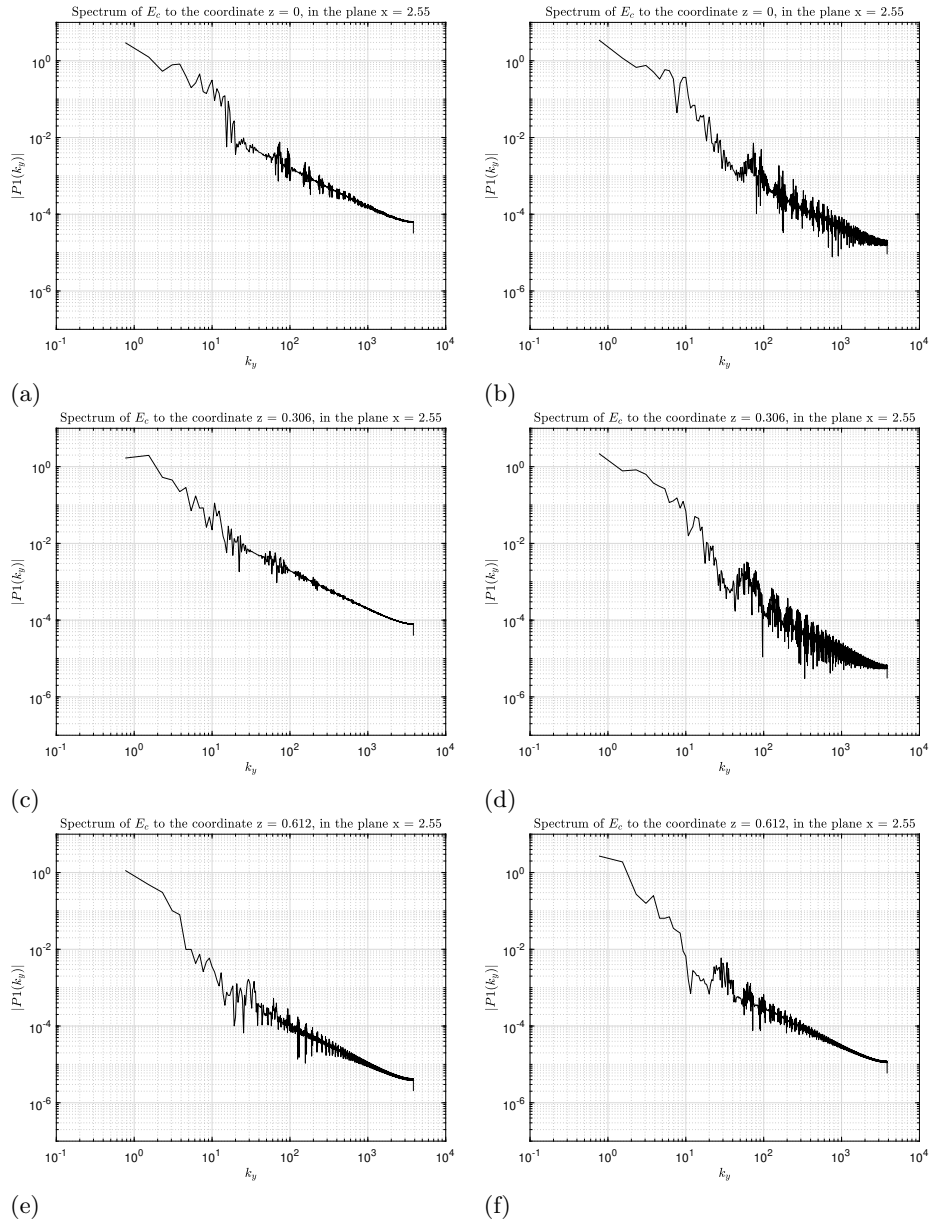


Figure 5.18: These figures represent the spectra of Kinetic Energy in the wave number range. The comparison made is between simulations with the autoclave configuration with random hatches (left column) and those with the autoclave without these additional tools (right column). In this case 10000 points are sampled along the y-direction, in y-z planes transverse to the autoclave. The plane corresponding to these graphs is  $x=2.55$  and on it three different stations of the z-coordinate are selected:  $z=0$ ,  $z=0.306$ ,  $z=0.612$ .

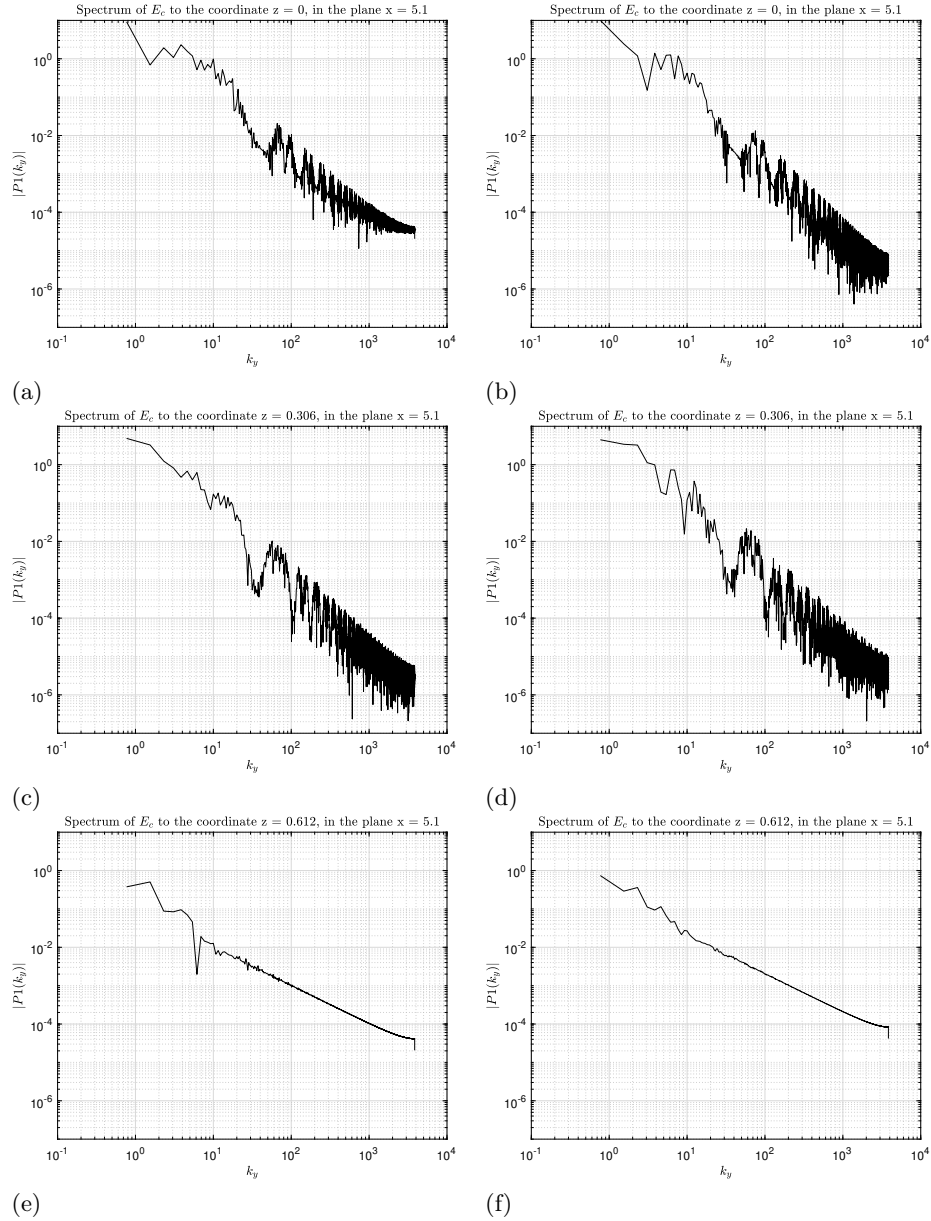


Figure 5.19: These figures represent the spectra of Kinetic Energy in the wave number range. The comparison made is between simulations with the autoclave configuration with random hatches (left column) and those with the autoclave without these additional tools (right column). In this case 10000 points are sampled along the y-direction, in y-z planes transverse to the autoclave. The plane corresponding to these graphs is  $x=5.1$  and on it three different stations of the z-coordinate are selected:  $z=0$ ,  $z=0.306$ ,  $z=0.612$ .

thus introduced the concept of the Q-criterion, it is easier to understand how it is a highly relevant parameter in describing the homogeneity and anisotropy of a turbulent flow.

The figures 5.20 and 5.21 represent the Q-criterion contours of 100 and 1000 respectively. After a sufficiently long simulation time (about 8 seconds) we see how the distribution of eddies and the intensity of vorticity is much better spread throughout the volume where the hatches are present. This leads to the conclusion that the degree of homogeneity of the turbulence is greater in the two snapshots 5.20b and 5.21b.

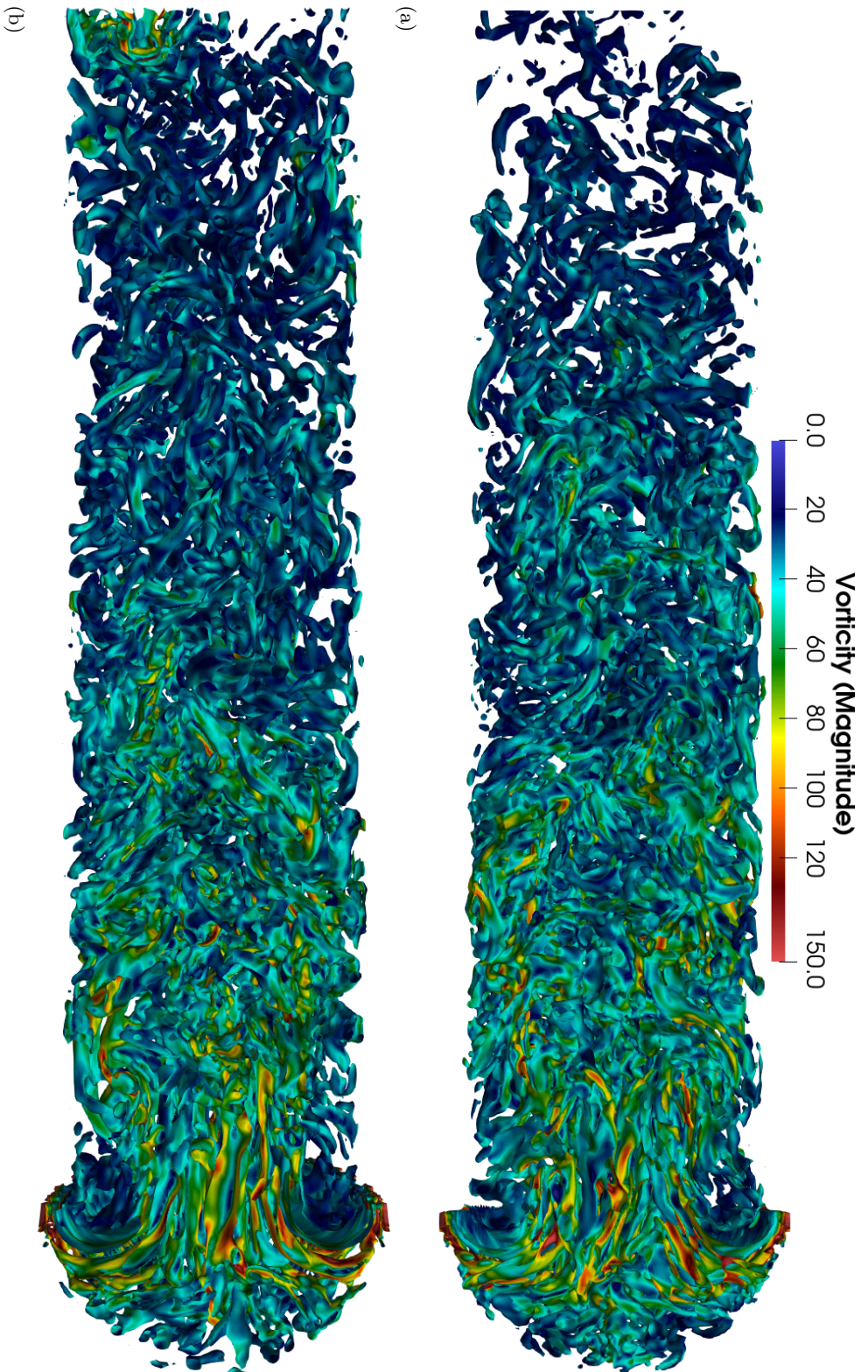


Figure 5.20: What is depicted in these two figures is a 3D contour of the  $Q$ -criterion with a value of 100. Then on the display, the isosurfaces are coloured with vorticity values in a range from 0.0 to 150.0. The figure 5.20a depicts the autoclave without hatches, while the figure 5.20b depicts the autoclave characterised by the presence of hatches.

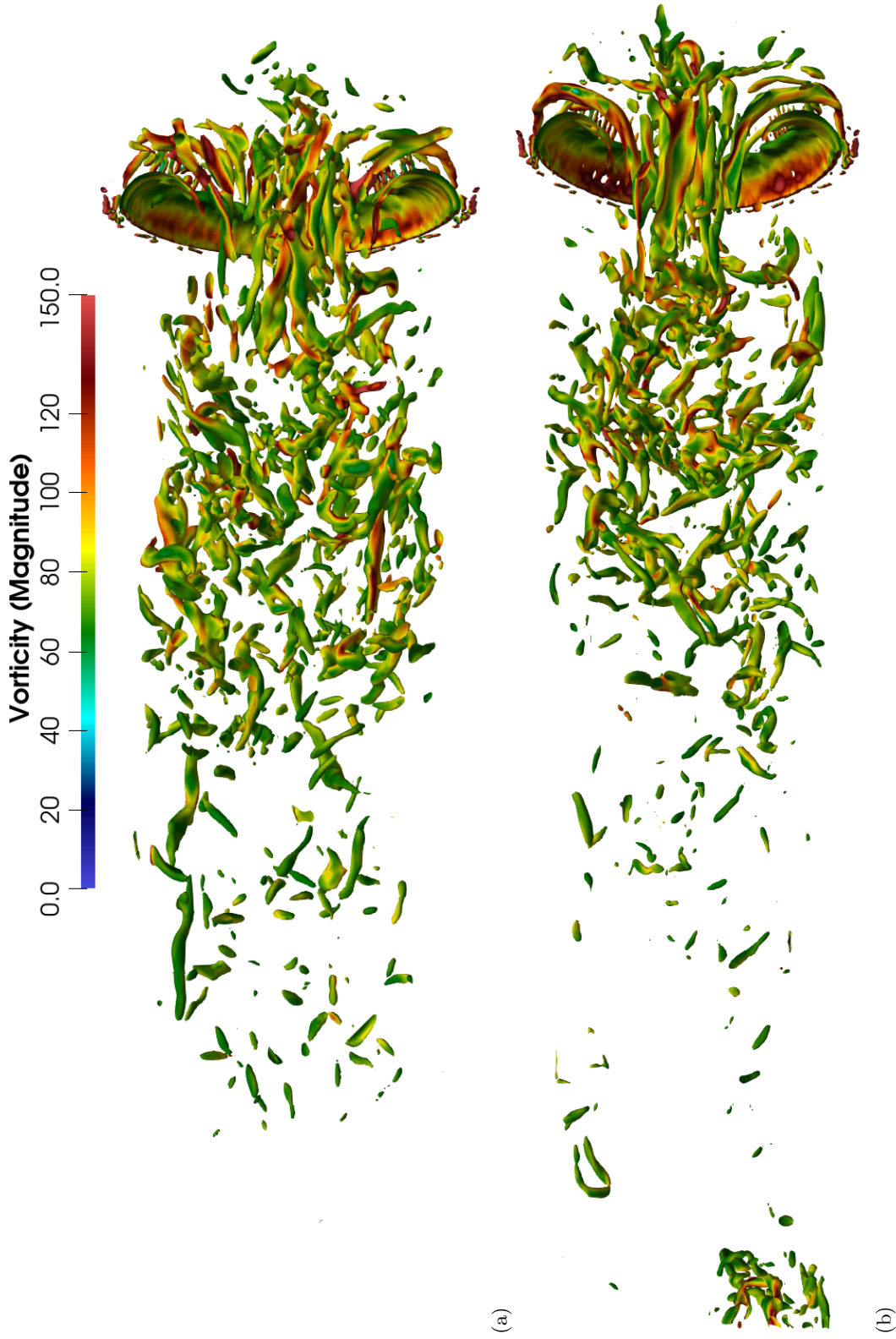


Figure 5.21: What is depicted in these two figures is a 3D contour of the Q-criterion with a value of 1000. Then on the display, the isosurfaces are coloured with vorticity values in a range from 0.0 to 150.0. The figure 5.21a depicts the autoclave without hatches, while the figure 5.21b depicts the autoclave characterised by the presence of hatches.



## Chapter 6

# Conclusions

This chapter, the concluding one, serves to draw a bit of a conclusion to all the work that has been done and presented within this thesis. Basically what has been done is nothing more than preliminary work on the study of turbulence inside the pressurized chamber of an industrial-type autoclave. The problem of homogeneity has enormous relevance in terms of achieving optimal results at the conclusion of the processing that such environments accommodate. Clearly, the results that have been presented are entirely preliminary results that will certainly need to be analyzed more carefully. Along with this, it must also be kept in mind that for reasons of time and available resources, compromises also had to be made, accepting the idea of making simplifications to the study. What emerges clearly at the end of it all, however, is how the proposal made to encourage the achievement of a degree of homogeneity of turbulence is proceeding in the right direction. In fact, while they may not have total validity, the results brought back show us that the use of what have been referred to as hatches certainly has a benign effect in this regard.

### 6.1 Future Scenarios

As is the case with all preliminary work of this kind, we are left with proposals and future steps that are intended to be pursued for the fully of all those developments that we have not been able to complete.

First of all, there was no opportunity to give much space to the output boundary condition discussion. In fact, in order to comply with the customs of an autoclave, in the simulations done the wall at the bottom of the domain was considered as an outflow wall from which the airflow can freely exit (in autoclaves in fact it is collected and then fed back into the chamber through the recirculation ducts). An interesting aspect would also be to evaluate a reflective condition that would result in a fully enclosed chamber with a flow that can flow back and up the chamber. Indeed, this condition would lead to different results from those obtained in terms of homogenization of turbulence.

Also, one can "play" differently with the number of hatches placed in the autoclave and especially on the duration of their opening between switches. Again in this sense

then one can reason about the insertion, additional or replacement of real mechanical appendages moved inside the chamber, always with the aim of homogenizing the turbulence in the autoclave.

As far as the simulative setup is concerned, one step forward is definitely to add functions for modeling near-wall flow, which at the moment has not been addressed in any way. Next then one could add bodies inside the autoclave to also put emphasis on the heat transfer and temperature gradient that is created and that is extremely related to the degree of homogeneity of the flow turbulence.

# Acknowledgements

Innanzitutto vorrei concentrarmi nel ringraziare coloro che hanno partecipato da vicino al progetto portato avanti durante questi 7 mesi. Quindi in primis la mia relatrice, la professoressa Daniela Tordella, che mi ha dato la possibilità di fare un'esperienza di questo tipo; questo lavoro mi ha infatti costretto a confrontarmi con tanti problemi diversi che mi hanno permesso di crescere sotto tanti aspetti. Mi ha lasciato libero di commettere errori e quindi imparare da essi e di portare avanti i vari sviluppi e le varie idee che hanno permesso poi il raggiungimento di ottimi risultati. Allo stesso tempo però è stata sempre molto disponibile e presente ogni qualvolta la contattassi. Per questo la ringrazio. Dopodiché un ringraziamento speciale va fatto anche a Luca Banetta. Durante questi mesi è stata una delle persone con le quali ho interagito di più. Mi ha dato un aiuto grandissimo e tante dritte che mi hanno permesso di migliorare e affrontare le varie sfide che mi si proponevano di fronte con un'ottica diversa e più matura rispetto a quanto facessi in passato. Lo ringrazio quindi per avermi supportato e sopportato sette giorni su sette per tutto questo lungo periodo.

Al termini di questo percorso, dopo 6 lunghi anni, il ringraziamento più grande va fatto sicuramente ai miei genitori. Grazie a loro e ai loro sforzi oggi mi sono laureato nel percorso magistrale di ingegneria al Politecnico di Torino, non una cosa che va data per scontata. Mi hanno sempre supportato, standomi vicino, senza essere invadenti e allo stesso tempo riponendo grandissima fiducia in tutto quello che facesti.

In generale grazie a tutti i miei amici, tutte le persone conosciute in questi anni tra Torino e altrove, ognuna delle quali mi ha lasciato qualcosa che porterò con me per sempre.

Per concludere vorrei ringraziare anche me stesso. Per non aver mai mollato, per aver lavorato sodo e averci sempre creduto. Oggi si è concluso un ciclo importante, da domani ne inizia un altro altrettanto importante, forse ancora di più. In bocca al lupo a me.



# Bibliography

- [1] Andrey Nikolaevich Kolmogorov. “The local structure of turbulence in incompressible viscous fluid for very large Reynolds numbers”. In: *Cr Acad. Sci. URSS* 30 (1941), pp. 301–305.
- [2] Jinhee Jeong and Fazle Hussain. “On the identification of a vortex”. In: *Journal of fluid mechanics* 285 (1995), pp. 69–94.
- [3] Andrew A Johnston. “An integrated model of the development of process-induced deformation in autoclave processing of composite structures”. PhD thesis. University of British Columbia, 1997.
- [4] Katepalli R Sreenivasan. “Fluid turbulence”. In: *Reviews of Modern Physics* 71.2 (1999), S383.
- [5] Robert Eymard, Thierry Gallouët, and Raphaële Herbin. “Finite volume methods”. In: *Handbook of numerical analysis* 7 (2000), pp. 713–1018.
- [6] S.B. Pope. *Turbulent Flows*. Cambridge University Press, 2000.
- [7] Roberto Verzicco. “Appunti di turbolenza”. In: *Dispense del corso di Fluidodinamica per Ingegneria Meccanica, Politecnico di Bari* (2001).
- [8] Timothy Barth and Mario Ohlberger. “Finite volume methods: foundation and analysis”. In: (2003).
- [9] Joaquim Peiró and Spencer Sherwin. “Finite difference, finite element and finite volume methods for partial differential equations”. In: *Handbook of materials modeling*. Springer, 2005, pp. 2415–2446.
- [10] A. Mignone et al. “PLUTO: A Numerical Code for Computational Astrophysics”. In: *The Astrophysical Journal Supplement Series* 170.1 (2007), pp. 228–242. DOI: 10.1086/513316. URL: <https://doi.org/10.1086/513316>.
- [11] Amy Henderson Squillacote et al. *The paraview guide*. Vol. 366. Kitware Clifton Park, NY, 2007.
- [12] Rafael Borges et al. “An improved weighted essentially non-oscillatory scheme for hyperbolic conservation laws”. In: *Journal of Computational Physics* 227.6 (2008), pp. 3191–3211.
- [13] Wolfgang Hillebrandt and Friedrich Kupka. *Interdisciplinary aspects of turbulence*. Vol. 756. Springer Science & Business Media, 2008.

- [14] N Slesinger et al. “Heat transfer coefficient distribution inside an autoclave”. In: *17th international conference on composite material ICCM*. 2009.
- [15] Yoshihide Tominaga and Ted Stathopoulos. “CFD modeling of pollution dispersion in a street canyon: Comparison between LES and RANS”. In: *Journal of Wind Engineering and Industrial Aerodynamics* 99.4 (2011), pp. 340–348.
- [16] David J Tritton. *Physical fluid dynamics*. Springer Science & Business Media, 2012.
- [17] François Dumont, Werner Fröhlingdorf, and Christian Weimer. “Virtual autoclave implementation for improved composite part quality and productivity”. In: *CEAS Aeronautical Journal* 4.3 (2013), pp. 277–289.
- [18] Alexander J Smits and Ivan Marusic. “Wall-bounded turbulence”. In: *Phys. Today* 66.9 (2013), pp. 25–30.
- [19] Christoph Brehm et al. “A comparison of higher-order finite-difference shock capturing schemes”. In: *Computers & Fluids* 122 (2015), pp. 184–208.
- [20] NEJ Kluge et al. “An experimental study of temperature distribution in an autoclave”. In: *Journal of Reinforced Plastics and Composites* 35.7 (2016), pp. 566–578.
- [21] Dongxi Liu et al. “Comparison of laminar model, RANS, LES and VLES for simulation of liquid sloshing”. In: *Applied Ocean Research* 59 (2016), pp. 638–649.
- [22] Fadl Moukalled, Luca Mangani, and Marwan Darwish. “The finite volume method”. In: *The finite volume method in computational fluid dynamics*. Springer, 2016, pp. 103–135.
- [23] Tobias A Weber et al. “A fast method for the generation of boundary conditions for thermal autoclave simulation”. In: *Composites Part A: Applied Science and Manufacturing* 88 (2016), pp. 216–225.
- [24] Y-T Zhang and C-W Shu. “ENO and WENO schemes”. In: *Handbook of Numerical Analysis*. Vol. 17. Elsevier, 2016, pp. 103–122.
- [25] Ismet Baran et al. “A review on the mechanical modeling of composite manufacturing processes”. In: *Archives of computational methods in engineering* 24.2 (2017), pp. 365–395.
- [26] M Dios et al. “A mathematical modeling approach to optimize composite parts placement in autoclave”. In: *International Transactions in Operational Research* 24.1-2 (2017), pp. 115–141.
- [27] Twan van Hooff, Bert Blocken, and Yoshihide Tominaga. “On the accuracy of CFD simulations of cross-ventilation flows for a generic isolated building: comparison of RANS, LES and experiments”. In: *Building and Environment* 114 (2017), pp. 148–165.
- [28] Tobias A Weber et al. “Thermal optimization of composite autoclave molds using the shift factor approach for boundary condition estimation”. In: *Journal of Composite Materials* 51.12 (2017), pp. 1753–1767.

- [29] S Anandan et al. “Curing of thick thermoset composite laminates: multiphysics modeling and experiments”. In: *Applied Composite Materials* 25.5 (2018), pp. 1155–1168.
- [30] Tobias Bohne et al. “Simulation and validation of air flow and heat transfer in an autoclave process for definition of thermal boundary conditions during curing of composite parts”. In: *Journal of Composite Materials* 52.12 (2018), pp. 1677–1687.
- [31] Juan A Garcí'a-Manrique et al. “Study of the degree of cure through thermal analysis and Raman spectroscopy in composite-forming processes”. In: *Materials* 12.23 (2019), p. 3991.
- [32] Ning Han et al. “Research on temperature field distribution in a frame mold during autoclave process”. In: *Materials* 13.18 (2020), p. 4020.
- [33] Mohammadreza Shirzadi, Parham A Mirzaei, and Yoshihide Tominaga. “CFD analysis of cross-ventilation flow in a group of generic buildings: Comparison between steady RANS, LES and wind tunnel experiments”. In: *Building Simulation*. Vol. 13. 6. Springer. 2020, pp. 1353–1372.
- [34] Mahendra K Verma. “Variable energy flux in turbulence”. In: *Journal of Physics A: Mathematical and Theoretical* (2021).
- [35] Junhong Zhu, Tim Frerich, and Axel S Herrmann. “CFD modeling and validation of heat transfer inside an autoclave based on a mesh independency study”. In: *Journal of Composite Materials* 55.18 (2021), pp. 2469–2487.
- [36] Wikipedia. *Autoclave* — *Wikipedia, L'enciclopedia libera*. [Online; in data 12-maggio-2022]. 2022. URL: <http://it.wikipedia.org/w/index.php?title=Autoclave&oldid=126888574>.
- [37] Wikipedia. *Materiale composito* — *Wikipedia, L'enciclopedia libera*. [Online; in data 6-giugno-2022]. 2022. URL: [http://it.wikipedia.org/w/index.php?title=Materiale\\_composito&oldid=125280466](http://it.wikipedia.org/w/index.php?title=Materiale_composito&oldid=125280466).
- [38] Wikipedia contributors. *MATLAB* — *Wikipedia, The Free Encyclopedia*. <https://en.wikipedia.org/w/index.php?title=MATLAB&oldid=1090198052>. [Online; accessed 4-July-2022]. 2022.
- [39] Enbio. *Autoclave: che cos'è e a che cosa serve? Tutto ciò che dovete sapere*. URL: <https://www.enbio.com/it/blog/post/autoclave-che-cose>.
- [40] Staff HPC@Polito. “*Computational resources provided by hpc@polito, which is a project of Academic Computing within the Department of Control and Computer Engineering at the Politecnico di Torino*”. URL: (<http://hpc.polito.it>).
- [41] Italmatic. *Autoclavi*. URL: <https://italmatic.net/settori/autoclavi/>.
- [42] Italmatic. *Progettazione e costruzione Autoclavi industriali certificate*. URL: <https://www.italmatic.eu/autoclavi-2/>.
- [43] HPC WIKI. *Scaling*. URL: <https://hpc-wiki.info/hpc/Scaling>.